A FLUID-STRUCTURE INTERACTION MODEL CAPTURING LONGITUDINAL DISPLACEMENT IN ARTERIES: MODELING, COMPUTATIONAL METHOD, AND COMPARISON WITH EXPERIMENTAL DATA

A Dissertation

Presented to

the Faculty of the Department of Mathematics

University of Houston

In Partial Fulfillment

of the Requirements for the Degree

Doctor of Philosophy

By

Martina Bukač

May 2012

A FLUID-STRUCTURE INTERACTION MODEL CAPTURING LONGITUDINAL DISPLACEMENT IN ARTERIES: MODELING, COMPUTATIONAL METHOD, AND COMPARISON WITH EXPERIMENTAL DATA

Martina Bukač

APPROVED:

Dr. Sunčica Čanić,
Chairman
Dept. of Mathematics, University of Houston

Dr. Roland Glowinski
Dept. of Mathematics, University of Houston

Dr. Annalisa Quaini
Dept. of Mathematics, University of Houston

Dr. Josip Tambača
Dept. of Mathematics, University of Zagreb

Dean, College of Natural Sciences and Mathematics

Acknowledgements

First and foremost, I acknowledge Dr. Sunčica Čanić, without whom I could not have completed this thesis. She is the best advisor and teacher I could have wished for, full of contagious enthusiasm and inspiration, which were always there when I needed it. I appreciate all her contributions of time, ideas, and funding to make my PhD experience productive and stimulating.

I feel privileged to have been able to work with Dr. Roland Glowinski, who gave me tools that were essential in my PhD research. His infinite wisdom and knowledge gave me the confidence to explore my research interests and the guidance to avoid getting lost in my exploration.

Many thanks to Dr. Josip Tambača, who has inspired me from early stages, and introduced me to applied mathematics. My initial interest in mathematics as well as my decision to pursue an academic career in mathematics and science can be attributed in large part to the undergraduate courses I took with him and to the experience I gained while he was advising my undergraduate thesis. I am also grateful for his valuable suggestions and tireless help during my time in graduate school.

I gratefully acknowledge Dr. Annalisa Quaini for discussing research and more, for the contribution of numerous ideas and suggestions. Most important, I acknowledge her for being an exceptional friend who always gave me a brighter look on things, and with whom I spent many unforgettable moments.

I thank Dr. Boris Muha, who first introduced me to Continuum Mechanics, for

suggestions and inspiration in the later stages of my thesis. I also acknowledge him for contributing to the work done in Chapter 5.3 of this thesis.

My time in Houston was made enjoyable in large part due to the many friends and groups that became a part of my life. I am grateful for time spent with them, for many international dinners and board game nights. Their company made my time at the Department filled with joy and laughter even at the most trying times of my tenure as a graduate student.

This thesis is dedicated to my parents, who have always offered unwavering support for my decisions and who have have consistently placed their faith in my ability to make these decisions myself. Without this balance of support and independence, I am certain that I could not have developed the determination nor the confidence in my abilities and in my decisions that have been necessary to complete my doctoral work.

A FLUID-STRUCTURE INTERACTION MODEL CAPTURING LONGITUDINAL DISPLACEMENT IN ARTERIES: MODELING, COMPUTATIONAL METHOD, AND COMPARISON WITH EXPERIMENTAL DATA

An Abstract of a Dissertation

Presented to

the Faculty of the Department of Mathematics

University of Houston

In Partial Fulfillment

of the Requirements for the Degree

Doctor of Philosophy

By

Martina Bukač

May 2012

Abstract

The focus of this thesis is on numerical modeling of fluid-structure interaction (FSI) problems with application to hemodynamics.

Recent *in vivo* studies, utilizing ultrasound contour and speckle tracking methods, have identified significant longitudinal wall displacements and viscoelastic arterial wall properties over a cardiac cycle. Existing computational models that use thin structure approximations of arterial walls have so far been limited to elastic models that capture only radial wall displacements. In this thesis, we present a new model and a novel loosely coupled partitioned numerical scheme modeling fluid-structure interaction (FSI) in blood flow allowing non-zero longitudinal displacement.

In this work arterial walls are modeled by a linearly viscoelastic, cylindrical Koiter shell model capturing both radial and longitudinal displacement. Fluid flow is modeled by the Navier-Stokes equations for an incompressible, viscous fluid. The two are fully coupled via kinematic and dynamic coupling conditions. The proposed numerical scheme is based on a new modified Lie operator splitting that decouples the fluid and structure sub-problems in a way that leads to a loosely coupled scheme that is *unconditionally* stable. This was achieved by a clever use of the kinematic coupling condition at the fluid and structure sub-problems, leading to an implicit coupling between the fluid and structure velocities. The proposed scheme is a modification of the recently introduced "kinematically coupled scheme" for which the newly proposed modified Lie splitting significantly increases the accuracy. In this work it is shown that the new scheme, called the kinematically coupled β-scheme, is unconditionally stable for all $\beta \in [0, 1]$. The performance and accuracy of the

scheme are studied on a series of instructive examples including a comparison with a monolithic scheme proposed by Quaini and Quarteroni in [77]. It is shown that the accuracy of our scheme is comparable to that of the monolithic scheme, while our scheme retains all the main advantages of partitioned schemes.

The results of the computational model are compared with *in vivo* measurements of the common carotid artery wall motion, and with data capturing stenosed coronary arteries, showing excellent agreement.

Keywords: Fluid-structure interaction, hemodynamics, loosely coupled scheme, longitudinal displacement, viscoelastic arteries.

Contents

List of Figures

List of Tables

Chapter 1

Introduction

Recent developments in ultrasound Contour and Speckle Tracking techniques make it now possible to measure *in vivo* radial and longitudinal arterial wall displacements [1, 25, 26, 28, 73, 84, 85, 89]. These measurements for the first time reveal that longitudinal displacement in healthy human arteries is comparable in magnitude to the radial displacement (see Figure 1.1). While healthy subjects exhibit significant longitudinal displacement, recent ultrasound *in vivo* measurements indicate that smaller longitudinal displacement is associated with atherosclerotic vessels [84], or with older, diabetic subjects [28] (see Figure 1.2). On the other hand, large longitudinal displacement is particularly pronounced under adrenaline conditions during which the longitudinal displacement of the intima-media complex increases by 200%, and becomes twice the magnitude of radial displacement [1]. Since the appropriate ultrasound techniques have only recently been developed, the relationship between longitudinal displacement and pathophysiology of the human cardiovascular system

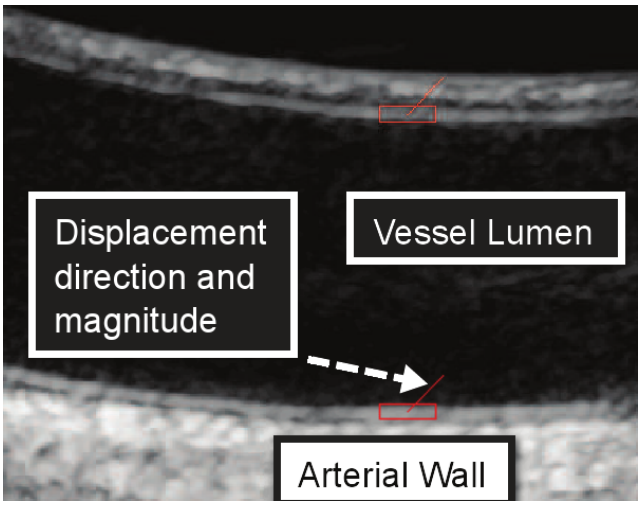

Figure 1.1: Longitudinal and radial displacement in a carotid artery measured using *in vivo* ultrasound speckle tracking method. The thin red line located at the intimal layer of the arterial wall shows the direction and magnitude of the displacement vector, showing equal magnitude in longitudinal and radial components of the displacement [28].

is under-explored, and the work in this thesis presents an important first step in this direction.

We study fluid-structure interaction (FSI) between an incompressible viscous, Newtonian fluid, and a thin viscoelastic structure modeled by the linearly viscoelastic cylindrical Koiter shell model. A cylindrical viscoelastic Koiter shell model is derived to describe the mechanical properties of arterial walls, while the Navier-Stokes equations for an incompressible, viscous, Newtonian fluid are employed to model the flow of blood in medium-to-large human arteries. The two are coupled via the kinematic (no-slip) and dynamic (balance of contact forces) coupling conditions.

In hemodynamics, the coupling between the fluid and structure is highly nonlinear due to the fact that the fluid and structure densities are roughly the same, making

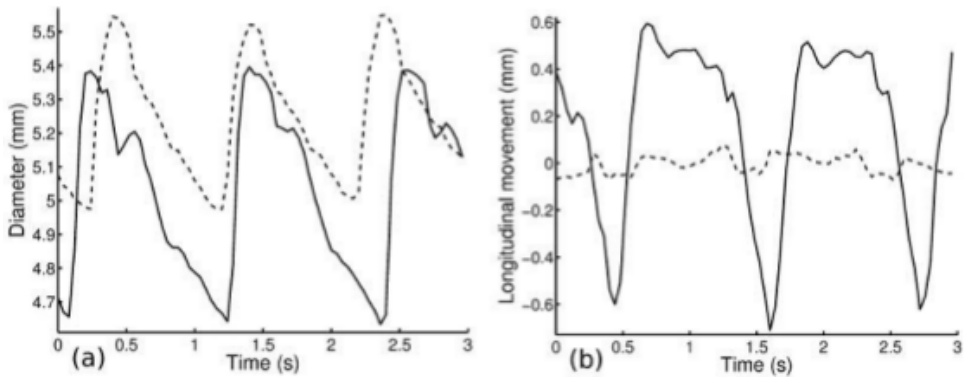

Figure 1.2: Comparison of carotid artery wall motion in a healthy and diabetic subject, measured *in vivo* using ultrasound speckle tracking methods [28].

the inertia of the fluid and structure roughly equal. In this regime, classical loosely coupled (or explicit) numerical schemes, which are based on the fluid and structure sub-solvers, have been shown to be intrinsically unstable [22] due to the miss-match between the discrete energy dictated by the numerical scheme, and the continuous energy of the coupled problem. This has been associated with the "added mass effect" [22]. To rectify this problem, the fluid and structure sub-solvers need to be sub-iterated until the energy balance at the discrete level approximates well the energy of the continuous coupled problem. The resulting strongly coupled scheme, however, gives rise to extremely high computational costs.

To get around these difficulties, several different loosely coupled algorithms have been proposed that modify the classical strategy in coupling the fluid and structure sub-solvers. The method proposed in [71] uses a simple membrane model for the structure that can be easily embedded into the fluid equations and appears as a generalized Robin boundary condition. In this way the original problem reduces to a sequence of fluid problems with a generalized Robin boundary condition that can

be solved using only the fluid solver. A similar approach was proposed in [8], where the fluid and structure are split in the classical way, but the fluid and structure sub-problems were linked via novel transmission (coupling) conditions that improve the convergence rate. Namely, a linear combination of the dynamic and kinematic interface conditions was used to artificially redistribute the fluid stress on the interface, thereby avoiding the difficulty associated with the added mass effect.

A different stabilization of the loosely coupled (explicit) schemes was proposed in [18] which is based on Nitsche's method [47] with a time penalty term giving L^2-control on the fluid force variations at the interface. We further mention the scheme proposed in [9], where Robin-Robin type preconditioner is combined with Krylov iterations for the solution of the interface system.

For completeness, we also mention several semi-implicit schemes. The schemes proposed in [4, 5, 37] separate the computation of fluid velocity from the coupled pressure-structure velocity system, thereby reducing the computational costs. Similar schemes, derived from algebraic splitting, were proposed in [10, 77]. We also mention [68] where an optimization problem is solved at each time-step to achieve continuity of stresses and continuity of velocity at the interface.

In this thesis we deal with the problems associated with the added mass effect by: (1) employing the kinematic coupling condition implicitly in all the sub-steps of the splitting, as in the kinematically coupled scheme first introduced in [46]; (2) treating the fluid sub-problem together with the viscous part of the structure equations so that the structure inertia appears in the fluid sub-problem (made possible by the kinematic coupling condition). In this step, a portion of the fluid stress, the fluid

inertia, and the viscous part of the structure equations are coupled weakly, and **implicitly**, thereby adding dissipative effects to the fluid solver and contributing to the overall stability of the scheme (although the scheme is stable even if viscoelasticity of the structure is neglected). The modification of the Lie splitting introduced in this manuscript uses the remaining portion of the normal fluid stress (the pressure) to explicitly load the structure in the elastodynamics equations, significantly increasing the accuracy of our scheme when compared with the classical kinematically coupled scheme [46], and making it comparable to that of the monolithic scheme presented in [10, 76]. Including the structure inertia implicitly in the fluid sub-problem is the main reason why our scheme is stable even when the density of the structure is equal to the density of fluid. We show, using ideas similar as in [22], that our scheme is unconditionally stable for all the ratios between the fluid and structure densities.

To deal with the motion of the fluid domain, we implemented an Arbitrary Lagrangian-Eulerian (ALE) approach. In addition to the ALE method [32, 48, 50, 59, 61, 77, 78], the Immersed Boundary Method [35, 40, 62, 65, 74, 75] has been very popular in problems with moving domains, especially when the structure is completely immersed in the fluid domain. We also mention the Fictitious Domain Method combined with the mortar element method or ALE method [7, 87], the Lattice Boltzmann method [34, 36, 53, 54], the Coupled Momentum Method [39], and the Level Set Method [27].

We used this computational model to study FSI in the common carotid artery and in a stenosed coronary artery under physiological conditions. Numerical results

were compared with measurement showing excellent agreement. New results related to the behavior of longitudinal displacement were obtained. More precisely, we showed that, unlike radial displacement, longitudinal displacement in stenotic lesions is highly dependent on the stenotic geometry. In particular, we showed that in type 3 stenotic geometry listed in Section 7.2, the magnitude of longitudinal displacement is largest, which may be associated with higher incidence of plaque rupture. We also showed that longitudinal displacement in atherosclerotic arteries is smaller than in healthy arteries, which is in line with the recent *in vivo* measurements that associate plaque burden with reduced total longitudinal wall displacement [85]. Details of the comparison between our numerical results and experimental measurements are presented in Chapter 7.

The research presented in this thesis provides a first step in our effort to capture multi-layered structure of arterial walls and their interaction with blood flow. In modeling the intima-media/adventitia complex, the coupling between a thin shell (intima) allowing radial and longitudinal displacement, and a thick structure (media/adventitia) is important. The development of the model presented in this thesis is crucial for this project. Our preliminary results show that the modified kinematically coupled scheme proposed in this manuscript is perfect for the numerical solution of such a FSI problem.

Chapter 2

The linearly viscoelastic Koiter models

2.1 Introduction

Arterial walls are complex structures composed of different layers, which makes their detailed elastic/viscoelastic behaviour difficult to model. There are three main layers that form arterial walls (see Figure 2.1):

- Tunica adventitia - The outermost layer of arterial wall; it is composed of connective tissue as well as collagen and elastic fibers.
- Tunica media - the middle layer of the arterial wall. It is composed of smooth muscle cells surrounded by a network of fibers primarily made of two proteins, collagen, and elastin. The elastin forms concentric rings within the vessel wall.
- Tunica intima - the innermost layer of arterial wall closest to the blood. It is composed of a single layer of specialized cells, called endothelial cells, which sit

atop the sub-endothelial space and a wall called the basement membrane.

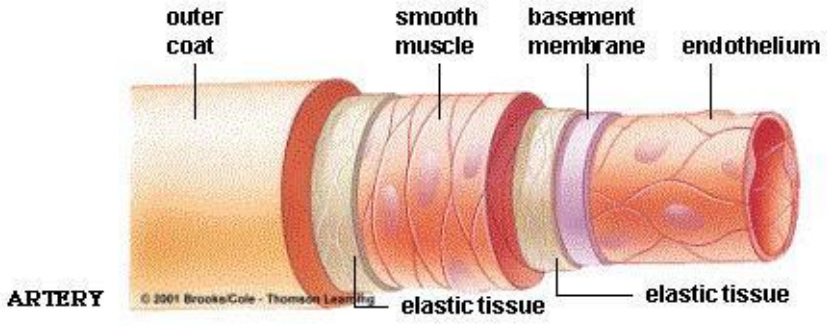

Figure 2.1: Layers forming arterial wall.

Since the full elastic response of arterial wall interacting with blood flow is difficult to model, the following set of simplifying assumptions is commonly introduced to capture only the most important physics in the description of the mechanical properties of arterial walls:

- homogeneity of the material with "small" displacements and "small" deformation gradients leading to the hypothesis of linear elasticity,
- "small" vessel wall thickness allowing a reduction from three-dimensional models to two-dimensional shell models,
- cylindrical geometry and axial symmetry leading to the further reduction to one-dimensional models capturing only radial displacement.

A classical model for arterial walls which includes those assumptions is the elastic membrane model. When external forces are applied, a membrane model captures deformation of the structure that only result from stretching. An extension of the

membrane model that captures deformation which result from both stretching and bending is a shell model.

In this chapter we derive the equations for the elastic membrane model for a tube with variable radius, and an elastic Koiter shell model for a straight tube; both are extended by the Kelvin-Voigt viscoelastic model. Kelvin-Voigt model has been shown in [2, 3, 11] to be a good approximation of the measured viscoelastic properties of the human carotid and femoral arteries, and the canine aorta.

2.2 Geometry of 2-surfaces and the shell problem

Let $\omega \subset \mathbb{R}^2$ be open, bounded and simply connected set with Lipschitz-continuous boundary ζ. Denote by $y = (y_\alpha)$ a generic point in $\overline{\omega}$, and let $\partial_\alpha := \partial/\partial_{y_\alpha}$ and $\partial_{\alpha\beta} := \partial^2/\partial y_\alpha \partial y_\beta$. Let $\boldsymbol{\varphi} \in C^3(\overline{\omega}; \mathbb{R}^3)$ be an injective mapping such that the two vectors

$$\boldsymbol{a}_\alpha(y) := \partial_\alpha \boldsymbol{\varphi}(y)$$

are linearly independent at all points $y \in \overline{\omega}$. Then they form the *covariant basis* of the tangent plane to the surface $S := \boldsymbol{\varphi}(\overline{\omega})$ at the point $\boldsymbol{\varphi}(y)$. The *contravariant basis* of the tangent plane is formed by the two vectors $\boldsymbol{a}^\alpha(y)$ defined by

$$\boldsymbol{a}^\alpha(y) \cdot \boldsymbol{a}_\beta(y) = \delta^\alpha_\beta.$$

To extend the basis to the whole space, we define the third vector (see Figure 2.2)

$$\boldsymbol{a}_3(y) = \boldsymbol{a}^3(y) = \frac{\boldsymbol{a}_1(y) \times \boldsymbol{a}_2(y)}{|\boldsymbol{a}_1(y) \times \boldsymbol{a}_2(y)|}.$$

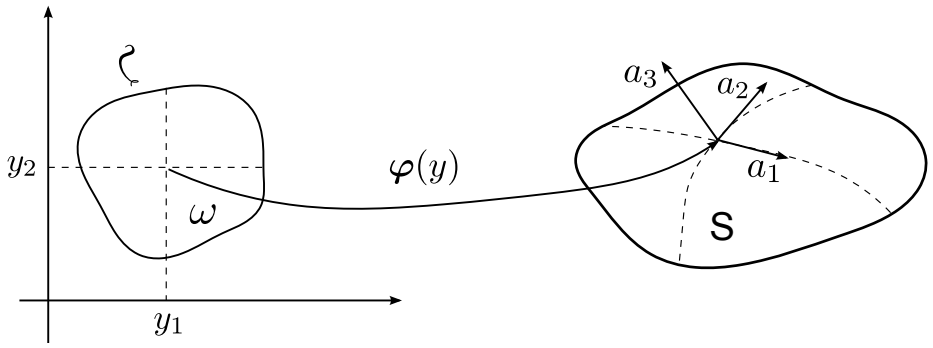

Figure 2.2: The mapping φ and the covariant basis at a point y

The *metric tensor* (*first fundamental form*) of the surface S in covariant $\mathbf{A}_c = (a_{\alpha\beta})$ or contravariant $\mathbf{A}^c = (a^{\alpha\beta})$ components is given, respectively, by

$$a_{\alpha\beta} = \boldsymbol{a}_\alpha \cdot \boldsymbol{a}_\beta, \quad a^{\alpha\beta} = \boldsymbol{a}^\alpha \cdot \boldsymbol{a}^\beta.$$

The area element along S is $\sqrt{a}dy$, where $a := det(\mathbf{A}_c) > 0$ in $\overline{\omega}$ since $\mathbf{A}_c$ is a positive definite matrix.

The *curvature tensor* (*second fundamental form*) of surface S in covariant $\mathbf{B}_c = (b_{\alpha\beta})$ or mixed $\mathbf{B} = (b^\beta_\alpha)$ components is given, respectively, by

$$b_{\alpha\beta} = \boldsymbol{a}_3 \cdot \partial_\alpha \boldsymbol{a}_\beta = -\partial_\alpha \boldsymbol{a}_3 \cdot \boldsymbol{a}_\beta, \quad b^\beta_\alpha = a^{\beta\sigma} b_{\sigma\alpha}.$$

The *Christoffel symbols* $\boldsymbol{\Gamma}^\sigma$ are given by

$$\Gamma^\sigma_{\alpha\beta} = \boldsymbol{a}^\sigma \cdot \partial_\beta \boldsymbol{a}_\alpha = -\partial_\beta \boldsymbol{a}^\sigma \cdot \boldsymbol{a}_\alpha.$$

In addition, we define covariant components $c_{\alpha\beta}$ of the third fundamental form of the surface S by

$$c_{\alpha\beta} = b^\sigma_\alpha b_{\sigma\beta},$$

and the first-order covariant derivatives $b^\sigma_\beta|_\alpha$ of the curvature tensor of S by

$$b^\sigma_\beta|_\alpha = \partial_\alpha b^\sigma_\beta + \Gamma^\sigma_{\alpha\tau} b^\tau_\beta - \Gamma^\tau_{\beta\alpha} b^\sigma_\tau.$$

For each $\epsilon > 0$, we define the set

$$\Omega^\epsilon = \omega \times (-\epsilon, \epsilon). \tag{2.1}$$

Let $x^\epsilon = (y, x^\epsilon_i)$ denote a generic point in $\overline{\Omega}^\epsilon$, and define a mapping $\boldsymbol{\Phi} : \overline{\Omega}^\epsilon \to \mathbb{R}^3$ by letting

$$\boldsymbol{\Phi}(x^\epsilon) := \boldsymbol{\varphi}(y) + x^\epsilon_3 \boldsymbol{a}^3(y), \quad \forall x^\epsilon = (y, x^\epsilon_3) \in \overline{\Omega}^\epsilon. \tag{2.2}$$

For each $0 < \epsilon \leq \epsilon_0$, the set $\boldsymbol{\Phi}(\overline{\Omega}^\epsilon)$ is the reference configuration of an elastic shell, with middle surface $S = \boldsymbol{\varphi}(\overline{\omega})$ and thickness 2ϵ. We will be assuming, see below, that the material constituting the shell is linearly elastic, isotropic and homogeneous, characterized by *Lamé constants* $\lambda > 0$ and $\mu > 0$.

2.3 Linearly viscoelastic Koiter shell model in curvilinear coordinates

Consider a linearly elastic shell of thickness 2ϵ, with middle surface $S = \boldsymbol{\varphi} \subset \mathbf{R}^3$, as defined in Section 2.2. Let ζ_0 be any portion of $\partial\omega$ with positive length. We assume the shell is clamped on a portion of their lateral face, whose middle line is $\boldsymbol{\varphi}(\zeta_0)$.

When external forces are applied, deformation of the shell will be a result of stretching and bending. Stretching of the surface is measured by the change of

metric tensor, and bending effects by the change of curvature tensor. Let $\boldsymbol{v} \in H^1(\omega) \times H^1(\omega) \times H^2(\omega)$. Then the *linearized change of metric tensor* $\boldsymbol{\gamma} = (\gamma_{\alpha\beta})$ and the *linearized change of curvature tensor* $\boldsymbol{\varrho} = (\varrho_{\alpha\beta})$ associated with $\boldsymbol{v}$, in covariant components, are given, respectively, by

$$\begin{aligned}
\gamma_{\alpha\beta}(\boldsymbol{v}) &= \frac{1}{2}(\partial_\alpha v_\beta + \partial_\beta v_\alpha) - \Gamma^\sigma_{\alpha\beta} v_\sigma - b_{\alpha\beta} v_3, \\
\varrho_{\alpha\beta}(\boldsymbol{v}) &= \partial_{\alpha\beta} v_3 - \Gamma^\sigma_{\alpha\beta}\partial_\sigma v_3 + b^\sigma_\beta(\partial_\alpha v_\sigma - \Gamma^\tau_{\alpha\sigma} v_\tau) + b^\sigma_\alpha(\partial_\beta v_\sigma - \Gamma^\tau_{\beta\sigma} v_\tau) + b^\sigma_\alpha|_\beta v_\sigma - c_{\alpha\beta} v_3,
\end{aligned}$$

where $\Gamma^\sigma_{\alpha\beta}$ are Christoffel symbols and $b_{\alpha\beta}$ are components of the second fundamental form defined in Section 2.2.

Introduce the elasticity tensor $\boldsymbol{\mathcal{A}}$ [24]

$$\boldsymbol{\mathcal{A}}\mathbf{E} = \frac{2E\sigma}{1-\sigma^2}(\mathbf{A}^c \cdot \mathbf{E})\mathbf{A}^c + \frac{2E}{1+\sigma}\mathbf{A}^c\mathbf{E}\mathbf{A}^c, \quad \mathbf{E} \in \mathrm{Sym}(\mathbb{R}^2), \tag{2.3}$$

where $\mathbf{A}_c$ and $\mathbf{A}^c$ are the first fundamental form in covariant and contravariant components, and $\cdot$ denotes the scalar product

$$A \cdot B := Tr(AB^\tau), \quad A, B \in M_2(\mathbb{R}).$$

Material properties are described through *Young's modulus* E and *Poisson's ration* σ. They are related to Lamé constants through the following identities

$$E = \frac{\mu(3\lambda + 2\mu)}{\lambda + \mu}, \qquad \sigma = \frac{\lambda}{2(\lambda + \mu)}.$$

Displacement of a shell corresponds to the displacement of shell's middle surface. Denote the displacement by $\boldsymbol{\eta}$ and assume that $\boldsymbol{\eta}$ is a function of space and time. We include viscoelastic behavior by assuming the Kelvin-Voigt model where the total stress is linearly proportional to strain and to the time-derivative of strain. Then, for

the linearly viscoelastic Koiter shell model we define the internal (stretching) force by

$$\frac{h}{2}\boldsymbol{\mathcal{A}}\boldsymbol{\gamma}(\boldsymbol{\eta}) + \frac{h}{2}\boldsymbol{\mathcal{B}}\boldsymbol{\gamma}(\dot{\boldsymbol{\eta}}), \tag{2.4}$$

and bending moment by

$$\frac{h^3}{24}\boldsymbol{\mathcal{A}}\boldsymbol{\varrho}(\boldsymbol{\eta}) + \frac{h^3}{24}\boldsymbol{\mathcal{B}}\boldsymbol{\varrho}(\dot{\boldsymbol{\eta}}). \tag{2.5}$$

Here $\dot{\boldsymbol{\eta}}$ denotes the time-derivative, h is thickness of the shell and $\boldsymbol{\mathcal{B}}$ is given by

$$\boldsymbol{\mathcal{B}}\mathbf{E} = \frac{2E_v\sigma_v}{1-\sigma_v^2}(\mathbf{A}^c \cdot \mathbf{E})\mathbf{A}^c + \frac{2E_v}{1+\sigma_v}\mathbf{A}^c\mathbf{E}\mathbf{A}^c, \quad \mathbf{E} \in \mathrm{Sym}(\mathbb{R}^2), \tag{2.6}$$

with E_v and σ_v corresponding to the viscous counterparts of the Young's modulus E and the Poisson's ratio σ.

To define the weak formulation, we introduce the following function space V by

$$V = \{\boldsymbol{v} \in H^1(\omega) \times H^1(\omega) \times H^2(\omega) : \boldsymbol{v}|_{\zeta_0} = 0,\ \partial_{\boldsymbol{\nu}} v_3|_{\zeta_0} = 0\}.$$

The total energy of the linearly viscoelastic Koiter shell is given by the sum of the contributions due to stretching and bending. The corresponding weak formulation will thus account for the internal (stretching) force and bending moment. Therefore, the weak formulation of the linearly viscoelastic Koiter shell is given by: for each $t > 0$ find $\boldsymbol{\eta}(t) \in V$ such that

$$\begin{aligned}\frac{h}{2}\int_\omega (\boldsymbol{\mathcal{A}}\boldsymbol{\gamma}(\boldsymbol{\eta}) + \boldsymbol{\mathcal{B}}\boldsymbol{\gamma}(\dot{\boldsymbol{\eta}})) \cdot \boldsymbol{\gamma}(\boldsymbol{\xi})\sqrt{a}dy + \frac{h^3}{24}\int_\omega (\boldsymbol{\mathcal{A}}\boldsymbol{\varrho}(\boldsymbol{\eta}) + \boldsymbol{\mathcal{B}}\boldsymbol{\varrho}(\dot{\boldsymbol{\eta}})) \cdot \boldsymbol{\varrho}(\boldsymbol{\xi})\sqrt{a}dy \\ +\rho_w h\int_\omega \frac{\partial^2\boldsymbol{\eta}}{\partial t^2} \cdot \boldsymbol{\xi}\sqrt{a}dy = \int_\omega \boldsymbol{f} \cdot \boldsymbol{\xi}\sqrt{a}dy, \quad \forall \boldsymbol{\xi} \in V,\end{aligned} \tag{2.7}$$

where ρ_w is shell's density and $\boldsymbol{f}$ is the vector of covariant components of the surface density of the force applied to the shell. The first term on the left-hand side of (2.7)

multiplying $h/2$ captures the membrane effects, while the second term on the left hand-side multiplying $h^3/24$ captures the flexural effects of the Koiter shell. In this model, components of the vector function $\boldsymbol{\eta}$ in the canonical basis are components of the displacement vector in contravariant basis.

2.4 The linearly viscoelastic membrane model for a tube with variable radius

To derive the linearly viscoleastic Koiter membrane model we note that the only difference between the membrane and shell models is that the shell model accounts for bending rigidity, while in the membrane this is negligible. Thus, the weak formulation of the linearly viscoelastic membrane model is: for each $t > 0$ find $\boldsymbol{\eta}(t) \in V$ such that $\forall \boldsymbol{\xi} \in V$

$$\frac{h}{2}\int_\omega (\boldsymbol{\mathcal{A}}\boldsymbol{\gamma}(\boldsymbol{\eta}) + \boldsymbol{\mathcal{B}}\boldsymbol{\gamma}(\dot{\boldsymbol{\eta}})) \cdot \boldsymbol{\gamma}(\boldsymbol{\xi})\sqrt{a}dy + \rho_w h \int_\omega \frac{\partial^2 \boldsymbol{\eta}}{\partial t^2} \cdot \boldsymbol{\xi}\sqrt{a}dy = \int_\omega \boldsymbol{f} \cdot \boldsymbol{\xi}\sqrt{a}dy. \quad (2.8)$$

Consider a clamped cylinder of length L, with variable radius $R(z)$, where $R : [0, L] \to \mathbb{R}$ is a smooth function. The reference surface is now defined by (see Figure 2.3)

$$\boldsymbol{\Phi} = \{x = (R(z)\cos\theta, R(z)\sin\theta, z) \in \mathbb{R}^3 : \theta \in (0, 2\pi), z \in (0, L)\},$$

and the reference position of the membrane is obtained through a smooth mapping

$$\boldsymbol{\varphi}(z, \theta) = (R(z)\cos\theta, R(z)\sin\theta, z) \in \mathbb{R}^3, \quad \text{for } z \in (0, L), \theta \in (0, 2\pi). \quad (2.9)$$

The mapping $\boldsymbol{\varphi}$ introduces a local system of curvilinear coordinates, whose covariant basis is given by

$$\begin{aligned}
\mathbf{a}_1 &= \frac{\partial \boldsymbol{\varphi}}{\partial z} = (R'(z)\cos\theta, R'(z)\sin\theta, 1), \\
\mathbf{a}_2 &= \frac{\partial \boldsymbol{\varphi}}{\partial \theta} = (-R(z)\sin\theta, R(z)\cos\theta, 0), \\
\mathbf{a}_3 &= \frac{a_1 \times a_2}{|a_1 \times a_2|} = (-\frac{\cos\theta}{\sqrt{1+(R')^2}}, -\frac{\sin\theta}{\sqrt{1+(R')^2}}, \frac{R'}{\sqrt{1+(R')^2}}).
\end{aligned}$$

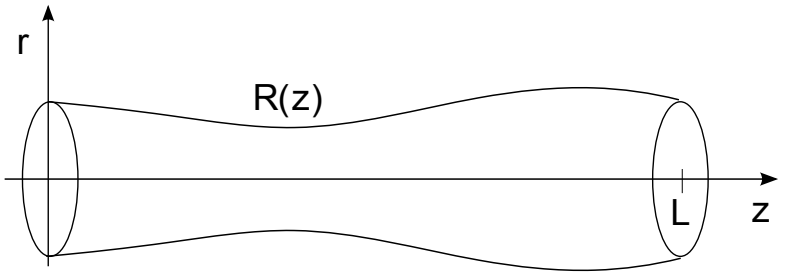

Figure 2.3: The reference domain

The contravariant basis is given by

$$\begin{aligned}
\mathbf{a}^1 &= \frac{1}{1+(R'(z))^2}(R'(z)\cos\theta, R'(z)\sin\theta, 1), \\
\mathbf{a}^2 &= \frac{1}{R}(-\sin\theta, \cos\theta, 0), \\
\mathbf{a}^3 &= \mathbf{a}_3 = (-\frac{\cos\theta}{\sqrt{1+(R')^2}}, -\frac{\sin\theta}{\sqrt{1+(R')^2}}, \frac{R'}{\sqrt{1+(R')^2}}).
\end{aligned}$$

The first fundamental form of the surface $\boldsymbol{\Phi}$ in covariant $\mathbf{A}_c = (a_{\alpha\beta})$ and contravariant $\mathbf{A}^c = (a^{\alpha\beta})$ components is, respectively,

$$\mathbf{A}_c = \begin{bmatrix} (R'(z))^2+1 & 0 \\ 0 & R(z)^2 \end{bmatrix}, \qquad \mathbf{A}^c = \begin{bmatrix} \frac{1}{(R'(z))^2+1} & 0 \\ 0 & \frac{1}{R(z)^2} \end{bmatrix}.$$

The second fundamental form of the surface $\mathbf{\Phi}$ in covariant $\mathbf{B}_c = (b_{\alpha\beta})$ and mixed components $\mathbf{B} = (b_\alpha^\beta)$ is, respectively,

$$\mathbf{B}_c = \begin{bmatrix} -\frac{R''(z)}{\sqrt{(R'(z))^2+1}} & 0 \\ 0 & \frac{R(z)}{\sqrt{(R'(z))^2+1}} \end{bmatrix}, \quad \mathbf{B} = \begin{bmatrix} -\frac{R''(z)}{((R'(z))^2+1)^{3/2}} & 0 \\ 0 & \frac{1}{R(z)\sqrt{(R'(z))^2+1}} \end{bmatrix}.$$

Now, the Christoffel symbols $\Gamma^\sigma_{\alpha\beta}$ for surface Σ read as follows

$$\begin{aligned} \Gamma^1_{11} &= \frac{R'(z)R''(z)}{1+R'(z)^2}, & \Gamma^2_{11} &= 0, \\ \Gamma^1_{12} &= \Gamma^1_{21} = 0, & \Gamma^2_{12} &= \Gamma^2_{21} = \frac{R'(z)}{R(z)}, \\ \Gamma^1_{22} &= -\frac{R(z)R'(z)}{1+R'(z)^2}, & \Gamma^2_{22} &= 0. \end{aligned}$$

Remark 2.4.1. Blouza and Le Dret showed in [14] that a linearized change of metric can be written in the following way

$$\gamma_{\alpha\beta}(\boldsymbol{v}) \;=\; \frac{1}{2}(\partial_\beta \tilde{\boldsymbol{v}} \cdot \boldsymbol{a}_\beta + \partial_\beta \tilde{\boldsymbol{v}} \cdot \boldsymbol{a}_\alpha), \tag{2.10}$$

for all $\boldsymbol{v} \in H^1(\omega) \times H^1(\omega) \times H^2(\omega)$, where $\tilde{\boldsymbol{v}} = [\boldsymbol{a}^1\ \boldsymbol{a}^2\ \boldsymbol{a}^3]\,\boldsymbol{v}$.

Using equation (2.10) the corresponding linearized change of metric reads as follows

$$\begin{aligned} \gamma_{11}(\boldsymbol{v}) &= \partial_1 v_1 - \frac{R''(z)R'(z)}{(R'(z))^2+1} v_1 + \frac{R''(z)}{\sqrt{1+(R'(z))^2}} v_3, \\ \gamma_{12}(\boldsymbol{v}) &= \frac{1}{2}(\partial_1 v_2 + \partial_2 v_1) - \frac{R'(z)}{R(z)} v_2, \\ \gamma_{21}(\boldsymbol{v}) &= \frac{1}{2}(\partial_2 v_1 + \partial_1 v_2) - \frac{R'(z)}{R(z)} v_2, \\ \gamma_{22}(\boldsymbol{v}) &= \partial_2 v_2 + \frac{R(z)R'(z)}{R'(z)^2+1} v_1 - \frac{R(z)}{\sqrt{1+(R'(z))^2}} v_3. \end{aligned}$$

Components of a vector function $\boldsymbol{v} = (v_1, v_2, v_3)$ are its components in contravariant basis $\{\boldsymbol{a}^1, \boldsymbol{a}^2, \boldsymbol{a}^3\}$. Note that the standard basis $\{\boldsymbol{e}_1, \boldsymbol{e}_2, \boldsymbol{e}_3\}$ can be written as a linear combination of vectors forming the contravariant basis in the following way

$$\begin{aligned}
\boldsymbol{e}_1 &= R'(z)\cos\theta\ \boldsymbol{a}^1 - R(z)\sin\theta\ \boldsymbol{a}^2 - \frac{\cos\theta}{\sqrt{1+R'(z)^2}}\ \boldsymbol{a}^3,\\
\boldsymbol{e}_2 &= R'(z)\sin\theta\ \boldsymbol{a}^1 + R(z)\cos\theta\ \boldsymbol{a}^2 - \frac{\sin\theta}{\sqrt{1+R'(z)^2}}\ \boldsymbol{a}^3,\\
\boldsymbol{e}_3 &= \boldsymbol{a}^1 + \frac{R'(z)}{\sqrt{1+R'(z)^2}}\ \boldsymbol{a}^3.
\end{aligned}$$

From this relation we can form the change of basis matrix $\boldsymbol{W}$ from the standard to contravariant basis:

$$\boldsymbol{W} = \begin{bmatrix} \boldsymbol{a}_1^\tau \\ \boldsymbol{a}_2^\tau \\ \boldsymbol{a}_3^\tau \end{bmatrix} = \begin{bmatrix} R'(z)\cos\theta & R'(z)\sin\theta & 1 \\ -R(z)\sin\theta & R(z)\cos\theta & 0 \\ -\frac{\cos\theta}{\sqrt{1+R'(z)^2}} & -\frac{\sin\theta}{\sqrt{1+R'(z)^2}} & \frac{R'(z)}{\sqrt{1+R'(z)^2}} \end{bmatrix}.$$

Given matrix $\boldsymbol{W}$, for every vector $\boldsymbol{v}$ we can relate its components in contravariant and standard basis as

$$[\boldsymbol{v}]_{\{\boldsymbol{a}^1,\boldsymbol{a}^2,\boldsymbol{a}^3\}} = \boldsymbol{W}[\boldsymbol{v}]_{\{\boldsymbol{e}_1,\boldsymbol{e}_2,\boldsymbol{e}_3\}}.$$

From here we can easily make a connection between the vector coordinates in contravariant and cylindrical coordinate system as

$$\begin{bmatrix} v_1 \\ v_2 \\ v_3 \end{bmatrix} = \begin{bmatrix} R'(z)\cos\theta & R'(z)\sin\theta & 1 \\ -R(z)\sin\theta & R(z)\cos\theta & 0 \\ -\frac{\cos\theta}{\sqrt{1+R'(z)^2}} & -\frac{\sin\theta}{\sqrt{1+R'(z)^2}} & \frac{R'(z)}{\sqrt{1+R'(z)^2}} \end{bmatrix} \begin{bmatrix} v_r\cos\theta \\ v_r\sin\theta \\ v_z \end{bmatrix}.$$

The latter equations simplify to

$$\begin{aligned} v_1 &= R'(z)v_r + v_z, \\ v_2 &= 0, \\ v_3 &= -\frac{1}{\sqrt{1+R'(z)^2}}v_r + \frac{R'(z)}{\sqrt{1+R'(z)^2}}v_z. \end{aligned}$$

Taking this into account, the change of metric tensor reads as follows

$$\boldsymbol{\gamma}(\boldsymbol{v}) = \begin{bmatrix} R'(z)v_r' + v_z' & 0 \\ 0 & R(z)v_r \end{bmatrix}, \qquad \forall (v_z, v_r) \in H_0^1(0,L) \times H_0^1(0,L). \tag{2.11}$$

With these constitutive relations and equation (2.8) we now define the weak formulation of the linearly viscoelastic membrane model by the following: for each $t > 0$ find $\boldsymbol{\eta}(t) = (\eta_z(t), \eta_r(t)) \in H_0^1(0,L) \times H_0^1(0,L)$ such that

$$\begin{aligned} &\frac{h}{2}\int_0^L (\boldsymbol{\mathcal{A}}\boldsymbol{\gamma}(\boldsymbol{\eta}) + \boldsymbol{\mathcal{B}}\boldsymbol{\gamma}(\dot{\boldsymbol{\eta}})) \cdot \boldsymbol{\gamma}(\boldsymbol{\xi}) R(z)\sqrt{1+R'(z)^2}dz + \rho_w h \int_0^L \frac{\partial^2 \boldsymbol{\eta}}{\partial t^2} \cdot \boldsymbol{\xi} R(z)\sqrt{1+R'(z)^2}dz \\ &\qquad = \int_0^L \boldsymbol{f} \cdot \boldsymbol{\xi} R(z)\sqrt{1+R'(z)^2}dz, \qquad \forall \boldsymbol{\xi} = (\xi_z, \xi_r) \in H_0^1 \times H_0^1. \end{aligned} \tag{2.12}$$

Written in terms of the **displacement**, employing the notation

$$C_v := \frac{E_v}{1-\sigma_v^2}, \quad D_v := \frac{E_v \sigma_v}{1-\sigma_v^2},$$

and after integration by parts, the weak formulation of the linearly viscoelastic Koiter

membrane model is given by

$$
\begin{aligned}
&-\int_0^L \frac{\partial}{\partial z}\Big(\frac{EhR(z)R'(z)^2}{(1-\sigma^2)(1+R'(z)^2)^{3/2}}\frac{\partial \eta_r}{\partial z}\Big)\xi_r dz - \int_0^L \frac{\partial}{\partial z}\Big(\frac{EhR(z)R'(z)}{(1-\sigma^2)(1+R'(z)^2)^{3/2}}\frac{\partial \eta_z}{\partial z}\Big)\xi_r dz\\
&-\int_0^L \frac{\partial}{\partial z}\Big(\frac{EhR(z)R'(z)}{(1-\sigma^2)(1+R'(z)^2)^{3/2}}\frac{\partial \eta_r}{\partial z}\Big)\xi_z dz + \int_0^L \frac{Eh\sigma R'(z)}{(1-\sigma^2)\sqrt{1+R'(z)^2}}\frac{\partial \eta_r}{\partial z}\xi_r dz\\
&-\int_0^L \frac{\partial}{\partial z}\Big(\frac{Eh\sigma}{(1-\sigma^2)\sqrt{1+R'(z)^2}}\eta_r\Big)\xi_z dz - \int_0^L \frac{\partial}{\partial z}\Big(\frac{EhR(z)}{(1-\sigma^2)(1+R'(z)^2)^{3/2}}\frac{\partial \eta_z}{\partial z}\Big)\xi_z dz\\
&+\int_0^L \frac{Eh}{1-\sigma^2}\frac{\sqrt{1+R'(z)^2}}{R(z)}\eta_r\xi_r dz + \int_0^L \frac{Eh\sigma}{1-\sigma^2}\frac{1}{\sqrt{1+R'(z)^2}}\frac{\partial \eta_z}{\partial z}\xi_r dz\\
&-\int_0^L \frac{\partial}{\partial z}\Big(\frac{Eh\sigma}{1-\sigma^2}\frac{R'(z)}{\sqrt{1+R'(z)^2}}\eta_r\Big)\xi_r dz - \int_0^L \frac{\partial}{\partial z}\Big(\frac{C_v hR(z)R'(z)^2}{(1+R'(z)^2)^{3/2}}\frac{\partial^2 \eta_r}{\partial z\partial t}\Big)\xi_r dz\\
&-\int_0^L \frac{\partial}{\partial z}\Big(\frac{C_v hR(z)R'(z)}{(1+R'(z)^2)^{3/2}}\frac{\partial^2 \eta_z}{\partial z\partial t}\Big)\xi_r dz - \int_0^L \frac{\partial}{\partial z}\Big(\frac{C_v hR(z)R'(z)}{(1+R'(z)^2)^{3/2}}\frac{\partial^2 \eta_r}{\partial z\partial t}\Big)\xi_z dz\\
&-\int_0^L \frac{\partial}{\partial z}\Big(\frac{C_v hR(z)}{\sqrt{1+R'(z)^2}^2}\frac{\partial^2 \eta_z}{\partial z\partial t}\Big)\xi_z dz - \int_0^L \frac{\partial}{\partial z}\Big(\frac{D_v hR'(z)}{\sqrt{1+R'(z)^2}}\frac{\partial \eta_r}{\partial t}\Big)\xi_r dz\\
&-\int_0^L \frac{\partial}{\partial z}\Big(\frac{D_v h}{\sqrt{1+R'(z)^2}}\frac{\partial \eta_r}{\partial t}\Big)\xi_z dz + \int_0^L \frac{C_v h\sqrt{1+R'(z)^2}}{R(z)}\frac{\partial \eta_r}{\partial t}\xi_r dz\\
&+\int_0^L \frac{D_v hR'(z)}{\sqrt{1+R'(z)^2}}\frac{\partial^2 \eta_r}{\partial z\partial t}\xi_r dz + \int_0^L \frac{D_v h}{\sqrt{1+R(z)'^2}}\frac{\partial^2 \eta_z}{\partial z\partial t}\xi_r dz\\
&+\rho_w h\int_0^L (\frac{\partial^2 \eta_z}{\partial t^2}\xi_z + \frac{\partial^2 \eta_r}{\partial t^2}\xi_r)R(z)\sqrt{1+R(z)'^2}dz\\
&=\int_0^L (f_z\xi_z + f_r\xi_r)R(z)\sqrt{1+R(z)'^2}dz, \quad \text{for all } \boldsymbol{\xi}=(\xi_z,\xi_r)\in H_0^1\times H_0^1.
\end{aligned}
$$

From here the equilibrium equations read as follows

$$
\begin{aligned}
f_z \;=\;& \rho_w h\frac{\partial^2 \eta_z}{\partial t^2} - \frac{\partial}{\partial z}\Big(C_0\eta_r\Big)\frac{1}{R\sqrt{1+R'^2}} - \frac{\partial}{\partial z}\Big(C_1\frac{\partial \eta_z}{\partial z}\Big)\frac{1}{R\sqrt{1+R'^2}}\\
&-\frac{\partial}{\partial z}\Big(C_2\frac{\partial \eta_r}{\partial z}\Big)\frac{1}{R\sqrt{1+R'^2}} - \frac{\partial}{\partial z}\Big(D_0\frac{\partial \eta_r}{\partial t}\Big)\frac{1}{R\sqrt{1+R'^2}}\\
&-\frac{\partial}{\partial z}\Big(D_1\frac{\partial^2 \eta_z}{\partial t\partial z}\Big)\frac{1}{R\sqrt{1+R'^2}} - \frac{\partial}{\partial z}\Big(D_2\frac{\partial^2 \eta_r}{\partial t\partial z}\Big)\frac{1}{R\sqrt{1+R'^2}},
\end{aligned}
$$

$$
\begin{aligned}
f_r &= \rho_w h\frac{\partial^2\eta_r}{\partial t^2} + C_3\eta_r - \frac{\partial}{\partial z}\left(C_4\eta_r\right)\frac{1}{R\sqrt{1+R'^2}} + C_5\frac{\partial\eta_r}{\partial z} + C_6\frac{\partial\eta_z}{\partial z} \\
&\quad -\frac{\partial}{\partial z}\left(C_7\frac{\partial\eta_r}{\partial z}\right)\frac{1}{R\sqrt{1+R'^2}} - \frac{\partial}{\partial z}\left(C_2\frac{\partial\eta_z}{\partial z}\right)\frac{1}{R\sqrt{1+R'^2}} + D_3\frac{\partial\eta_r}{\partial t} + D_4\frac{\partial^2\eta_r}{\partial t\partial z} \\
&\quad +D_5\frac{\partial^2\eta_z}{\partial t\partial z} - \frac{\partial}{\partial z}\left(D_6\frac{\partial\eta_r}{\partial t}\right)\frac{1}{R\sqrt{1+R'^2}} - \frac{\partial}{\partial z}\left(D_7\frac{\partial^2\eta_r}{\partial t\partial z}\right)\frac{1}{R\sqrt{1+R'^2}} \\
&\quad -\frac{\partial}{\partial z}\left(D_2\frac{\partial^2\eta_z}{\partial t\partial z}\right)\frac{1}{R\sqrt{1+R'^2}},
\end{aligned}
$$

where

$$
\begin{aligned}
&C_0 = \tfrac{hE\sigma}{1-\sigma^2}\tfrac{1}{\sqrt{1+R'^2}}, \quad C_1 = \tfrac{hE}{1-\sigma^2}\tfrac{R}{(1+R'^2)^{3/2}}, \quad C_2 = \tfrac{hE}{1-\sigma^2}\tfrac{R'R}{(1+R'^2)^{3/2}}, \quad C_3 = \tfrac{hE}{1-\sigma^2}\tfrac{1}{R^2}, \\
&C_4 = \tfrac{hE\sigma}{1-\sigma^2}\tfrac{R'}{\sqrt{1+R'^2}}, \quad C_5 = \tfrac{hE\sigma}{1-\sigma^2}\tfrac{R'}{R(1+R'^2)}, \quad C_6 = \tfrac{hE\sigma}{1-\sigma^2}\tfrac{1}{R(1+R'^2)}, \quad C_7 = \tfrac{hE}{1-\sigma^2}\tfrac{RR'^2}{(1+R'^2)^{3/2}}, \\
&D_0 = hD_v\tfrac{1}{\sqrt{1+R'^2}}, \quad D_1 = hC_v\tfrac{R}{(1+R'^2)^{3/2}}, \quad D_2 = hC_v\tfrac{RR'}{(1+R'^2)^{3/2}}, \quad D_3 = hC_v\tfrac{1}{R^2}, \\
&D_4 = hD_v\tfrac{R'}{R(1+R'^2)}, \quad D_5 = hD_v\tfrac{1}{R(1+R'^2)}, \quad D_6 = hD_v\tfrac{R'}{\sqrt{1+R'^2}}, \quad D_7 = hC_v\tfrac{RR'^2}{(1+R'^2)^{3/2}}.
\end{aligned}
$$

At this step it is easy to include the space-dependence of Young's modulus, structure thickness or viscoelastic parameters. Let us assume that the stiffness changes along the cylinder, i.e. $E = E(z)$, and let $h = const, C_v = const$, and $D_v = const$. After taking all the derivatives, the viscoelastic Koiter membrane model is given by

$$
\begin{aligned}
f_z &= \rho_w h\frac{\partial^2\eta_z}{\partial t^2} - a_0\eta_r - a_1\frac{\partial\eta_r}{\partial z} - a_2\frac{\partial\eta_z}{\partial z} - a_3\frac{\partial^2\eta_r}{\partial z^2} - a_4\frac{\partial^2\eta_z}{\partial z^2} - b_0\frac{\partial\eta_r}{\partial t} - b_1\frac{\partial^2\eta_r}{\partial t\partial z} \\
&\quad -b_2\frac{\partial^2\eta_z}{\partial t\partial z} - b_3\frac{\partial^3\eta_r}{\partial t\partial z^2} - b_4\frac{\partial^3\eta_z}{\partial t\partial z^2}, \qquad (2.13) \\
f_r &= \rho_w h\frac{\partial^2\eta_r}{\partial t^2} + a_5\eta_r - a_6\frac{\partial\eta_r}{\partial z} + a_7\frac{\partial\eta_z}{\partial z} - a_8\frac{\partial^2\eta_r}{\partial z^2} - a_3\frac{\partial^2\eta_z}{\partial z^2} + b_5\frac{\partial\eta_r}{\partial t} - b_6\frac{\partial^2\eta_r}{\partial t\partial z} \\
&\quad +b_7\frac{\partial^2\eta_z}{\partial t\partial z} - b_8\frac{\partial^3\eta_r}{\partial t\partial z^2} - b_3\frac{\partial^3\eta_z}{\partial t\partial z^2}, \qquad (2.14)
\end{aligned}
$$

where

$$
\begin{aligned}
a_0 &= \frac{h\sigma}{1-\sigma^2}\frac{1}{R(1+R'^2)}\left(E' - \frac{ER'R''}{1+R'^2}\right),\\
a_1 &= \frac{h}{1-\sigma^2}\frac{1}{1+R'^2}\left(\frac{R'}{1+R'^2}E' + \frac{E}{R}(\sigma + \frac{R'^2(R'^2-2R''R+1)+R''R}{(1+R'^2)^2})\right),\\
a_2 &= \frac{h}{1-\sigma^2}\frac{1}{(1+R'^2)^2}\left(E' + \frac{ER'(1+R'^2-3RR'')}{R(1+R'^2)}\right),\\
a_3 &= \frac{hE}{1-\sigma^2}\frac{R'}{(1+R^2)^2},\\
a_4 &= \frac{hE}{1-\sigma^2}\frac{1}{(1+R'^2)^2},\\
a_5 &= \frac{h}{R(1-\sigma^2)}\left(\frac{E}{R} - \frac{\sigma R'}{1+R'^2}E' - \frac{E\sigma R''}{(1+R'^2)^2}\right),\\
a_6 &= \frac{h}{1-\sigma^2}\frac{R'}{(1+R'^2)^2}\left(E'R' + \frac{E}{R}\frac{RR''(2-R'^2)+R'^2(1+R'^2)}{1+R'^2}\right),\\
a_7 &= \frac{h}{1-\sigma^2}\frac{1}{1+R'^2}\left(-\frac{R'}{1+R'^2}E' + \frac{E}{R}(\sigma - \frac{R'^2(R'^2-2R''R+1)+R''R}{(1+R'^2)^2})\right),\\
a_8 &= \frac{hE}{1-\sigma^2}\left(\frac{R'}{1+R'^2}\right)^2\\
b_0 &= -\frac{hD_vR'R''}{R(1+R'^2)^2},\\
b_1 &= \frac{h}{1+R'^2}\left(\frac{D_v}{R} + \frac{C_v}{R}\frac{R'^2(R'^2-2R''R+1)+R''R}{(1+R'^2)^2}\right),\\
b_2 &= \frac{hC_vR'(1+R'^2-3RR'')}{R(1+R'^2)^3},\\
b_3 &= hC_v\frac{R'}{(1+R^2)^2},\\
b_4 &= hC_v\frac{1}{(1+R'^2)^2},\\
b_5 &= \frac{h}{R}\left(\frac{C_v}{R} - \frac{D_vR''}{(1+R'^2)^2}\right),\\
b_6 &= hC_v\frac{R'(RR''(2-R'^2)+R'^2(1+R'^2))}{R(1+R'^2)^3},\\
b_7 &= \frac{h}{1+R'^2}\left(\frac{D_v}{R} - \frac{C_v}{R}\frac{R'^2(R'^2-2R''R+1)+R''R}{(1+R'^2)^2}\right),\\
b_8 &= hC_v\left(\frac{R'}{1+R'^2}\right)^2.
\end{aligned}
$$

2.5 The linearly viscoelastic Koiter shell model for a straight tube

Consider a clamped cylindrical shell with the reference radius of the middle surface equal to $R = const$. Shell thickness is denoted by h and the cylinder length by L. Assume the shell is axially symmetric, so that the displacement in the $\theta-$direction is zero and nothing in the problem depends on θ. Displacement of the shell corresponds to the displacement of shell's middle surface and is denoted by $\boldsymbol{\eta}(z,t) = (\eta_z(z,t), \eta_r(z,t))$. The reference domain is now defined by (see Figure 2.4)

$$\boldsymbol{\Phi} = \{x = (R\cos\theta, R\sin\theta, z) \in \mathbb{R}^3 \ : \ \theta \in (0, 2\pi), z \in (0, L)\}. \tag{2.15}$$

Note that the reference configuration is the same as (2.9) in the case $R(z) = const =$

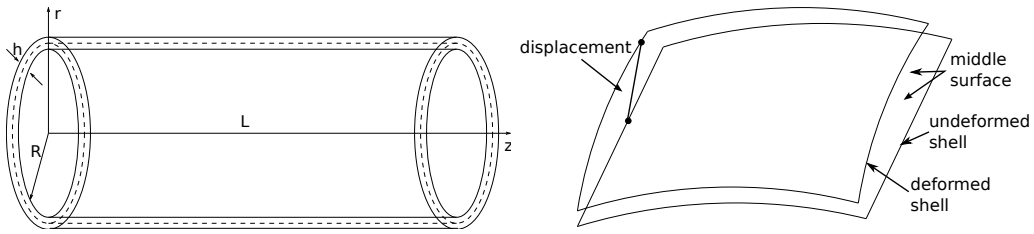

Figure 2.4: Left: Cylindrical shell in reference configuration with middle surface radius R and shell thickness h. Right: Deformed shell.

$R, \forall z \in (0, L)$. Therefore, the first fundamental form of the cylindrical shell in covariant $\mathbf{A}_c = (a_{\alpha\beta})$ and contravariant $\mathbf{A}^c = (a^{\alpha\beta})$ components is given, respectively,

by

$$\mathbf{A}_c = \begin{bmatrix} 1 & 0 \\ 0 & R^2 \end{bmatrix}, \qquad \mathbf{A}^c = \begin{bmatrix} 1 & 0 \\ 0 & \frac{1}{R^2} \end{bmatrix}.$$

Now, using equation (2.11) with $R'(z) = 0, \forall z \in (0, L)$, the change of metric tensor is given by

$$\boldsymbol{\gamma}(\boldsymbol{v}) = \begin{bmatrix} v_z' & 0 \\ 0 & Rv_r \end{bmatrix}, \qquad \forall (v_z, v_r) \in H_0^1(0, L) \times H_0^1(0, L). \tag{2.16}$$

Since we are deriving a shell model we also have to find the change of the curvature tensor to capture bending effects.

Remark 2.5.1. Blouza and Le Dret showed in [14] that linearized change of curvature can be written in the following way

$$\varrho_{\alpha\beta}(\boldsymbol{v}) \;=\; (\partial_{\alpha\beta}\tilde{\boldsymbol{v}} - \Gamma^{\sigma}_{\alpha\beta}\partial_{\sigma}\tilde{\boldsymbol{v}}) \cdot \boldsymbol{a}_3, \tag{2.17}$$

for all $\boldsymbol{v} \in H^1(\omega) \times H^1(\omega) \times H^2(\omega)$, where $\tilde{\boldsymbol{v}} = [\boldsymbol{a}^1\ \boldsymbol{a}^2\ \boldsymbol{a}^3]\,\boldsymbol{v}$.

Using this result together with equations from the previous section, the change of curvature tensor for a cylindrical shell is given by

$$\boldsymbol{\varrho}(\boldsymbol{v}) = \begin{bmatrix} -v_r'' & 0 \\ 0 & v_r \end{bmatrix}, \qquad \forall (v_z, v_r) \in H_0^1(0, L) \times H_0^1(0, L). \tag{2.18}$$

Introduce the following function space

$$\begin{aligned} V_c \;&=\; H_0^1(0, L) \times H_0^2(0, L) \\ &=\; \{\boldsymbol{\xi} = (\xi_z, \xi_r) \in H^1(0, L) :\ \boldsymbol{\xi}(0) = \boldsymbol{\xi}(L) = 0,\ \xi_r'(0) = \xi_r'(L) = 0\}. \end{aligned} \tag{2.19}$$

Then, using equation (2.7) the weak formulation of the linearly viscoelastic Koiter shell model is given by: for each $t > 0$ find $\boldsymbol{\eta}(t) = (\eta_z(t), \eta_r(t)) \in V_c$ such that

$$\begin{aligned}
&\frac{h}{2}\int_0^L \Big(\frac{2E}{1-\sigma^2}\frac{\partial \eta_z}{\partial z}\xi_z' + \frac{2E\sigma}{R(1-\sigma^2)}\eta_r\xi_z' + \frac{2E\sigma}{R(1-\sigma^2)}\frac{\partial \eta_z'}{\partial z}\xi_r + \frac{2E}{R^2(1-\sigma^2)}\eta_r\xi_r \\
&\quad + \frac{2E_v}{1-\sigma_v^2}\frac{\partial^2\eta_z}{\partial z\partial t}\xi_z' + \frac{2E_v\sigma_v}{R(1-\sigma_v^2)}\frac{\partial \eta_r}{\partial t}\xi_z' + \frac{2E_v\sigma_v}{R(1-\sigma_v^2)}\frac{\partial^2\eta_z}{\partial z\partial t}\xi_r + \frac{2E_v}{R^2(1-\sigma_v^2)}\frac{\partial \eta_r}{\partial t}\xi_r\Big)Rdz \\
&+\frac{h^3}{24}\int_0^L \Big(\frac{2E}{1-\sigma^2}\frac{\partial^2\eta_r}{\partial z^2}\xi_r'' - \frac{2E\sigma}{R^2(1-\sigma^2)}\eta_r\xi_r'' - \frac{2E\sigma}{R^2(1-\sigma^2)}\frac{\partial^2\eta_r}{\partial z^2}\xi_r + \frac{2E}{R^4(1-\sigma^2)}\eta_r\xi_r \\
&\quad + \frac{2E_v}{1-\sigma_v^2}\frac{\partial^3\eta_r}{\partial z^2\partial t}\xi_r'' - \frac{2E_v\sigma_v}{R^2(1-\sigma_v^2)}\frac{\partial \eta_r}{\partial t}\xi_r'' - \frac{2E_v\sigma_v}{R^2(1-\sigma_v^2)}\frac{\partial^3\eta_r}{\partial z^2\partial t}\xi_r + \frac{2E_v}{R^4(1-\sigma_v^2)}\frac{\partial \eta_r}{\partial t}\xi_r\Big)Rdz \\
&+\rho_s h\int_0^L (\frac{\partial^2\eta_z}{\partial t^2}\xi_z + \frac{\partial^2\eta_r}{\partial t^2}\xi_r)dz = \int_0^L (f_z\xi_z + f_r\xi_r)Rdz, \qquad \forall \boldsymbol{\xi} = (\xi_z, \xi_r) \in V_c. \qquad (2.20)
\end{aligned}$$

After integration by parts, the equilibrium equations read as follows

$$f_z = \rho_s h\frac{\partial^2\eta_z}{\partial t^2} - C_2\frac{\partial \eta_r}{\partial z} - C_3\frac{\partial^2\eta_z}{\partial z^2} - D_2\frac{\partial^2\eta_r}{\partial t\partial z} - D_3\frac{\partial^3\eta_z}{\partial t\partial z^2} \qquad (2.21)$$

$$\begin{aligned}
f_r = {} & \rho_s h\frac{\partial^2\eta_r}{\partial t^2} + C_0\eta_r - C_1\frac{\partial^2\eta_r}{\partial z^2} + C_2\frac{\partial \eta_z}{\partial z} + C_4\frac{\partial^4\eta_r}{\partial z^4} + D_0\frac{\partial \eta_r}{\partial t} - D_1\frac{\partial^3\eta_r}{\partial t\partial z^2} \\
& + D_2\frac{\partial^2\eta_z}{\partial t\partial z} + D_4\frac{\partial^5\eta_r}{\partial t\partial z^4}, \qquad (2.22)
\end{aligned}$$

where

$$\begin{aligned}
C_0 &= \frac{hE}{R^2(1-\sigma^2)}(1+\frac{h^2}{12R^2}), & C_1 &= \frac{h^3}{6}\frac{E\sigma}{R^2(1-\sigma^2)}, & C_2 &= \frac{h}{R}\frac{E\sigma}{1-\sigma^2}, \\
C_3 &= \frac{hE}{1-\sigma^2}, & C_4 &= \frac{h^3E}{12(1-\sigma^2)} & & \\
D_0 &= \frac{h}{R^2}C_v(1+\frac{h^2}{12R^2}), & D_1 &= \frac{h^3}{6}\frac{D_v}{R^2}, & D_2 &= \frac{hD_v}{R}, \\
D_3 &= hC_v, & D_4 &= \frac{h^3C_v}{12}. & &
\end{aligned} \qquad (2.23)$$

Remark 2.5.2. In the numerical examples we will be using the viscoelastic Koiter shell model neglecting the terms containing the 4th and 5th order derivatives (it can be shown, using non-dimensional analysis, that these terms are much smaller than the remaining terms).

2.5.1 Energy equality of the linearly viscoelastic Koiter shell

In (2.20) we replace the test function $\boldsymbol{\xi}$ by the structure velocity $\frac{\partial \boldsymbol{\eta}}{\partial t}$ and integrate by parts over $(0, L)$ to obtain the following energy equality of the clamped Koiter shell:

$$\begin{aligned}
&\frac{d}{dt}\left\{ \frac{\rho_s h}{2}\left|\left|\frac{\partial \eta_z}{\partial t}\right|\right|^2_{L^2(0,L)} + \frac{\rho_s h}{2}\left|\left|\frac{\partial \eta_r}{\partial t}\right|\right|^2_{L^2(0,L)} \right.\\
&\quad + \frac{h}{2}\left[\frac{E}{1+\sigma}\left|\left|\frac{\eta_r}{R}\right|\right|^2_{L^2(0,L)} + \frac{E}{1+\sigma}\left|\left|\frac{\partial \eta_z}{\partial z}\right|\right|^2_{L^2(0,L)} + \frac{E\sigma}{1-\sigma^2}\left|\left|\frac{\partial \eta_z}{\partial z} + \frac{\eta_r}{R}\right|\right|^2_{L^2(0,L)}\right]\\
&\quad \left. + \frac{h^3}{24}\left[\frac{E}{1+\sigma}\left|\left|\frac{\eta_r}{R^2}\right|\right|^2_{L^2(0,L)} + \frac{E}{1+\sigma}\left|\left|\frac{\partial^2 \eta_r}{\partial z^2}\right|\right|^2_{L^2(0,L)} + \frac{E\sigma}{1-\sigma^2}\left|\left| - \frac{\partial^2 \eta_r}{\partial z^2} + \frac{\eta_r}{R^2}\right|\right|^2_{L^2(0,L)}\right]\right\}\\
&\quad + \frac{h}{2}\left[\frac{E_v}{1+\sigma_v}\left|\left|\frac{\partial \eta_r}{R\partial t}\right|\right|^2_{L^2(0,L)} + \frac{E_v}{1+\sigma_v}\left|\left|\frac{\partial^2 \eta_z}{\partial z \partial t}\right|\right|^2_{L^2(0,L)} + \frac{E_v\sigma_v}{1-\sigma_v^2}\left|\left|\frac{\partial^2 \eta_z}{\partial z \partial t} + \frac{\partial \eta_r}{R\partial t}\right|\right|^2_{L^2(0,L)}\right]\\
&\quad + \frac{h^3}{24}\left[\frac{E_v}{1+\sigma_v}\left|\left|\frac{\partial \eta_r}{R^2\partial t}\right|\right|^2_{L^2(0,L)} + \frac{E_v}{1+\sigma_v}\left|\left|\frac{\partial^3 \eta_r}{\partial z^2 \partial t}\right|\right|^2_{L^2(0,L)} + \frac{E_v\sigma_v}{1-\sigma_v^2}\left|\left| - \frac{\partial^3 \eta_r}{\partial z^2 \partial t} + \frac{\partial \eta_r}{R^2 \partial t}\right|\right|^2_{L^2(0,L)}\right]\\
&\qquad = \int_0^L \mathbf{f} \cdot \frac{\partial \boldsymbol{\eta}}{\partial t}\, d\hat{z}. \qquad (2.24)
\end{aligned}$$

The first two terms under the time-derivative correspond to the kinetic energy of the Koiter shell. The terms in the second and third row correspond to the elastic energy of the Koiter shell (the terms multiplying h are the membrane energy, while the terms multiplying h^3 correspond to the flexural (bending) energy). The terms in the fourth and fifth row correspond to the viscous energy of the viscoelastic Koiter shell, while the last term corresponds to the work done by the external loading.

Denote by $\mathcal{E}_{Ks}$ the contribution from the kinetic and elastic energy:

$$\begin{aligned}\mathcal{E}_{Ks} &= \rho_s h\left|\left|\frac{\partial \eta_z}{\partial t}\right|\right|^2_{L^2(0,L)} + \rho_s h\left|\left|\frac{\partial \eta_r}{\partial t}\right|\right|^2_{L^2(0,L)} + h\left[\frac{E}{1+\sigma}\left|\left|\frac{\eta_r}{R}\right|\right|^2_{L^2(0,L)} + \frac{E}{1+\sigma}\left|\left|\frac{\partial \eta_z}{\partial z}\right|\right|^2_{L^2(0,L)}\right.\\ &\left. + \frac{E\sigma}{1-\sigma^2}\left|\left|\frac{\partial \eta_z}{\partial z} + \frac{\eta_r}{R}\right|\right|^2_{L^2(0,L)}\right] + \frac{h^3}{12}\left[\frac{E}{1+\sigma}\left|\left|\frac{\eta_r}{R^2}\right|\right|^2_{L^2(0,L)} + \frac{E}{1+\sigma}\left|\left|\frac{\partial^2 \eta_r}{\partial z^2}\right|\right|^2_{L^2(0,L)}\right.\\ &\left. + \frac{E\sigma}{1-\sigma^2}\left|\left| - \frac{\partial^2 \eta_r}{\partial z^2} + \frac{\eta_r}{R^2}\right|\right|^2_{L^2(0,L)}\right], \end{aligned} \tag{2.25}$$

and by $\mathcal{V}_{Ks}$ the contribution from the viscous energy:

$$\begin{aligned}\mathcal{V}_{Ks} &= \frac{h}{2}\left[\frac{E_v}{1+\sigma_v}\left|\left|\frac{\partial \eta_r}{R\partial t}\right|\right|^2_{L^2(0,L)} + \frac{E_v}{1+\sigma_v}\left|\left|\frac{\partial^2 \eta_z}{\partial z \partial t}\right|\right|^2_{L^2(0,L)} + \frac{E_v\sigma_v}{1-\sigma_v^2}\left|\left|\frac{\partial^2 \eta_z}{\partial z \partial t} + \frac{\partial \eta_r}{R\partial t}\right|\right|^2_{L^2(0,L)}\right]\\ &+ \frac{h^3}{24}\left[\frac{E_v}{1+\sigma_v}\left|\left|\frac{\partial \eta_r}{R^2\partial t}\right|\right|^2_{L^2(0,L)} + \frac{E_v}{1+\sigma_v}\left|\left|\frac{\partial^3 \eta_r}{\partial z^2 \partial t}\right|\right|^2_{L^2(0,L)}\right.\\ &\left. + \frac{E_v\sigma_v}{1-\sigma_v^2}\left|\left| - \frac{\partial^3 \eta_r}{\partial z^2 \partial t} + \frac{\partial \eta_r}{R^2\partial t}\right|\right|^2_{L^2(0,L)}\right]. \end{aligned}$$

In the case when the external forces are zero, we have the following energy equality:

$$\frac{1}{2}\frac{d}{dt}\mathcal{E}_{Ks} + \mathcal{V}_{Ks} = 0. \tag{2.26}$$

Chapter 3

The Navier-Stokes equations for incompressible viscous fluid in moving domains and the Arbitrary Lagrangian Eulerian (ALE) formulation

3.1 Introduction

A well-accepted model for blood flow in medium-to-large arteries are the Navier-Stokes equations for an incompressible viscous fluid. In this chapter we present the Navier-Stokes equations for an incompressible viscous fluid in moving domains. To resolve the difficulties associated with moving domains we introduce the ALE method. This approach is widely used in numerical studies of the fluid-structure

interaction problems [32, 48, 50, 61, 77, 78].

3.2 The Navier-Stokes equations for an incompressible viscous fluid in moving domains

We consider the flow of an incompressible, viscous fluid in a two-dimensional channel of length L and reference width 2R. The lateral boundary of the channel is bounded by a thin, deformable wall. Without loss of generality, we consider only the upper half of the fluid domain supplemented by a symmetry conditions at the axis of symmetry. We assume the tube is fixed at the edges, i.e., the length of the tube does not change.

We will be assuming that for each $t \in (0, T)$ the boundary of the fluid domain is Lipschitz continuous and that its lateral boundary, in Eulerian framework, can be described by a Lipschitz continuous function

$$g(\cdot\,; t) : (0, L) \to \mathbb{R}, \quad g(\cdot\,; t) : z \mapsto g(z; t) \quad \text{for each} \quad t \in (0, T),$$

so that, in Eulerian framework,

$$\Gamma(t) = \{(z, g(z; t)), z \in (0, L)\} \quad \text{for} \quad t \in (0, T),$$

where z and r denote the horizontal and vertical Cartesian coordinates, respectively. The fluid domain is given by (see Figure 3.1)

$$\Omega(t) = \{(z, r) \in \mathbb{R}^2;\ 0 < z < L,\ 0 < r < g(z; t)\}, \quad \text{for} \quad t \in (0, T). \tag{3.1}$$

The inlet boundary will be denoted by Γ_{in}, the outlet boundary by Γ_{out}, the sym-

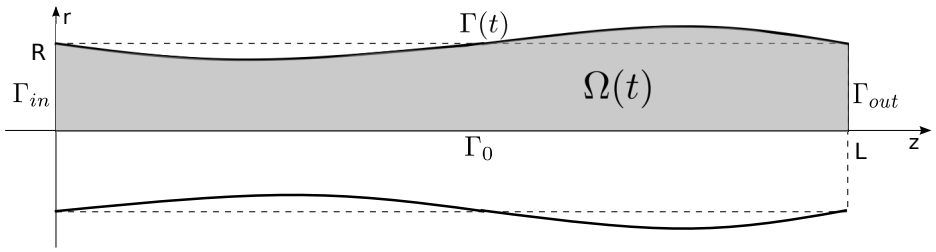

Figure 3.1: Fluid domain $\Omega(t)$.

metry (bottom) boundary for which $r = 0$ by Γ_b, so that

$$\partial\Omega(t) = \Gamma_{\text{in}} \cup \Gamma(t) \cup \Gamma_{\text{out}} \cup \Gamma_b.$$

The flow of a viscous, incompressible, Newtonian fluid is governed by the Navier-Stokes equations

$$\rho_f\left(\frac{\partial \boldsymbol{u}}{\partial t} + \boldsymbol{u}\cdot\nabla\boldsymbol{u}\right) = \nabla\cdot\boldsymbol{\sigma} \quad \text{in } \Omega(t) \text{ for } t \in (0,T), \tag{3.2}$$

$$\nabla\cdot\boldsymbol{u} = 0 \quad \text{in } \Omega(t) \text{ for } t \in (0,T), \tag{3.3}$$

where $\boldsymbol{u} = (u_z, u_r)$ is the fluid velocity, p is the fluid pressure, ρ_f is the fluid density, and $\boldsymbol{\sigma}$ is the fluid stress tensor. We assume the fluid is Newtonian so that the fluid stress tensor is given by $\boldsymbol{\sigma} = -p\boldsymbol{I} + 2\mu\boldsymbol{D}(\boldsymbol{u})$, where μ is the fluid viscosity and $\boldsymbol{D}(\boldsymbol{u}) = (\nabla\boldsymbol{u} + (\nabla\boldsymbol{u})^\tau)/2$ is the rate-of-strain tensor.

At the inlet and outlet boundary we prescribe the normal stress:

$$\boldsymbol{\sigma}\mathbf{n}|_{in}(0,r,t) = -p_{in}(t)\mathbf{n}|_{in} \quad \text{on } (0,R)\times(0,T), \tag{3.4}$$

$$\boldsymbol{\sigma}\mathbf{n}|_{out}(L,r,t) = -p_{out}(t)\mathbf{n}|_{out} \quad \text{on } (0,R)\times(0,T), \tag{3.5}$$

where $\mathbf{n}_{in}/\mathbf{n}_{out}$ are the outward normals to the inlet/outlet boundaries, respectively. Even though not physiologically optimal, these boundary conditions are common in blood flow modeling [8, 65, 70].

At the bottom boundary Γ_b we impose the symmetry conditions

$$\frac{\partial u_z}{\partial r}(z,0,t) = 0, \quad u_r(z,0,t) = 0 \quad \text{on } (0,L)\times(0,T). \tag{3.6}$$

The upper boundary $\Gamma(t)$ represents a moving channel wall. Here we prescribe the no-slip boundary conditions for the fluid velocity

$$\boldsymbol{u} = \boldsymbol{u}_D \quad \text{on } \Gamma(t), \text{ for } t \in (0,T).$$

When considering a fluid-structure interaction problem the no-slip condition will be supplemented by an additional condition describing the balance of contact forces.

Initially, the fluid is assumed to be at rest

$$\boldsymbol{u} = 0,$$

with the moving wall in the reference configuration.

3.3 The ALE mapping

To deal with the motion of the fluid domain we adopt the Arbitrary Lagrangian-Eulerian (ALE) approach [32, 50, 70]. In the context of finite element method approximation of moving-boundary problems, ALE method deals efficiently with the deformation of the mesh, especially near the interface between the fluid and structure.

Denote by $\hat{\Omega} := (0,L)\times(0,R)$ the reference domain, and let $\Omega(t)$ be a current domain. A point $\hat{\boldsymbol{x}} \in \hat{\Omega}$ is called the ALE coordinate, while $\boldsymbol{x} = \boldsymbol{x}(\hat{\boldsymbol{x}},t) \in \Omega(t)$

is called the Eulerian coordinate. ALE approach is based on introducing a family of (arbitrary, invertible, smooth) mappings $\mathcal{A}_t$ defined on a single, fixed, reference domain $\hat{\Omega}$ such that, for each $t \in (t_0, T)$, $\mathcal{A}_t$ maps the reference domain $\hat{\Omega} = (0, L) \times (0, R)$ into the current domain $\Omega(t)$ (see Figure 3.2):

$$\mathcal{A}_t : \hat{\Omega} \subset \mathbb{R}^d \to \Omega(t) \subset \mathbb{R}^d, \quad \boldsymbol{x}(\hat{\boldsymbol{x}}, t) = \mathcal{A}_t(\hat{\boldsymbol{x}}) \in \Omega(t), \quad \text{for } \hat{\boldsymbol{x}} \in \hat{\Omega}. \tag{3.7}$$

In addition, assume that the mapping

$$t \to \boldsymbol{x}(\hat{\boldsymbol{x}}, t)$$

is differentiable almost everywhere in $[0, T]$.

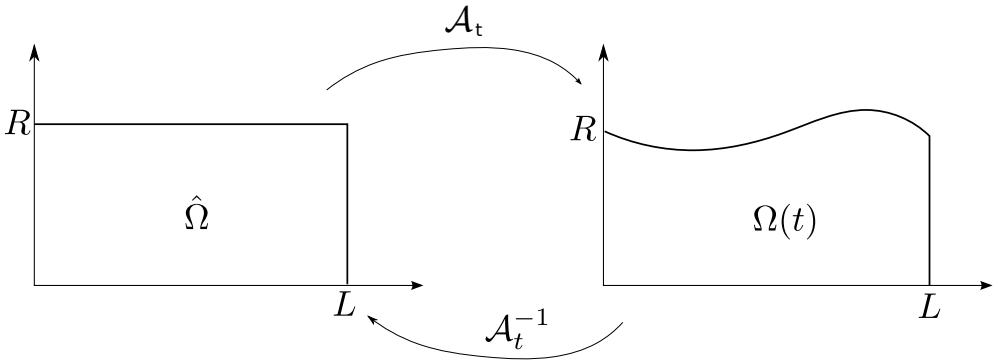

Figure 3.2: $\mathcal{A}_t$ maps the reference domain $\hat{\Omega}$ into the current domain $\Omega(t)$.

Let $f = f(\boldsymbol{x}, t)$ be a function defined on $\Omega(t) \times (t_0, T)$ and $\hat{f} := f \circ \mathcal{A}_t$ the corresponding function defined on $\hat{\Omega} \times (t_0, T)$ given by

$$\hat{f}(\hat{\boldsymbol{x}}, t) = f(\mathcal{A}_t(\hat{\boldsymbol{x}}), t). \tag{3.8}$$

Define the time derivative of f on the reference configuration, in notation $\frac{\partial f}{\partial t}\big|_{\hat{\boldsymbol{x}}}$, in the following way

$$\left.\frac{\partial f}{\partial t}\right|_{\hat{\boldsymbol{x}}} (\boldsymbol{x}, t) := \frac{\partial \hat{f}}{\partial t}(\mathcal{A}_t^{-1}(\boldsymbol{x}), t). \tag{3.9}$$

Using this notation, differentiating the function f defined in (3.8) using the chain rule we have

$$\left.\frac{\partial f}{\partial t}\right|_{\hat{\boldsymbol{x}}} = \frac{\partial f}{\partial t} + \left(\frac{\partial \mathcal{A}_t}{\partial t} \circ \mathcal{A}_t^{-1}(\boldsymbol{x})\right) \cdot \nabla f = \frac{\partial f}{\partial t} + \boldsymbol{w} \cdot \nabla f, \tag{3.10}$$

where ∇ denotes the gradient with respect to $\boldsymbol{x}$ and

$$\boldsymbol{w} = \frac{\partial \mathcal{A}_t}{\partial t} \circ \mathcal{A}_t^{-1}(\boldsymbol{x}) = \left.\frac{\partial \boldsymbol{x}}{\partial t}\right|_{\hat{\boldsymbol{x}}} \tag{3.11}$$

denotes domain velocity.

3.4 The ALE formulation of the Navier-Stokes equations in conservative and non-conservative form

When dealing with moving domains in practice, it is natural to work with variables that follow the domain evolution. Suppose we have a moving mesh and let $\boldsymbol{x}_{t^n}$ and $\boldsymbol{x}_{t^{n+1}}$ be the corresponding mesh nodes in the mesh at times t^n and t^{n+1}, as in Figure 3.3. A natural way of discretizing the time-derivative of a function $\boldsymbol{u} \in$

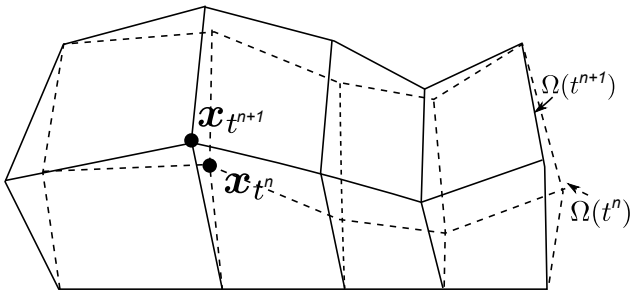

Figure 3.3: Example of a moving mesh.

$\Omega(t^{n+1})$ is via the forward difference

$$\frac{\partial \boldsymbol{u}}{\partial t}(\boldsymbol{x}_{t^{n+1}}, t^{n+1}) \approx \frac{\boldsymbol{u}(\boldsymbol{x}_{t^{n+1}}, t^{n+1}) - \boldsymbol{u}(\boldsymbol{x}_{t^n}, t^n)}{t^{n+1} - t^n}.$$

However, a point $\boldsymbol{x}_{t^{n+1}}$ that belongs to $\Omega(t^{n+1})$ does not have to necessarily belong to $\Omega(t^n)$. Since the two terms that define the discrete form of the time derivative are not defined on same domains, the approximation of the time-derivative is not well defined. For this reason it is necessary to map the function $\boldsymbol{u}$ back to the reference domain before discretizing the time derivatives. Using relation (3.10), for a function $\boldsymbol{u}$ defined on a moving domain we can write

$$\frac{\partial \boldsymbol{u}}{\partial t} = \left.\frac{\partial \boldsymbol{u}}{\partial t}\right|_{\hat{\boldsymbol{x}}} - \boldsymbol{w} \cdot \nabla \boldsymbol{u}, \tag{3.12}$$

where $\boldsymbol{w}$ is domain velocity and $\left.\frac{\partial \boldsymbol{u}}{\partial t}\right|_{\hat{\boldsymbol{x}}}$ is derivative of $\boldsymbol{u}$ on the reference domain.

We apply this rule to write the time-derivative of the velocity in Navier-Stokes equations (3.2)-(3.3) on the reference domain. Using equation (3.12), the ALE formulation of the Navier-Stokes equations in non-conservative form is given by

$$\rho_f \left(\left.\frac{\partial \boldsymbol{u}}{\partial t}\right|_{\hat{\boldsymbol{x}}} + (\boldsymbol{u} - \boldsymbol{w}) \cdot \nabla \boldsymbol{u} \right) = \nabla \cdot \boldsymbol{\sigma} \quad \text{in } \Omega(t) \text{ for } t \in (0, T), \tag{3.13}$$

$$\nabla \cdot \boldsymbol{u} = 0 \quad \text{in } \Omega(t) \text{ for } t \in (0, T), \tag{3.14}$$

with appropriate initial and boundary conditions.

Remark 3.4.1. In the general case $\boldsymbol{w}(\boldsymbol{x}, t) \neq \boldsymbol{u}(\boldsymbol{x}, t)$. However, let us point out two special cases:

- $\boldsymbol{w} = 0$: the domain is fixed, i.e. $\Omega(t) = \hat{\Omega}$. In this case we recover the Eulerian description of the motion.

- $\boldsymbol{w} = \boldsymbol{u} : \Omega(t)$ is the material domain. In this case we recover the Lagrangian description of the motion.

To derive the conservative formulation we introduce the following proposition [43]

Proposition 3.4.1. *The following identity holds*

$$\frac{\partial J_{\mathcal{A}}}{\partial t}(\hat{\boldsymbol{x}}, t) = J_{\mathcal{A}}(\hat{\boldsymbol{x}}, t)\, \nabla \cdot \boldsymbol{w}(\mathcal{A}_t(\hat{\boldsymbol{x}}), t), \qquad \forall \hat{\boldsymbol{x}} \in \hat{\Omega}, \forall t > 0, \tag{3.15}$$

where $J_{\mathcal{A}}$ is Jacobian of $\mathcal{A}_t$.

Using Proposition 3.4.1 one can show the following equality

$$\left.\frac{\partial \boldsymbol{u}}{\partial t}\right|_{\hat{\boldsymbol{x}}} = \frac{1}{J_{\mathcal{A}}}\left(\left.\frac{\partial (J_{\mathcal{A}}\boldsymbol{u})}{\partial t}\right|_{\hat{\boldsymbol{x}}} - J_{\mathcal{A}}\boldsymbol{u}\nabla \cdot \boldsymbol{w}\right). \tag{3.16}$$

Replacing the material derivative in (3.13) with the relation (3.16) and using

$$\nabla \cdot (\boldsymbol{u} \otimes \boldsymbol{w}) = \boldsymbol{u}\nabla \cdot \boldsymbol{w} + \boldsymbol{w} \cdot \nabla \boldsymbol{u},$$

we obtain the ALE formulation of the incompressible Navier-Stokes equations in conservative form

$$\frac{\rho_f}{J_{\mathcal{A}}}\left.\frac{\partial (J_{\mathcal{A}}\boldsymbol{u})}{\partial t}\right|_{\hat{\boldsymbol{x}}} + \nabla \cdot \Big(\rho_f \boldsymbol{u} \otimes (\boldsymbol{u} - \boldsymbol{w}) - \boldsymbol{\sigma}\Big) = 0 \quad \text{in } \Omega(t) \text{ for } t \in (0, T), \tag{3.17}$$

$$\nabla \cdot \boldsymbol{u} = 0 \quad \text{in } \Omega(t) \text{ for } t \in (0, T), \tag{3.18}$$

with appropriate initial and boundary conditions.

3.5 Construction of the ALE mapping

Assume we know the motion of the interface

$$\boldsymbol{h} : \partial\hat{\Omega} \times (0, T) \to \partial\Omega(t).$$

We want to find an ALE mapping $\mathcal{A}_t$ such that

$$\mathcal{A}_t(\hat{\boldsymbol{x}}) = \boldsymbol{h}(\hat{\boldsymbol{x}}, t), \quad \forall \hat{\boldsymbol{x}} \in \partial\hat{\Omega},\ t \in (0, T).$$

Since $\mathcal{A}_t(\hat{\boldsymbol{x}}) = \boldsymbol{x}(\hat{\boldsymbol{x}}, t)$ and $\mathcal{A}_t$ is arbitrary inside $\hat{\Omega}$, we can assume $\boldsymbol{x}$ is any "reasonable" extension of $\boldsymbol{h}$ over $\hat{\Omega}$

$$\boldsymbol{x} = \mathrm{Ext}(\boldsymbol{h}).$$

A simple model for finding such an $\boldsymbol{x}$ is the following:

Problem 3.5.1. *Find $\boldsymbol{x} : \hat{\Omega} \times (0, T) \to \Omega(t)$ such that*

$$\frac{\partial \boldsymbol{x}}{\partial t} - \nabla_{\hat{\boldsymbol{x}}} \cdot (\kappa \nabla_{\hat{\boldsymbol{x}}} \boldsymbol{x}) = 0, \quad \forall \hat{\boldsymbol{x}} \in \hat{\Omega},\ t \in (0, T), \tag{3.19}$$

$$\boldsymbol{x}(\hat{\boldsymbol{x}}, 0) = \hat{\boldsymbol{x}}, \qquad \hat{\boldsymbol{x}} \in \hat{\Omega}, \tag{3.20}$$

$$\boldsymbol{x}(\hat{\boldsymbol{x}}, t) = \boldsymbol{h}(\hat{\boldsymbol{x}}, t), \qquad \hat{\boldsymbol{x}} \in \partial\hat{\Omega},\ t \in (0, T), \tag{3.21}$$

where κ is a positive constant.

In the case when we do not have a prescribed motion given for all times t, a numerical method only has an input for the time interval (t^n, t^{n+1}) which consists of the reference domain and the new position of the boundary, in notation $\tilde{\boldsymbol{h}} : \partial\hat{\Omega} \to \partial\Omega(t)$, a simple choice for the function $\boldsymbol{x}$ is a harmonic extension of $\tilde{\boldsymbol{h}}$ onto $\hat{\Omega}$:

Problem 3.5.2. *Find $\boldsymbol{x} : \hat{\Omega} \to \Omega(t)$ such that*

$$\nabla_{\hat{\boldsymbol{x}}} \cdot (\kappa \nabla_{\hat{\boldsymbol{x}}} \boldsymbol{x}) = 0, \quad \forall \hat{\boldsymbol{x}} \in \hat{\Omega}, \tag{3.22}$$

$$\boldsymbol{x}(\hat{\boldsymbol{x}}) = \tilde{\boldsymbol{h}}(\hat{\boldsymbol{x}}), \qquad \hat{\boldsymbol{x}} \in \partial\hat{\Omega}, \tag{3.23}$$

where κ is a positive constant (in the simplest case $\kappa = 1$).

In our approach, we define $\mathcal{A}_t$ to be the harmonic extension of the mapping $\hat{\boldsymbol{g}}$ that maps the boundary of $\hat{\Omega}$ to the boundary of $\Omega(t)$ for a given time t. More precisely, in our case $\hat{\Omega} := (0, L) \times (0, R)$, and so $\mathcal{A}_t$ is a harmonic extension of

$$\hat{\boldsymbol{g}} : \partial\hat{\Omega} \to \partial\Omega(t)$$

onto the whole domain $\hat{\Omega}$, for a given t :

Problem 3.5.3. *Find* $\boldsymbol{x} : \hat{\Omega} \to \Omega(t)$ *such that*

$$\Delta_{\hat{\boldsymbol{x}}}\boldsymbol{x} = 0, \qquad \forall \hat{\boldsymbol{x}} \in \hat{\Omega}, \tag{3.24}$$

$$\boldsymbol{x}(\hat{\boldsymbol{x}}) = 0, \qquad \hat{\boldsymbol{x}} \in \hat{\Omega} \backslash \partial\hat{\Omega}, \tag{3.25}$$

$$\boldsymbol{x}(\hat{\boldsymbol{x}}) = \hat{\boldsymbol{g}}(\hat{\boldsymbol{x}}), \qquad \hat{\boldsymbol{x}} \in \partial\hat{\Omega}. \tag{3.26}$$

Chapter 4

The fluid-structure interaction problem

4.1 The coupling conditions and formulation of the fluid-structure interaction problem

Consider the flow of an incompressible viscous fluid in a two-dimensional channel. Without loss of generality, we consider only the upper half of the fluid domain supplemented by a symmetry condition at the axis of symmetry (see Figure 3.1). The lateral boundary of the channel is bounded by a thin, deformable wall. We model the fluid flow by the Navies-Stokes equations for an incompressible viscous fluid (3.3)-(3.6), and the motion of the wall by the linearly viscoelastic Koiter shell model (2.22)-(2.23). We are interested in simulating a pressure-driven flow through the deformable 2D channel with a two-way coupling between the fluid and structure.

The fluid domain, which depends on time, is not known *a priori*. The location

of the lateral boundary, defined in Lagrangian framework, is given by $\Gamma(t) = \{(\hat{z} + \eta_z(\hat{z}, t), R + \eta_r(\hat{z}, t)) \mid \hat{z} \in (0, L)\}$ for $t \in (0, T)$. Throughout the rest of this thesis we will be denoting the Lagrangian coordinates by $\hat{\mathbf{x}} = (\hat{z}, \hat{r})$. The displacement of the boundary will always be given in Lagrangian framework. However, we will omit the hat notation on $\boldsymbol{\eta}$ for simplicity.

The fluid and structure are coupled via the kinematic and dynamic boundary conditions [20]:

- **Kinematic boundary condition** describes continuity of velocity: the fluid velocity at the current interface $\Gamma(t)$ equals the velocity of the structure:

$$\mathbf{u}(\hat{z} + \eta_z(\hat{z}, t), R + \eta_r(\hat{z}, t), t) = \frac{\partial \boldsymbol{\eta}}{\partial t}(\hat{z}, t) \quad \text{on } (0, L) \times (0, T). \tag{4.1}$$

- **Dynamic coupling condition** describes balance of forces: the contact force exerted by the fluid to the structure is counterbalanced by the contact force of the structure. The fluid contact force, typically given in Eulerian framework, is given by the normal fluid stress $\boldsymbol{\sigma n}$ on $\Gamma(t)$, where $\boldsymbol{n}$ is the outward normal to the deformed boundary $\Gamma(t)$. Let $\boldsymbol{F} = (f_z, f_r)$ denote the force of the structure to the fluid-structure interface. Then, for every Borel subset $B \in \hat{\Gamma}$, we require

$$\begin{aligned} \int_B \sqrt{\left(1 + \frac{\partial \eta_z}{\partial z}\right)^2 + \left(\frac{\partial \eta_r}{\partial z}\right)^2}\, \widehat{\boldsymbol{\sigma n}}|_{\Gamma(t)} \cdot \boldsymbol{e}_z dz &= -\int_B f_z dz, \\ \int_B \sqrt{\left(1 + \frac{\partial \eta_z}{\partial z}\right)^2 + \left(\frac{\partial \eta_r}{\partial z}\right)^2}\, \widehat{\boldsymbol{\sigma n}}|_{\Gamma(t)} \cdot \boldsymbol{e}_r dz &= -\int_B f_r dz, \end{aligned}$$

  where

$$J := \sqrt{\left(1 + \frac{\partial \eta_z}{\partial z}\right)^2 + \left(\frac{\partial \eta_r}{\partial z}\right)^2} \tag{4.2}$$

is the Jacobian determinant of the mapping transforming $\Gamma(t)$ to $\hat{\Gamma}$. Pointwise, the balance of contact forces reads

$$-f_z = J\widehat{\boldsymbol{\sigma}\boldsymbol{n}}|_{\Gamma(t)} \cdot \boldsymbol{e}_z, \quad \text{on } \hat{\Gamma} \times (0,T), \tag{4.3}$$

$$-f_r = J\widehat{\boldsymbol{\sigma}\boldsymbol{n}}|_{\Gamma(t)} \cdot \boldsymbol{e}_r, \quad \text{on } \hat{\Gamma} \times (0,T). \tag{4.4}$$

Now, we define the fluid-structure interaction problem, written in the ALE framework, as the following problem:

Problem 4.1.1.

$$\begin{aligned}
&\rho_f\left(\tfrac{\partial \boldsymbol{u}}{\partial t}\big|_{\hat{\boldsymbol{x}}} + (\boldsymbol{u}-\boldsymbol{w})\cdot\nabla\boldsymbol{u}\right) = \nabla\cdot\boldsymbol{\sigma} && \text{in } \Omega(t)\times(0,T),\\
&\nabla\cdot\boldsymbol{u} = 0 && \text{in } \Omega(t)\times(0,T),\\
&\tfrac{\partial \boldsymbol{\eta}}{\partial t} = \boldsymbol{u}|_{\Gamma(t)} && \text{on } (0,L)\times(0,T),\\
&\rho_s h\tfrac{\partial^2\eta_z}{\partial t^2} - C_2\tfrac{\partial\eta_r}{\partial z} - C_3\tfrac{\partial^2\eta_z}{\partial z^2} - D_2\tfrac{\partial^2\eta_r}{\partial t\partial z} - D_3\tfrac{\partial^3\eta_z}{\partial t\partial z^2} = f_z && \text{on } (0,L)\times(0,T),\\
&\rho_s h\tfrac{\partial^2\eta_r}{\partial t^2} + C_0\eta_r - C_1\tfrac{\partial^2\eta_r}{\partial z^2} + C_2\tfrac{\partial\eta_z}{\partial z} + D_0\tfrac{\partial\eta_r}{\partial t} - D_1\tfrac{\partial^3\eta_r}{\partial t\partial z^2}\\
&\qquad + D_2\tfrac{\partial^2\eta_z}{\partial t\partial z} = f_r && \text{on } (0,L)\times(0,T),
\end{aligned}$$

with the following boundary and initial conditions

$$\begin{aligned}
&\frac{\partial u_z}{\partial r}(z,0,t) = u_r(z,0,t) = 0 \quad \text{on } (0,L)\times(0,T),\\
&\boldsymbol{u}(0,R,t) = \boldsymbol{u}(L,R,t) = 0, \quad \boldsymbol{\eta}(0,t) = \boldsymbol{\eta}(L,t) = 0,\\
&\boldsymbol{\sigma}\mathbf{n}|_{in}(0,r,t) = -p_{in}(t)\mathbf{n}|_{in},\ \boldsymbol{\sigma}\mathbf{n}|_{out}(L,r,t) = -p_{out}(t)\mathbf{n}|_{out} \ \text{ on } (0,R)\times(0,T),\\
&\boldsymbol{u}|_{t=0} = \mathbf{0}, \quad \boldsymbol{\eta}|_{t=0} = \mathbf{0}, \quad \left.\frac{\partial\boldsymbol{\eta}}{\partial t}\right|_{t=0} = \mathbf{0} \quad \text{on } \hat{\Omega}.
\end{aligned} \tag{4.5}$$

Remark 1. It is worth mentioning here that while the fluid flow is modeled in 2D, the thin structure equations, described in the previous section, are given in terms

of cylindrical coordinates, assuming axial symmetry. It is standard practice in 2D fluid-structure interaction studies to use thin structure equations that are derived assuming cylindrical geometry. This is because cylindrical structure models account for the circumferential stress that "keeps" the top and bottom boundary of the structure "coupled together" when they are loaded by the stresses exerted by the fluid, thereby giving rise to physiologically reasonable solutions.

4.2 Variational formulation and the energy equality for the coupled FSI system

4.2.1 Variational formulation

Define the space of test functions

$$\begin{aligned} V(t) &= \{\boldsymbol{v} : \Omega(t) \to \mathbb{R}^2 |\ \boldsymbol{v} = \hat{\boldsymbol{v}} \circ (\mathcal{A}_t)^{-1}, \hat{\boldsymbol{v}} \in (H^1(\hat{\Omega}))^2, v_r|_{r=0} = 0, \\ &\qquad \boldsymbol{v}|_{\Gamma(t)} \in H_0^1(\Gamma(t))\}, \qquad (4.6) \\ Q(t) &= \{q : \Omega(t) \to \mathbb{R} |\ q = \hat{q} \circ (\mathcal{A}_t)^{-1}, \hat{q} \in L^2(\hat{\Omega})\}, \qquad (4.7) \end{aligned}$$

for all $t \in [0, T)$. The variational formulation of Problem 4.1.1 reads: given $t \in (0, T)$, find $(\boldsymbol{u}, p, \boldsymbol{\eta}(t)) \in V(t) \times Q(t) \times V_c$ such that for all $(\boldsymbol{v}, q) \in V(t) \times Q(t)$

$$\rho_f \int_{\Omega(t)} \frac{\partial \boldsymbol{u}}{\partial t} \cdot \boldsymbol{v} d\boldsymbol{x} + 2\mu \int_{\Omega(t)} \boldsymbol{D}(\boldsymbol{u}) : \boldsymbol{D}(\boldsymbol{v}) d\boldsymbol{x} - \int_{\Omega(t)} p \nabla \cdot \boldsymbol{v} d\boldsymbol{x}$$

$$+ \int_0^L \left(\rho_s h \frac{\partial^2 \eta_z}{\partial t^2} - C_2 \frac{\partial \eta_r}{\partial z} - D_2 \frac{\partial^2 \eta_r}{\partial t \partial z} \right) v_z|_{\hat{\Gamma}} d\hat{z} + \int_0^L \left(C_3 \frac{\partial \eta_z}{\partial z} + D_3 \frac{\partial^2 \eta_z}{\partial t \partial z} \right) \frac{\partial (v_z|_{\hat{\Gamma}})}{\partial z} d\hat{z}$$

$$+\int_0^L \left(\rho_s h\frac{\partial^2\eta_r}{\partial t^2}+C_0\eta_r+C_2\frac{\partial\eta_z}{\partial z}+D_0\frac{\partial\eta_r}{\partial t}+D_2\frac{\partial^2\eta_z}{\partial t\partial z}\right)v_r|_{\hat{\Gamma}}d\hat{z}$$
$$+\int_0^L \left(C_1\frac{\partial\eta_r}{\partial z}+D_1\frac{\partial^2\eta_r}{\partial t\partial z}\right)\frac{\partial(v_r|_{\hat{\Gamma}})}{\partial z}d\hat{z}=\int_0^R p_{in}(t)v_z|_{z=0}dr-\int_0^R p_{out}(t)v_z|_{z=L}dr,$$

and

$$\int_{\Omega(t)} q\nabla\cdot\boldsymbol{u}d\boldsymbol{x}=0.$$

4.2.2 The energy of the coupled FSI problem

To formally derive the energy of the coupled FSI problem we multiply the structure equations by the structure velocity, the balance of momentum in the fluid equations by the fluid velocity, integrate by parts over the respective domains using the incompressibility condition, and add the two equations together. The dynamic and kinematic coupling conditions are then used to couple the fluid and structure sub-problems.

We start by first considering the Navier-Stokes equations for the fluid. To find the energy of the fluid sub-problem we multiply the momentum equation in the Navier-Stokes equations by $\boldsymbol{u}$ and integrate by parts over $\Omega(t)$, using the incompressibility condition along the way. With the help of the following identities

$$\begin{aligned}\int_{\Omega(t)}\frac{\partial\boldsymbol{u}}{\partial t}\boldsymbol{u}d\boldsymbol{x} &= \frac{1}{2}\frac{d}{dt}\int_{\Omega(t)}|\boldsymbol{u}|^2d\boldsymbol{x}-\frac{1}{2}\int_{\partial\Omega(t)}|\boldsymbol{u}|^2\boldsymbol{u}\cdot\boldsymbol{n}dS,\\ \int_{\Omega(t)}(\boldsymbol{u}\cdot\nabla)\boldsymbol{u}\cdot\boldsymbol{u}d\boldsymbol{x} &= \frac{1}{2}\int_{\partial\Omega(t)}|\boldsymbol{u}|^2\boldsymbol{u}\cdot\boldsymbol{n}dS,\end{aligned}$$

one obtains

$$\frac{1}{2}\frac{d}{dt}\left\{\rho_f||\boldsymbol{u}||^2_{L^2(\Omega(t))}\right\} + 2\mu||\boldsymbol{D}(\boldsymbol{u})||^2_{L^2(\Omega(t))}$$
$$-\int_0^R p_{in}(t)u_z|_{z=0}dr + \int_0^R p_{out}(t)u_z|_{z=L}dr = \int_{\Gamma(t)} \boldsymbol{\sigma}\mathbf{n}\cdot\boldsymbol{u}\ dS.$$

The integral on the right-hand side can be written in Lagrangian coordinates as

$$\int_{\Gamma(t)} \boldsymbol{\sigma}\mathbf{n}\cdot\boldsymbol{u}\ dS = \int_0^L \left[\boldsymbol{\sigma}\mathbf{n}\cdot\boldsymbol{u}\right]|_{(\hat{z}+\eta_z(\hat{z},t),R+\eta_r(\hat{z},t))}\ J\ d\hat{z} \tag{4.8}$$

where J is the Jacobian of transformation from the Eulerian to Lagrangian framework, given by (4.2). Now we use the kinematic (4.1) and dynamic (4.3)-(4.4) lateral boundary conditions to obtain

$$\int_0^L \left[\boldsymbol{\sigma}\mathbf{n}\cdot\boldsymbol{u}\right]|_{(\hat{z}+\eta_z(\hat{z},t),R+\eta_r(\hat{z},t))}\ J\ d\hat{z} = -\int_0^L \mathbf{f}\cdot\frac{\partial\boldsymbol{\eta}}{\partial t}\ d\hat{z}. \tag{4.9}$$

Thus, the fluid sub-problem coupled with the structure satisfies

$$\tfrac{1}{2}\tfrac{d}{dt}\left\{\rho_f||\boldsymbol{u}||^2_{L^2(\Omega(t))}\right\} + 2\mu||\boldsymbol{D}(\boldsymbol{u})||^2_{L^2(\Omega(t))}$$

$$-\int_0^R p_{in}(t)u_z|_{z=0}dr + \int_0^R p_{out}(t)u_z|_{z=L}dr = -\int_0^L \mathbf{f}\cdot\frac{\partial\boldsymbol{\eta}}{\partial t}\ d\hat{z}. \tag{4.10}$$

By adding (2.24) and (4.10), the right-hand sides of the two equations cancel out and one obtains the energy equality for the FSI problem:

$$\tfrac{d}{dt}\Bigg\{ \underbrace{\frac{\rho_f}{2}||\boldsymbol{u}||^2_{L^2(\Omega(t))} + \frac{\rho_s h}{2}\left|\left|\frac{\partial\eta_z}{\partial t}\right|\right|^2_{L^2(0,L)} + \frac{\rho_s h}{2}\left|\left|\frac{\partial\eta_r}{\partial t}\right|\right|^2_{L^2(0,L)}}_{Kinetic\ Energy}$$
$$+\tfrac{h}{2}\underbrace{\left[\frac{E}{1+\sigma}\left|\left|\frac{\eta_r}{R}\right|\right|^2_{L^2(0,L)} + \frac{E}{1+\sigma}\left|\left|\frac{\partial\eta_z}{\partial z}\right|\right|^2_{L^2(0,L)} + \frac{E\sigma}{1-\sigma^2}\left|\left|\frac{\partial\eta_z}{\partial z} + \frac{\eta_r}{R}\right|\right|^2_{L^2(0,L)}\right]}_{Structure\ Elastic\ Energy\ (Membrane\ Contribution)}$$
$$+\tfrac{h^3}{24}\underbrace{\left[\frac{E}{1-\sigma^2}\left|\left|\frac{\eta_r}{R^2}\right|\right|^2_{L^2(0,L)} + \frac{2E\sigma}{1-\sigma^2}\left|\left|\frac{\partial^2\eta_r}{\partial z^2}\right|\right|^2_{L^2(0,L)}\right]}_{Structure\ Elastic\ Energy\ (Flexural(Shell)\ Contribution)}\Bigg\}$$

$$+\frac{h}{2}\underbrace{\left[\frac{E_v}{1+\sigma_v}\left|\left|\frac{\partial\eta_r}{R\partial t}\right|\right|^2_{L^2(0,L)}+\frac{E_v}{1+\sigma_v}\left|\left|\frac{\partial^2\eta_z}{\partial z\partial t}\right|\right|^2_{L^2(0,L)}+\frac{E_v\sigma_v}{1-\sigma_v^2}\left|\left|\frac{\partial^2\eta_z}{\partial z\partial t}+\frac{\partial\eta_r}{R\partial t}\right|\right|^2_{L^2(0,L)}\right]}_{Structure\ Viscous\ Energy\ (Membrane\ Contribution)}$$

$$+\frac{h^3}{24}\underbrace{\left[\frac{E_v}{1-\sigma_v^2}\left|\left|\frac{\partial\eta_r}{R^2\partial t}\right|\right|^2_{L^2(0,L)}+\frac{2E_v}{1-\sigma_v^2}\left|\left|\frac{\partial^3\eta_r}{\partial z^2\partial t}\right|\right|^2_{L^2(0,L)}\right]}_{Structure\ Viscous\ Energy\ (Flexural\ (Shell)\ Contribution)}+\underbrace{2\mu||\boldsymbol{D}(\boldsymbol{u})||^2_{L^2(\Omega(t))}}_{Fluid\ Viscous\ Energy}$$

$$=\int_0^R p_{in}(t)u_z|_{z=0}dr-\int_0^R p_{out}(t)u_z|_{z=L}dr. \tag{4.11}$$

The coefficients E_v and σ_v are defined in Chapter 1. Therefore, we have shown that if a solution to the coupled fluid-structure interaction problem (2.21) - (4.4) exists, then it satisfies the energy equality (4.11). This equality says that the rate of change of the kinetic energy of the fluid, the kinetic energy of the structure, and the elastic energy of the structure, plus the viscous energy of the structure, plus the viscous energy of the fluid, is equal to the work done by the inlet and outlet data.

Chapter 5

A kinematically coupled β-scheme for the fluid-structure interaction problem

5.1 Monolithic and partitioned algorithms for fluid-structure interaction problem

There are two main approaches to numerically solving fluid-structure interaction problems, monolithic and partitioned approach. Monolithic schemes solve the fluid-structure interaction problem as a single system, enforcing strong coupling between the fluid and structure. As a drawback, they are generally quite expensive in terms of programming time, memory requirements and computational time when solving large systems. Namely, since the coupling between the fluid and structure is highly non-linear, such solvers require solving non-linear, strongly coupled problems at each

time step using, for example, fixed point or Newtons methods [12, 23, 29, 38, 48].

Partitioned schemes separate the fluid-structure interaction problem into two main sub-problems: the fluid sub-problem and the structure sub-problem. Partitioned algorithms that do not require sub-iterations between the fluid and the structure sub-problems at each time-step are called *loosely coupled* algorithms. Those that require sub-iterations between the fluid and the structure sub-problems are called *strongly coupled* algorithms. The basic idea of a classical partitioned scheme is to solve the fluid sub-problem with Dirichlet boundary conditions at the fluid-structure interface given by the velocity of the structure from the previous time-step. After that, one can compute the fluid stress at the fluid-structure interface and use it as a load in the structure sub-problem. This saves computational time since it involves solving smaller sub-problems, and programming time by allowing the use of existing solvers for each sub-problem. However, the energy at the fluid-structure interface is not exactly balanced due to the explicit discrete coupling between sub-problems.

More precisely, if fluid and structure are of roughly the same densities, which is the case in the blood flow applications, small errors can lead to instabilities and convergence issues in numerical simulations. Numerical instabilities that occur when modeling interaction between fluid and structure of comparable densities are associated with the "added mass effect" [22]. Causin *et al.* showed that in the blood flow applications classical partitioned schemes are unconditionally unstable. The added mass effect also influences implicit schemes by causing convergence issues, but not instabilities.

One of the recently proposed loosely coupled schemes that is unconditionally stable when fluid and structure have comparable densities is *the kinematically coupled scheme*. This scheme was proposed in [46] and applied to a simple benchmark problem. To solve the fluid-structure interaction problem (4.1.1), we propose an extension of the kinematically coupled scheme with the following two goals:

1. to capture both radial and longitudinal displacement of arterial wall,

2. to improve accuracy of the scheme.

More precisely, the classical kinematically coupled scheme introduced in [46] is based on a time-splitting approach known as the Lie splitting [44]. The viscoelastic structure is split into its elastic part and the viscous part. The viscous (parabolic) part and structure inertia are treated **implicitly** together with the fluid, while the elastic (hyperbolic) part is treated separately. The inclusion of the structure inertia and viscous part of the structure into the fluid solver implicitly as a boundary condition in the weak formulation is crucial for the stability of the scheme. This approach provides a desirable discrete energy inequality making this scheme stable even when the density of the fluid is equal to the density of the structure.

The elastic part of the structure, which is solved separately, communicates with the fluid only via the kinematic coupling condition. The fluid stress does not appear in this step, as it is used as a loading to the viscous part of the structure in the weak formulation of the fluid sub-problem.

We will change this approach by additionally splitting the normal stress into a fraction that loads the viscous part of the structure, and a fraction (pressure) that

loads the elastic part of the structure. This splitting is done using a modification of the Lie splitting scheme in a way which significantly increases accuracy.

Thus, the kinematically coupled scheme, called the kinematically coupled β-scheme, is extended and improved to achieve the following two goals:

1. Capture both radial and longitudinal displacement of the linearly viscoelastic Koiter shell for the underlying fluid-structure interaction problem.

2. Increase the accuracy of the kinematically coupled scheme by introducing a new splitting strategy based on a modified Lie's scheme.

This version of the kinematically coupled scheme retains all the advantages of the original scheme, which include:

- The scheme does not require sub-iterations between the fluid and structure sub-solvers to achieve stability.

- The scheme is modular, allowing the use of one's favorite fluid or structure solvers independently. The solvers communicate through the initial conditions.

- Except for the pressure, the fluid stress at the boundary does not need to be calculated explicitly.

5.1.1 The Lie operator splitting scheme

Let A be an operator from a Hilbert space H into itself, and suppose $\phi_0 \in H$. Consider the following initial value problem

$$\frac{\partial \phi}{\partial t} + A(\phi) = 0 \quad \text{in } (0,T), \tag{5.1}$$

$$\phi(0) = \phi_0. \tag{5.2}$$

Suppose A has a non-trivial decomposition

$$A = \sum_{i=1}^{I} A_i,$$

where $I \geq 2$ and A_i are non-trivial, individually simpler operators than A. Let $\triangle t > 0$ be a time discretization step. Denote $t^n = n\triangle t$ and let ϕ^n be an approximation of $\phi(t^n)$. The **Lie scheme** [44] reads as follows: Set

$$\phi^0 = \phi_0.$$

Then, for $n \geq 0$ compute ϕ^{n+1} by solving

$$\frac{\partial \phi_i}{\partial t} + A_i(\phi_i) = 0 \quad \text{on } (t^n, t^{n+1}),$$

$$\phi_i(t^n) = \phi^{n+(i-1)/I},$$

and set $\phi^{n+i/I} = \phi_i(t^{n+1})$, for $i = 1, \ldots . I$.

This method is first-order accurate in time. More precisely, if (5.1) is defined on a finite-dimensional space, and if the operators A_i are smooth enough, then $\|\phi(t^n) - \phi^n\| = O(\Delta t)$ [44]. In our case, operator A that is associated with Problem 4.1.1 will be split into a sum of three operators:

1. The Stokes problem with suitable boundary conditions implicitly involving structure velocity and fluid stress at the boundary.

2. The fluid advection problem.

3. The elastodynamics problem for the structure, loaded by the fluid pressure.

These sub-problems are coupled via the kinematic coupling condition and via fluid pressure appearing in the elastodynamics problem. The kinematic coupling condition also plays a key role in writing Problem 4.1.1 as a first-order system, based on which the Lie splitting can be performed.

To write Problem 4.1.1 in first-order form, we utilize the kinematic coupling condition $\boldsymbol{u} = \dfrac{\partial \boldsymbol{\eta}}{\partial t}$. Written in the ALE framework, our problem now reads: Find $\mathbf{u} = (u_z, u_r)$, $\boldsymbol{\eta} = (\eta_z, \eta_r)$, with $\hat{\mathbf{u}}(\hat{\mathbf{x}}, t) = \mathbf{u}(\mathcal{A}_t(\hat{\mathbf{x}}), t)$ and $\hat{\mathbf{u}}|_{\hat{\Gamma}} = \hat{\mathbf{u}}(\hat{z}, R, t)$, such that

$$\rho_f \left(\left. \frac{\partial \mathbf{u}}{\partial t} \right|_{\hat{\boldsymbol{x}}} + (\mathbf{u} - \mathbf{w}) \cdot \nabla \mathbf{u} \right) = \nabla \cdot \boldsymbol{\sigma}, \qquad \text{in } \Omega(t) \times (0, T), \tag{5.3}$$

$$\nabla \cdot \mathbf{u} = 0 \qquad \text{in } \Omega(t) \times (0, T), \tag{5.4}$$

with the kinematic and dynamic coupling conditions holding on $\Gamma(t)$:

$$\frac{\partial \boldsymbol{\eta}}{\partial t} = \hat{\mathbf{u}}|_{\hat{\Gamma}} \qquad \text{on } (0, L) \times (0, T), \tag{5.5}$$

$$\begin{aligned} &\rho_s h \frac{\partial (\hat{u}_z|_{\hat{\Gamma}})}{\partial t} - C_2 \frac{\partial \eta_r}{\partial z} - C_3 \frac{\partial^2 \eta_z}{\partial z^2} - D_2 \frac{\partial (\hat{u}_r|_{\hat{\Gamma}})}{\partial z} - D_3 \frac{\partial^2 (\hat{u}_z|_{\hat{\Gamma}})}{\partial z^2} \\ &\quad = - \sqrt{\left(1 + \frac{\partial \eta_z}{\partial z}\right)^2 + \left(\frac{\partial \eta_r}{\partial z}\right)^2} \, \widehat{\boldsymbol{\sigma}\mathbf{n}}|_{\Gamma(t)} \cdot \mathbf{e_z} \quad \text{on } (0, L) \times (0, T), \end{aligned} \tag{5.6}$$

$$\begin{aligned} &\rho_s h \frac{\partial (\hat{u}_r|_{\hat{\Gamma}})}{\partial t} + C_0 \eta_r - C_1 \frac{\partial^2 \eta_r}{\partial z^2} + C_2 \frac{\partial \eta_z}{\partial z} + D_0 \hat{u}_r|_{\hat{\Gamma}} - D_1 \frac{\partial^2 (\hat{u}_r|_{\hat{\Gamma}})}{\partial z^2} + D_2 \frac{\partial (\hat{u}_z|_{\hat{\Gamma}})}{\partial z} \\ &= - \sqrt{\left(1 + \frac{\partial \eta_z}{\partial z}\right)^2 + \left(\frac{\partial \eta_r}{\partial z}\right)^2} \, \widehat{\boldsymbol{\sigma}\mathbf{n}}|_{\Gamma(t)} \cdot \mathbf{e_r} \quad \text{on } (0, L) \times (0, T), \end{aligned} \tag{5.7}$$

and the following boundary conditions on $\Gamma_{\text{in}} \cup \Gamma_{\text{out}} \cup \Gamma_b$:

$$\frac{\partial u_z}{\partial r}(z,0,t) = u_r(z,0,t) = 0 \quad \text{on } \Gamma_b, \tag{5.8}$$

$$\mathbf{u}(0,R,t) = \mathbf{u}(L,R,t) = 0, \quad \boldsymbol{\eta}|_{z=0,L} = \left.\frac{\partial \eta_r}{\partial z}\right|_{z=0,L} = 0, \tag{5.9}$$

$$\sigma\mathbf{n}|_{in}(0,r,t) = -p_{in}(t)\mathbf{n}|_{in}, \tag{5.10}$$

$$\sigma\mathbf{n}|_{out}(L,r,t) = -p_{out}(t)\mathbf{n}|_{out} \text{ on } (0,R)\times(0,T). \tag{5.11}$$

At time $t = 0$ the following initial conditions are prescribed:

$$\mathbf{u}|_{t=0} = \mathbf{0}, \quad \boldsymbol{\eta}|_{t=0} = \mathbf{0}, \quad \left.\frac{\partial \boldsymbol{\eta}}{\partial t}\right|_{t=0} = \mathbf{0}. \tag{5.12}$$

Notice how the kinematic coupling condition is used in (5.6) and (5.7) to rewrite the viscous part of the structure equations in terms of the trace of the fluid velocity on $\Gamma(t)$. This will be used in the splitting algorithm described below.

Remark 2. As shown in [33], if we discretise (3.11) as

$$\boldsymbol{w}(\boldsymbol{x},\tau) = \frac{\mathcal{A}_\tau(\hat{\boldsymbol{x}}) - \hat{\boldsymbol{x}}}{\tau} + O(\tau), \tag{5.13}$$

we obtain a linear affine transformation for $\mathcal{A}_\tau$

$$\mathcal{A}_\tau(\hat{\boldsymbol{x}}) = \hat{\boldsymbol{x}} + \tau\boldsymbol{w}(\boldsymbol{x},\tau) + O(\tau). \tag{5.14}$$

It can be easily shown that, using this transformation, spatial partial derivatives of a function on a domain $\Omega(\tau)$ are equal to the derivatives of the same function on the reference domain $\hat{\Omega}$, plus an error $O(\tau)$ [33]. We avoid dealing with this problem by writing only the time-derivative on the reference domain, and leaving the spatial derivatives evaluated on the current domain. Details of the new splitting are described next.

5.2 Details of the operator-splitting scheme

We split the first-order system (5.3)-(5.12) into three sub-problems. The fluid problem will be split into its viscous part and the pure advection part (incorporating the fluid and ALE advection simultaneously). The fluid stress $\widehat{\boldsymbol{\sigma}\mathbf{n}}$ will be split into two parts, Part I and Part II:

$$\widehat{\boldsymbol{\sigma}\mathbf{n}} = \underbrace{\widehat{\boldsymbol{\sigma}\mathbf{n}} + \beta\widehat{p\mathbf{n}}}_{(I)} \underbrace{-\beta\widehat{p\mathbf{n}}}_{(II)},$$

where β is a number between 0 and 1, $0 \leq \beta \leq 1$, with $\beta = 0$ corresponding to the splitting introduced in [46]. As discussed later, the accuracy of the scheme increases as the value of β increases from 0 to 1. The numerical results presented in this manuscript will correspond to the value of $\beta = 1$. The viscoelastic structure equations will be split into their viscous part and the elastic part. These are combined into a splitting algorithm in the following three steps.

- **Step 1.** Step 1 involves the Stokes problem with the viscous part of the structure and Part I of the fluid stress. The Stokes problem is solved on a fixed domain $\Omega(t^n)$ with a "Robin type" lateral boundary condition given in terms of Part I of the fluid stress which is balanced implicitly by the viscous part of the structure and by structure inertia. The problem reads as follows:

  Problem 5.2.1. *Given* $\mathbf{u}^n$ *and* $\boldsymbol{\eta}^n$*, find* $\mathbf{u}, p$ *and* $\boldsymbol{\eta}$*, with* $\hat{\mathbf{u}}(\hat{\mathbf{x}}, t) = \mathbf{u}(\mathcal{A}_t(\hat{\mathbf{x}}), t)$

such that for $t \in (t^n, t^{n+1})$*:*

$$
\begin{cases}
\rho_f \frac{\partial \mathbf{u}}{\partial t}\big|_{\hat{\boldsymbol{x}}} = \nabla \cdot \boldsymbol{\sigma}, \quad \nabla \cdot \mathbf{u} = 0 \quad \text{in } \Omega(t^n) \times (t^n, t^{n+1}) \\
\\
\frac{\partial \boldsymbol{\eta}}{\partial t}(\hat{z}, t) = 0 \quad \text{on } (0, L) \times (t^n, t^{n+1}), \\
\\
\rho_s h \frac{\partial (\hat{u}_z|_{\hat{\Gamma}})}{\partial t} - D_2 \frac{\partial (\hat{u}_r|_{\hat{\Gamma}})}{\partial z} - D_3 \frac{\partial^2 (\hat{u}_z|_{\hat{\Gamma}})}{\partial z^2} + \beta \sqrt{(1 + \frac{\partial \eta_z^n}{\partial z})^2 + (\frac{\partial \eta_r^n}{\partial z})^2} (\widehat{p^n \mathbf{n}^n}|_{\Gamma(t)}) \cdot \mathbf{e_z} \\
\qquad = -\sqrt{(1 + \frac{\partial \eta_z^n}{\partial z})^2 + (\frac{\partial \eta_r^n}{\partial z})^2} (\widehat{\boldsymbol{\sigma} \boldsymbol{n}^n}|_{\Gamma(t)}) \cdot \mathbf{e_z} \quad \text{on } (0, L) \times (t^n, t^{n+1}), \\
\\
\rho_s h \frac{\partial (\hat{u}_r|_{\hat{\Gamma}})}{\partial t} + D_0 \hat{u}_r|_{\hat{\Gamma}} - D_1 \frac{\partial^2 (\hat{u}_r|_{\hat{\Gamma}})}{\partial z^2} + D_2 \frac{\partial (\hat{u}_z|_{\hat{\Gamma}})}{\partial z} \\
\qquad + \beta \sqrt{(1 + \frac{\partial \eta_z^n}{\partial z})^2 + (\frac{\partial \eta_r^n}{\partial z})^2} (\widehat{p^n \mathbf{n}^n}|_{\Gamma(t)}) \cdot \mathbf{e_r} \\
\qquad = -\sqrt{(1 + \frac{\partial \eta_z^n}{\partial z})^2 + (\frac{\partial \eta_r^n}{\partial z})^2} (\widehat{\boldsymbol{\sigma} \boldsymbol{n}^n}|_{\Gamma(t)}) \cdot \mathbf{e_r} \quad \text{on } (0, L) \times (t^n, t^{n+1}),
\end{cases}
$$

with the following boundary conditions on $\Gamma_{\text{in}} \cup \Gamma_{\text{out}} \cup \Gamma_b$*:*

$$
\frac{\partial u_z}{\partial r}(z, 0, t) = \quad u_r(z, 0, t) = 0 \quad \text{on } \Gamma_b,
$$

$$
\mathbf{u}(0, R, t) = \mathbf{u}(L, R, t) = 0,
$$

$$
\boldsymbol{\sigma} \mathbf{n}|_{in} = -p_{in}(t) \mathbf{n}|_{in} \text{ on } \Gamma_{\text{in}}, \quad \boldsymbol{\sigma} \mathbf{n}|_{out} = -p_{out}(t) \mathbf{n}|_{out} \text{ on } \Gamma_{\text{out}},
$$

and initial conditions

$$
\mathbf{u}(t^n) = \mathbf{u}^n, \quad \boldsymbol{\eta}(t^n) = \boldsymbol{\eta}^n.
$$

Then set $\mathbf{u}^{n+1/3} = \mathbf{u}(t^{n+1})$, $\boldsymbol{\eta}^{n+1/3} = \boldsymbol{\eta}(t^{n+1})$, $p^{n+1} = p(t^{n+1})$.

Note that here we used only Part I of the fluid stress.

- **Step 2**. In Step 2 we solve the fluid and ALE advection sub-problem defined on a fixed domain $\Omega(t^n)$. The problem reads:

  Problem 5.2.2. *Find* $\mathbf{u}$ *and* $\boldsymbol{\eta}$ *with* $\hat{\mathbf{u}}(\hat{\mathbf{x}},t) = \mathbf{u}(\mathcal{A}_t(\hat{\mathbf{x}}),t)$*, such that for* $t \in (t^n, t^{n+1})$

$$\begin{cases} \frac{\partial \mathbf{u}}{\partial t}\big|_{\hat{\boldsymbol{x}}} + (\mathbf{u}^{n+1/3} - \mathbf{w}^{n+1/3}) \cdot \nabla \mathbf{u} = 0, \quad \text{in } \Omega(t^n) \times (t^n, t^{n+1}) \\ \frac{\partial \boldsymbol{\eta}}{\partial t}(\hat{z},t) = 0 \quad \text{on } (0,L) \times (t^n, t^{n+1}), \\ \rho_s h_s \frac{\partial (\hat{\mathbf{u}}|_{\hat{\Gamma}})}{\partial t} = 0, \quad \text{on } (0,L) \times (t^n, t^{n+1}), \end{cases}$$

  with boundary conditions:

$$\mathbf{u} = \mathbf{u}^{n+1/3} \quad \text{on } \Gamma_-^{n+1/3}, \text{ where}$$

$$\Gamma_-^{n+1/3} = \{\mathbf{x} \in \mathbb{R}^2 | \mathbf{x} \in \partial\Omega(t^n), (\mathbf{u}^{n+1/3} - \mathbf{w}^{n+1/3}) \cdot \mathbf{n} < 0\},$$

  and initial conditions

$$\mathbf{u}(t^n) = \mathbf{u}^{n+1/3}, \quad \boldsymbol{\eta}(t^n) = \boldsymbol{\eta}^{n+1/3}.$$

  Then set $\mathbf{u}^{n+2/3} = \mathbf{u}(t^{n+1})$, $\boldsymbol{\eta}^{n+2/3} = \boldsymbol{\eta}(t^{n+1})$.

- **Step 3**. Step 3 involves solving the elastodynamics problem for the location of the deformable boundary by solving the elastic part of the structure which is loaded by Part II of the normal fluid stress. Additionally, the fluid and structure communicate via the kinematic lateral boundary condition which gives the velocity of the structure in terms of the trace of the fluid velocity, taken initially to be the value from the previous sub-step. The problem reads:

Problem 5.2.3. *Find* $\hat{\mathbf{u}}$ *and* $\boldsymbol{\eta}$*, with* p^{n+1} *computed in Step 1 and* $\boldsymbol{\eta}^n$ *obtained at the previous time step, such that for* $t \in (t^n, t^{n+1})$

$$
\begin{cases}
\frac{\partial \mathbf{u}}{\partial t}\big|_{\hat{\boldsymbol{x}}} = 0, \quad \text{in } \Omega(t^n) \\
\\
\frac{\partial \boldsymbol{\eta}}{\partial t}(z,t) = \hat{\mathbf{u}}|_{\hat{\Gamma}} \quad \text{on } (0,L)\times(t^n,t^{n+1}), \\
\\
\rho_s h \frac{\partial(\hat{u}_z|_{\hat{\Gamma}})}{\partial t} - C_2 \frac{\partial \eta_r}{\partial z} - C_3 \frac{\partial^2 \eta_z}{\partial z^2} \\
\qquad = \beta \sqrt{(1+\frac{\partial \eta_z^n}{\partial z})^2 + (\frac{\partial \eta_r^n}{\partial z})^2}\, (\widehat{p^{n+1}\mathbf{n}^n}|_{\Gamma(t)}) \cdot \mathbf{e_z} \quad \text{on } (0,L)\times(t^n,t^{n+1}), \\
\rho_s h \frac{\partial(\hat{u}_r|_{\hat{\Gamma}})}{\partial t} + C_0 \eta_r - C_1 \frac{\partial^2 \eta_r}{\partial z^2} + C_2 \frac{\partial \eta_z}{\partial z} \\
\qquad = \beta \sqrt{(1+\frac{\partial \eta_z^n}{\partial z})^2 + (\frac{\partial \eta_r^n}{\partial z})^2}\, (\widehat{p^{n+1}\mathbf{n}^n}|_{\Gamma(t)}) \cdot \mathbf{e_r} \quad \text{on } (0,L)\times(t^n,t^{n+1}),
\end{cases}
$$

with boundary conditions:

$$\boldsymbol{\eta}|_{z=0,L} = \frac{\partial \eta_r}{\partial z}\bigg|_{z=0,L} = 0;$$

and initial conditions:

$$\mathbf{u}(t^n) = \mathbf{u}^{n+2/3}, \quad \boldsymbol{\eta}(t^n) = \boldsymbol{\eta}^{n+2/3}.$$

Then set $\mathbf{u}^{n+1} = \mathbf{u}(t^{n+1})$, $\boldsymbol{\eta}^{n+1} = \boldsymbol{\eta}(t^{n+1})$.

Do $t^n = t^{n+1}$ *and return to Step 1.*

A diagram of the scheme is shown in Figure 5.1.

Remark 5.2.1. Note that the outward normal to the lateral boundary can be written as

$$\boldsymbol{n} = \frac{(-\eta_r', 1+\eta_z')}{\sqrt{(\eta_r')^2 + (1+\eta_z')^2}}. \tag{5.15}$$

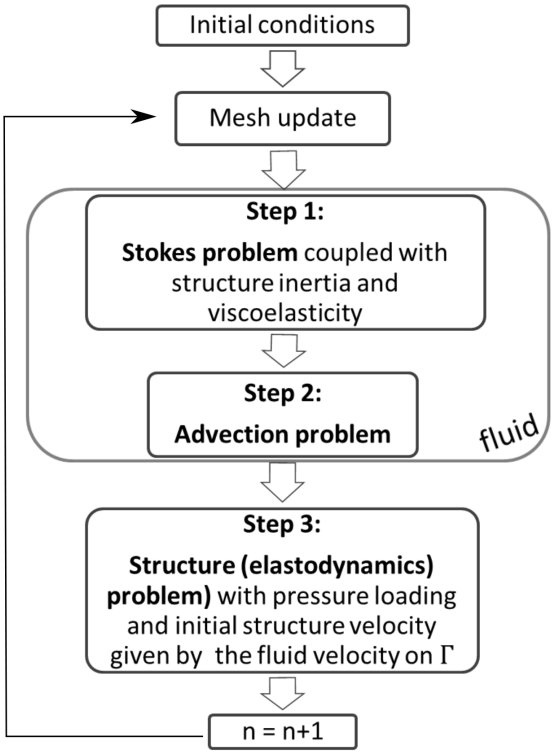

Figure 5.1: Diagram of the kinematically coupled β-scheme.

Using this equality, we can take $\boldsymbol{n}$ in Step 3 implicitly, which upon substituting $\hat{\boldsymbol{u}}|_{\hat{\Gamma}}$ by $\frac{\partial \boldsymbol{\eta}}{\partial t}$ leads to the following system

$$\begin{cases} \rho_s h \frac{\partial^2 \eta_z}{\partial t^2} - (C_2 - \beta \hat{p}|^{n+1}_{\Gamma(t)}) \frac{\partial \eta_r}{\partial z} - C_3 \frac{\partial^2 \eta_z}{\partial z^2} = 0 \quad \text{on } (0, L) \times (t^n, t^{n+1}), \\ \rho_s h \frac{\partial^2 \eta_r}{\partial t^2} + C_0 \eta_r - C_1 \frac{\partial^2 \eta_r}{\partial z^2} + (C_2 - \beta \hat{p}|^{n+1}_{\Gamma(t)}) \frac{\partial \eta_z}{\partial z} + \frac{h^2}{12} C_3 \frac{\partial^4 \eta_r}{\partial z^4} \\ \qquad = \beta \hat{p}|^{n+1}_{\Gamma(t)} \quad \text{on } (0, L) \times (t^n, t^{n+1}), \end{cases}$$

where p^{n+1} is pressure computed in Step 1.

Remark 5.2.2. The trace of the pressure, used in Step 3 to load the structure, needs to be well-defined. In general, one expects the pressure for a Dirichlet problem defined on a Lipschitz domain to be in $L^2(\Omega)$, which is not sufficient. Several works, see

e.g., [6, 56, 83], indicate that, under certain compatibility conditions, the solution of the related class of moving boundary problems has higher regularity, allowing the definition of the trace of the pressure on the moving boundary. In fact, we can show that for our problem, under certain compatibility conditions at the corners of the domain, the pressure belongs to $W^{1,8/7}(\Omega)$, which is more than sufficient for the trace to be well-defined on $\Gamma(t^n)$ [67].

5.2.1 The time-dependent Stokes problem

Consider Problem 5.2.1. In this subproblem the time derivative of $\boldsymbol{\eta}$ is zero in (t^n, t^{n+1}), implying $\boldsymbol{\eta}(t) = \boldsymbol{\eta}(t^n), \forall t \in (t^n, t^{n+1})$. Therefore we can map the problem back into $\Omega(t^n)$. Thus, in Step 1 we are solving

$$\rho_f \frac{\partial \boldsymbol{u}}{\partial t} = \nabla \cdot \boldsymbol{\sigma}, \quad \nabla \cdot \boldsymbol{u} = 0 \quad \text{in } \Omega(t^n) \times (t^n, t^{n+1}), \tag{5.16}$$

with the following boundary conditions:

- On $\Gamma(t^n)$:

$$\begin{aligned} &\rho_s h \frac{\partial (u_z|_{\Gamma(t^n)})}{\partial t} - D_2 \frac{\partial (u_r|_{\Gamma(t^n)})}{\partial z} - D_3 \frac{\partial^2 (u_z|_{\Gamma(t^n)})}{\partial z^2} \\ &+\beta \sqrt{(1 + \frac{\partial \eta_z^n}{\partial z})^2 + (\frac{\partial \eta_r^n}{\partial z})^2} (\widehat{p^n \mathbf{n}^n}|_{\Gamma(t^n)}) \cdot \mathbf{e_z} \\ &= -\sqrt{(1 + \frac{\partial \eta_z^n}{\partial z})^2 + (\frac{\partial \eta_r^n}{\partial z})^2} (\widehat{\boldsymbol{\sigma} \boldsymbol{n}^n}|_{\Gamma(t^n)}) \cdot \mathbf{e_z} \text{ on } (0, L) \times (t^n, t^{n+1}), \end{aligned} \tag{5.17}$$

$$\rho_s h\frac{\partial(u_r|_{\Gamma(t^n)})}{\partial t} + D_0 u_r|_{\Gamma(t^n)} - D_1\frac{\partial^2(u_r|_{\Gamma(t^n)})}{\partial z^2} + D_2\frac{\partial(u_z|_{\Gamma(t^n)})}{\partial z}$$
$$+\beta\sqrt{(1+\frac{\partial\eta_z^n}{\partial z})^2+(\frac{\partial\eta_r^n}{\partial z})^2}(\widehat{p^n\mathbf{n}^n}|_{\Gamma(t^n)})\cdot\mathbf{e_r}$$
$$= -\sqrt{(1+\frac{\partial\eta_z^n}{\partial z})^2+(\frac{\partial\eta_r^n}{\partial z})^2}(\widehat{\boldsymbol{\sigma}\boldsymbol{n}^n}|_{\Gamma(t^n)})\cdot\mathbf{e_r} \quad \text{on } (0,L)\times(t^n,t^{n+1}). \tag{5.18}$$

Note that $\boldsymbol{\sigma}$ here is the fluid stress at the current time.

- On Γ_b:

$$\frac{\partial u_z}{\partial r}(z,0,t)=0, \quad u_r(z,0,t)=0. \tag{5.19}$$

- On Γ_{in}:

$$\boldsymbol{u}(0,R,t)=0, \quad \boldsymbol{\sigma}\boldsymbol{n}|_{\Gamma_{in}} = -p_{in}(t)\boldsymbol{n}. \tag{5.20}$$

- On Γ_{out}:

$$\boldsymbol{u}(L,R,t)=0, \quad \boldsymbol{\sigma}\boldsymbol{n}|_{\Gamma_{out}} = -p_{out}(t)\boldsymbol{n}. \tag{5.21}$$

Initially,

$$\boldsymbol{u}(t^n)=\boldsymbol{u}^n, \quad \boldsymbol{\eta}(t^n)=\boldsymbol{\eta}^n. \tag{5.22}$$

5.2.1.1 Variational formulation

Recall the spaces of test functions defined in (4.6) and (4.7)

$$\begin{aligned} V(t) &= \{\boldsymbol{v}:\Omega(t)\to\mathbb{R}^2|\ \boldsymbol{v}=\hat{\boldsymbol{v}}\circ(\mathcal{A}_t)^{-1}, \hat{\boldsymbol{v}}\in(H^1(\hat{\Omega}))^2, v_r|_{r=0}=0,\\ &\qquad \boldsymbol{v}|_{\Gamma(t)}\in H_0^1(\Gamma(t))\},\\ Q(t) &= \{q:\Omega(t)\to\mathbb{R}|\ q=\hat{q}\circ(\mathcal{A}_t)^{-1}, \hat{q}\in L^2(\hat{\Omega})\}, \ \text{ for all } t\in[0,T). \end{aligned}$$

Then the variational formulation of problem (5.16)-(5.22) reads as follows: *For* $t \in (0,T)$ *find* $\boldsymbol{u} \in V(t^n)$ *and* $p \in Q(t^n)$ *such that* $\forall \boldsymbol{v} \in V(t^n)$

$$\begin{aligned}
&\varrho_f \int_{\Omega(t^n)} \frac{\partial \boldsymbol{u}}{\partial t} \cdot \boldsymbol{v} d\boldsymbol{x} + 2\mu \int_{\Omega(t^n)} \boldsymbol{D}(\boldsymbol{u}) : \boldsymbol{D}(\boldsymbol{v}) d\boldsymbol{x} + \int_0^L \rho_s h \frac{\partial (u_z|_{\Gamma(t^n)})}{\partial t} v_z|_{\Gamma(t^n)} dz \\
&\qquad - \int_0^L D_2 \frac{\partial (u_r|_{\Gamma(t^n)})}{\partial z} v_z|_{\Gamma(t^n)} dz + \int_0^L D_3 \frac{\partial (u_z|_{\Gamma(t^n)})}{\partial z} \frac{\partial (v_z|_{\Gamma(t^n)})}{\partial z} dz \\
&\quad + \int_0^L \rho_s h \frac{\partial (u_r|_{\Gamma(t^n)})}{\partial t} v_r|_{\Gamma(t^n)} dz + \int_0^L \left(D_0 u_r|_{\Gamma(t^n)} + D_2 \frac{\partial (u_z|_{\Gamma(t^n)})}{\partial z} \right) v_r|_{\Gamma(t^n)} dz \\
&\quad + \int_0^L D_1 \frac{\partial (u_r|_{\Gamma(t^n)})}{\partial z} \frac{\partial (v_r|_{\Gamma(t^n)})}{\partial z} dz - \int_{\Omega(t^n)} p \nabla \cdot \boldsymbol{v} d\boldsymbol{x} = \int_0^R p_{in}(t^n) v_z|_{z=0} dr \\
&\quad - \int_0^R p_{out}(t^n) v_z|_{z=L} dr - \beta \int_0^L \sqrt{(1 + \frac{\partial \eta_z^n}{\partial z})^2 + (\frac{\partial \eta_r^n}{\partial z})^2} \widehat{(p^n n_z^n)}|_{\Gamma(t^n)} v_z|_{\Gamma(t^n)} dz \\
&\qquad - \beta \int_0^L \sqrt{(1 + \frac{\partial \eta_z^n}{\partial z})^2 + (\frac{\partial \eta_r^n}{\partial z})^2} \widehat{(p^n n_r^n)}|_{\Gamma(t^n)} v_r|_{\Gamma(t^n)} dz,
\end{aligned}$$

and

$$\int_{\Omega(t^n)} q \nabla \cdot \boldsymbol{u} d\boldsymbol{x} = 0, \quad \forall q \in Q(t^n). \tag{5.23}$$

To discretise problem (5.16)-(5.22) in space we use an isoparametric version of the Bercovier-Pironneau finite element spaces introduced in [13], also known as $\mathbb{P}_1$-*iso*-$\mathbb{P}_2$ and $\mathbb{P}_1$ approximation. Namely, we use a continuous piecewise linear approximation of the pressure on a triangulation $\hat{\mathcal{T}}_h$ of $\hat{\Omega}$, and the same approximation for velocity on a mesh $\hat{\mathcal{T}}_{h/2}$, where $\hat{\mathcal{T}}_{h/2}$ is twice finer than $\hat{\mathcal{T}}_h$.

Precisely, denote by $\hat{\mathcal{T}}_h = \hat{\mathcal{T}}_{Rh} \cup \hat{\mathcal{T}}_{Ch}$, where

$$\begin{aligned}
\hat{\mathcal{T}}_{Rh} &= \{T |\ T \in \hat{\mathcal{T}}_h,\ \text{the three edges of } T \text{ are rectilinear}\}, \\
\hat{\mathcal{T}}_{Ch} &= \{T |\ T \in \hat{\mathcal{T}}_h,\ T \text{ has two vertices on } \Gamma\}.
\end{aligned}$$

To form the mesh $\hat{\mathcal{T}}_{h/2}$, every triangle $T \in \hat{\mathcal{T}}_{Rh}$ is divided into four sub-triangles by joining the midpoints of its edges. Every curved triangle $T \in \hat{\mathcal{T}}_{Ch}$ is divided into four sub-triangles by joining the two midpoints of the rectilinear edges, and the midpoint of the arc, as shown in Figure 5.2.

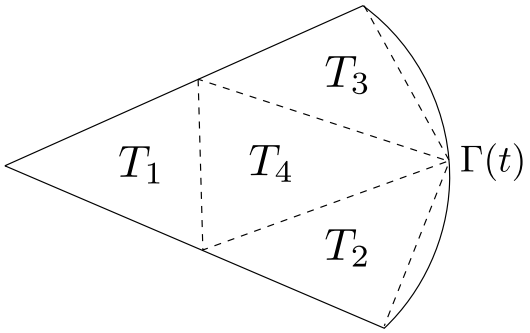

Figure 5.2: Approximation of a curved triangle T by $\tilde{T} = \cup_{i=1}^{4} T_i$.

Pressure and velocity spaces on a reference domain are now approximated, respectively, by

$$\begin{aligned} \hat{Q}_h &= \{q|\ q \in C^0(\bar{\hat{\Omega}}),\ q|_T \in \mathbb{P}_1, \forall T \in \hat{\mathcal{T}}_{Rh}, \\ &\qquad q|_{\tilde{T}} \in \tilde{P}_1(\tilde{T}), \forall \tilde{T} \in \hat{\mathcal{T}}_{Ch}\}, \end{aligned} \tag{5.24}$$

$$\begin{aligned} \hat{V}_h &= \{\boldsymbol{v}|\ \boldsymbol{v} \in (C^0(\bar{\hat{\Omega}}))^2,\ \boldsymbol{v}|_T \in (\tilde{P}_2(T))^2, \forall T \in \hat{\mathcal{T}}_{Rh}, \\ &\qquad \boldsymbol{v}|_{\tilde{T}} \in (\tilde{P}_2(\tilde{T}))^2, \forall \tilde{T} \in \hat{\mathcal{T}}_{Ch}\}, \end{aligned} \tag{5.25}$$

where

$$\begin{aligned} \tilde{P}_2(T) &= \{\varphi|\ \varphi \in C^0(T),\ \varphi|_{T_i} \in \mathbb{P}_1,\ \forall i = 1, \ldots, 4\}, \quad \forall T \in \hat{\mathcal{T}}_h, \\ \tilde{P}_1(\tilde{T}) &= \{\varphi|\ \varphi \in \tilde{P}_2(\tilde{T}), \varphi \text{ at the midpoint is equal to the arithmetic average of } \varphi \\ &\qquad \text{at corresponding endpoints}\}. \end{aligned}$$

With a slight abuse of notation, using the ALE mapping (3.7), we can define the finite element spaces for a given time step t^n

$$Q_h(t^n) = \mathcal{A}_{t^n}(\hat{Q}_h), \tag{5.26}$$

$$V_h(t^n) = \mathcal{A}_{t^n}(\hat{V}_h), \tag{5.27}$$

where

$$\mathcal{T}_h = \mathcal{A}_{t^n}(\hat{\mathcal{T}}_h), \tag{5.28}$$

and $\Gamma(t^n)$ is linearly interpolated and each triangle with straight edges in $\hat{\mathcal{T}}_h$ is transformed in a triangle with straight edges in $\mathcal{T}_h$.

To discretise the time-derivative we use the backward Euler method. To write the variational formulation of a fully discrete problem let $Q_h(t^n)$ and $V_h(t^n)$ be defined as in (5.26)-(5.27). Then, the variational formulation of a problem discretised in time and space is given by: *Find* $\boldsymbol{u}_h^{n+1/3} \in V_h(t^n)$ *and* $p_h^{n+1/3} \in Q_h(t^t)$ *such that* $\forall \boldsymbol{v}_h \in V_h(t^n)$

$$\begin{aligned}
&\frac{\rho_f}{\triangle t}\int_{\Omega(t^n)} \boldsymbol{u}_h^{n+1/3}\cdot\boldsymbol{v}_h d\boldsymbol{x} + 2\mu\int_{\Omega(t^n)} \boldsymbol{D}(\boldsymbol{u}_h^{n+1/3}):\boldsymbol{D}(\boldsymbol{v}_h)d\boldsymbol{x}\\
&+\frac{\varrho_s h}{\triangle t}\int_0^L u_{h,z}^{n+1/3}|_{\Gamma(t^n)} v_{h,z}|_{\Gamma(t^n)} dz + \frac{\rho_s h}{\triangle t}\int_0^L u_{h,r}^{n+1/3}|_{\Gamma(t^n)} v_{h,r}|_{\Gamma(t^n)} dz\\
&+\int_0^L D_3 \frac{\partial(u_{h,z}^{n+1/3}|_{\Gamma(t^n)})}{\partial z}\frac{\partial(v_{h,z}|_{\Gamma(t^n)})}{\partial z}dz - \int_0^L D_2\frac{\partial(u_{h,r}^{n+1/3}|_{\Gamma(t^n)})}{\partial z} v_{h,z}|_{\Gamma(t^n)} dz\\
&+\int_0^L \left(D_0 u_{h,r}^{n+1/3}|_{\Gamma(t^n)} + D_2\frac{\partial(u_{h,z}^{n+1/3}|_{\Gamma(t^n)})}{\partial z}\right) v_{h,r}|_{\Gamma(t^n)} dz\\
&+\int_0^L D_1\frac{\partial(u_{h,r}^{n+1/3}|_{\Gamma(t^n)})}{\partial z}\frac{\partial(v_{h,r}|_{\Gamma(t^n)})}{\partial z}dz - \int_{\Omega(t^n)} p_h^{n+1/3}\nabla\cdot\boldsymbol{v}_h d\boldsymbol{x} = L(\boldsymbol{v}_h),
\end{aligned} \tag{5.29}$$

and

$$\int_{\Omega(t^n)} q_h \nabla \cdot \boldsymbol{u}_h^{n+1/3} d\boldsymbol{x} = 0, \quad \forall q_h \in Q_h(t^n), \tag{5.30}$$

where

$$\begin{aligned} L(\boldsymbol{v}_h) = \frac{\rho_f}{\triangle t} \int_{\Omega(t^n)} \boldsymbol{u}_h^n \cdot \boldsymbol{v}_h d\boldsymbol{x} + \frac{\rho_s h}{\triangle t} \int_0^L u_{h,r}^n|_{\Gamma(t^n)} v_{h,r}|_{\Gamma(t^n)} dz + \frac{\rho_s h}{\triangle t} \int_0^L u_{h,r}^n|_{\Gamma(t^n)} v_{h,r}|_{\Gamma(t^n)} dz \\ + \int_0^R p_{in}(t^n) v_{h,z}|_{z=0} dr - \int_0^R p_{out}(t^n) v_{h,z}|_{z=L} dr \\ -\beta \int_0^L \sqrt{(1 + \frac{\partial \eta_{h,z}^n}{\partial z})^2 + (\frac{\partial \eta_{h,r}^n}{\partial z})^2} (\widehat{p_h^n n_z^n})|_{\Gamma(t^n)} v_{h,z}|_{\Gamma(t^n)} dz \\ -\beta \int_0^L \sqrt{(1 + \frac{\partial \eta_{h,z}^n}{\partial z})^2 + (\frac{\partial \eta_{h,r}^n}{\partial z})^2} (\widehat{p_h^n n_r^n})|_{\Gamma(t^n)} v_{h,r}|_{\Gamma(t^n)} dz. \end{aligned} \tag{5.31}$$

5.2.1.2 An iterative procedure for solving the generalized Stokes problem

To describe a basic idea of an iterative method for solving the Stokes problem, we start by considering the generalized Stokes problem:

$$\begin{cases} \alpha \boldsymbol{u} - \mu \triangle \boldsymbol{u} + \nabla p = \boldsymbol{f} & \text{in } \Omega(t^n), \\ \nabla \cdot \boldsymbol{u} = 0 & \text{in } \Omega(t^n), \\ \boldsymbol{u} = \boldsymbol{g}_0 \quad \text{on } \Gamma_0, \quad \mu \frac{\partial \boldsymbol{u}}{\partial n} - \boldsymbol{n} p = g_1 \quad \text{on } \Gamma_1, \end{cases} \tag{5.32}$$

where $\Gamma_0 \cap \Gamma_1 = \emptyset$, $\overline{\Gamma_0 \cup \Gamma_1} = \partial\Omega(t^n)$. Note that this corresponds to the discretized problem (5.16) for a fixed time $t = t^n$ and generalized boundary conditions. To write the weak formulation of problem (5.32), introduce the following function spaces:

$$V_0 = \{\boldsymbol{v} | \boldsymbol{v} \in (H^1(\Omega(t^n)))^2, \ \boldsymbol{v} = \boldsymbol{0} \text{ on } \Gamma_0\}, \tag{5.33}$$

$$V_{g0} = \{\boldsymbol{v} | \boldsymbol{v} \in (H^1(\Omega(t^n)))^2, \ \boldsymbol{v} = \boldsymbol{g}_0 \text{ on } \Gamma_0\}. \tag{5.34}$$

Now the weak form of problem (5.32) is given by:

find $\boldsymbol{u} \in V_{g0},\ p \in L^2(\Omega(t^n))$ *such that*

$$\begin{cases} \int_{\Omega(t^n)}(\alpha \boldsymbol{u}\cdot\boldsymbol{v} + \mu\nabla\boldsymbol{u} : \nabla\boldsymbol{v})d\boldsymbol{x} - \int_{\Omega(t^n)} p\nabla\cdot\boldsymbol{v}d\boldsymbol{x} \\ \qquad = \int_{\Omega(t^n)} \boldsymbol{f}\cdot\boldsymbol{v}d\boldsymbol{x} + \int_{\Gamma_1}\boldsymbol{g}_1\cdot\boldsymbol{v}d\Gamma \qquad \forall \boldsymbol{v}\in V_0, \\ \nabla\cdot\boldsymbol{u} = 0 \qquad \text{in } \Omega(t^n). \end{cases} \tag{5.35}$$

Next, we introduce a linear operator from $L^2(\Omega(t^n))$ into $L^2(\Omega(t^n))$, called *Stokes operator*, defined by

$$Aq = \nabla\cdot\boldsymbol{u}_q \quad \forall q \in L^2(\Omega(t^n)), \tag{5.36}$$

where $\boldsymbol{u}_q \in V_0$ is a unique solution of the following linear variational problem

$$\int_{\Omega(t^n)}(\alpha\boldsymbol{u}_q\cdot\boldsymbol{v} + \mu\nabla\boldsymbol{u} : \nabla\boldsymbol{v})d\boldsymbol{x} = \int_{\Omega(t^n)} q\nabla\cdot\boldsymbol{v}d\boldsymbol{x} \quad \forall\boldsymbol{v}\in V_0. \tag{5.37}$$

In the following Lemma, we summarize a result from [44], Section 4.19.4:

Lemma 5.2.1. *Assume that problem* (5.35) *has s solution* $\{\boldsymbol{u}, p\}$ *in* $V_{g0}\times P$. *Then the pressure p also verifies*

$$Ap = -\nabla\cdot\boldsymbol{u}_0, \tag{5.38}$$

where $\boldsymbol{u}_0 \in V_{g0}$ *is the solution of the following problem,* $\forall\boldsymbol{v}\in V_0$*:*

$$\int_{\Omega(t^n)}(\alpha\boldsymbol{u}_0\cdot\boldsymbol{v} + \mu\nabla\boldsymbol{u}_0 : \nabla\boldsymbol{v})d\boldsymbol{x} = \int_{\Omega(t^n)}\boldsymbol{f}\cdot\boldsymbol{v}d\boldsymbol{x} + \int_{\Gamma_1}\boldsymbol{g}_1\cdot\boldsymbol{v}d\Gamma. \tag{5.39}$$

To write an iterative method for the generalized Stokes problem, let us observe that the incompressibility condition $\nabla\cdot\boldsymbol{u} = 0$ is equivalent to

$$p = p - \rho\nabla\cdot\boldsymbol{u}, \tag{5.40}$$

if $\rho \neq 0$. Using the latter identity, an iterative method for the generalized Stokes problem proposed in [44], Section 4.20., reads as follows:

Let $p^0 \in L^2(\Omega(t^n))$ be given. Then, for $n \geq 0$, $p^k \in L^2(\Omega(t^n))$ known, we obtain $\boldsymbol{u}^k$ and p^{k+1} via

$$\begin{cases} \int_{\Omega(t^n)} (\alpha \boldsymbol{u}^k \cdot \boldsymbol{v} + \mu \nabla \boldsymbol{u}^k : \nabla \boldsymbol{v}) d\boldsymbol{x} - \int_{\Omega(t^n)} p^k \nabla \cdot \boldsymbol{v} d\boldsymbol{x} \\ \qquad = \int_{\Omega(t^n)} \boldsymbol{f} \cdot \boldsymbol{v} d\boldsymbol{x} + \int_{\Gamma_1} \boldsymbol{g}_1 \cdot \boldsymbol{v} d\Gamma \qquad \forall \boldsymbol{v} \in V_0, \end{cases} \tag{5.41}$$

$$p^{k+1} = p^k - \rho \nabla \cdot \boldsymbol{u}^k. \tag{5.42}$$

It was shown in [44], Section 4.20.1., that if $0 < \rho < \mu$, the iterative scheme above converges to the unique solution $\{\boldsymbol{u}, p\}$ of the generalized Stokes problem (5.35) in $V_{g0} \times L^2(\Omega(t^n))$.

Using the iterative scheme (5.41)-(5.42) and Lemma 5.2.1, we give a naive description of the conjugate gradient method applied to the sequence $\{p^k\}_{k \geq 0}$:

Take an initial guess $p^0 \in L^2(\Omega(t^n))$ and then find $g^0 \in L^2(\Omega(t^n))$ such that

$$\int_{\Omega(t^n)} g^0 q d\boldsymbol{x} = \int_{\Omega(t^n)} (Ap^0 + \nabla \cdot \boldsymbol{u}_0) q d\boldsymbol{x}, \quad \forall \boldsymbol{q} \in L^2(\Omega(t^n)),$$

where $\boldsymbol{u}_0$ is the solution of (5.39). Set $w^0 = g^0$.

For $k \geq 0$, assuming that p^k, r^k, g^k and w^k are known, compute $p^{k+1}, r^{k+1}, g^{k+1}$ and w^{k+1} as follows:

1. $\rho^k = \dfrac{\int_{\Omega(t^n)} |g^k|^2 d\boldsymbol{x}}{\int_{\Omega(t^n)} (Aw^k) w^k d\boldsymbol{x}}$,
2. $p^{k+1} = p^k - \rho^k w^k$,
3. *find $g^{k+1} \in L^2(\Omega(t^n))$ such that*

$$\int_{\Omega(t^n)} g^{k+1} q d\boldsymbol{x} = \int_{\Omega(t^n)} g^k q d\boldsymbol{x} - \rho^k \int_{\Omega(t^n)} Aw^k q d\boldsymbol{x}, \quad \forall \boldsymbol{q} \in L^2(\Omega(t^n)). \tag{5.43}$$

If $\dfrac{\int_{\Omega(t^n)} |g^{k+1}|^2 d\boldsymbol{x}}{\int_{\Omega(t^n)} |g^k|^2 d\boldsymbol{x}} \leq \epsilon$ *take* $p = p^{k+1}$. *Else compute*

4. $\gamma_k = \dfrac{\int_{\Omega(t^n)} |g^{k+1}|^2 d\boldsymbol{x}}{\int_{\Omega(t^n)} |g^k|^2 d\boldsymbol{x}}$,
5. $w^{k+1} = g^{k+1} + \gamma_k w^k$.

   Set $k+1 \to k$ *and go back to Step 1.*

Since we do not know operator A explicitly, but only how A operates on particular vectors, we can rewrite the latter algorithm in the following way:

Take an initial guess $p^0 \in L^2(\Omega(t^n))$ *and then find* $\boldsymbol{u}^0 \in V_{g0}$ *such that*

$$\alpha \boldsymbol{u}^0 - \mu \triangle \boldsymbol{u}^0 = f - \nabla p^0 \quad \text{in } \Omega(t^n)$$
$$\boldsymbol{u}^0 = \boldsymbol{g}_0 \quad \text{on } \Gamma_0.$$

Set $g^0 = \nabla \cdot \boldsymbol{u}^0$ and $w^0 = g^0$.

For $k \geq 0$, *assuming that* p^k, r^k, g^k *and* w^k *are known, compute* $p^{k+1}, r^{k+1}, g^{k+1}$ *and* w^{k+1} *as follows:*

1. *find* $\boldsymbol{u}^k \in V_{g0}$ *such that*

$$\alpha \boldsymbol{u}^k - \mu \triangle \boldsymbol{u}^k = f - \nabla p^k \quad \text{in } \Omega(t^n)$$
$$\boldsymbol{u}^k = 0 \quad \text{on } \Gamma_0,$$

2. $\bar{g}^k = \nabla \cdot \boldsymbol{u}^k$,
3. $\rho^k = \dfrac{\int_{\Omega(t^n)} |g^k|^2 d\boldsymbol{x}}{\int_{\Omega(t^n)} \bar{g}^k w^k d\boldsymbol{x}}$,
4. $p^{k+1} = p^k - \rho^k w^k$,

5. $g^{k+1} = g^k - \rho^k \bar{g}^k$.
   If $\dfrac{\int_{\Omega(t^n)} |g^{k+1}|^2 d\boldsymbol{x}}{\int_{\Omega(t^n)} |g^k|^2 d\boldsymbol{x}} \leq \epsilon$ *take* $p = p^{k+1}$. *Else compute*

6. $\gamma_k = \dfrac{\int_{\Omega(t^n)} |g^{k+1}|^2 d\boldsymbol{x}}{\int_{\Omega(t^n)} |g^k|^2 d\boldsymbol{x}}$,

7. $w^{k+1} = g^{k+1} + \gamma_k w^k$.

   Set $k+1 \to k$ *and go back to Step 1.*

With this we finish a description of the conjugate gradient method for a generalized Stokes problem. Since it is known that the rate of convergence of the conjugate gradient method that uses the classical scalar product in $L^2(\Omega(t^n))$ is slow if $\alpha >> \mu$, which is the case in blood flow, in the next section we present the preconditioned conjugate gradient method for the Stokes problem (5.16)-(5.22).

5.2.1.3 The preconditioned conjugate gradient method for the Stokes problem

To solve the problem (5.16)-(5.22) numerically, we use a preconditioned conjugate gradient method proposed in [45]. The fully discrete variational formulation of the problem is given by (5.29)- (5.31). To avoid cumbersome notation we will drop the h subscript for the discretized variables.

Denote by $\alpha = \varrho_f / \triangle t$ and $\beta = \varrho_s h / \triangle t + D_0$ and consider the following scalar product in $L^2(\Omega(t^n))$

$$\{p, q\} \to \int_{\Omega(t^n)} (B^{-1} p) q d\boldsymbol{x},$$

where $Bq = \alpha\varphi_q + \mu q$, and φ_q is a solution of the following problem

$$\begin{cases} -\triangle\varphi_q = q & \text{in } \Omega(t^n), \\ \varphi_q = 0 & \text{on}\Gamma_{in} \cup \Gamma_{out}, \\ \frac{\partial\varphi_q}{\partial n} = 0 & \text{on } \Gamma_b, \\ \varphi_q + \frac{\beta}{\alpha}\frac{\partial\varphi_q}{\partial n} = 0 & \text{on } \Gamma(t^n). \end{cases} \tag{5.44}$$

Then, the preconditioned conjugate gradient algorithm for the problem (5.29)- (5.31) read as follows:

Take an initial guess $p^0 \in Q_h(t^n)$ *and then find* $\boldsymbol{u}^0 \in V_h(t^n)$ *such that*

$$\begin{aligned} &\frac{\varrho_f}{\triangle t}\int_{\Omega(t^n)} \boldsymbol{u}^0\cdot\boldsymbol{v}d\boldsymbol{x} + 2\mu\int_{\Omega(t^n)} \boldsymbol{D}(\boldsymbol{u}^0):\boldsymbol{D}(\boldsymbol{v})d\boldsymbol{x} + \frac{\varrho_s h}{\triangle t}\int_0^L u_z^0|_{\Gamma(t^n)}v_z|_{\Gamma(t^n)}dz \\ &\quad -\int_0^L D_2\frac{\partial(u_r^0|_{\Gamma(t^n)})}{\partial z}v_z|_{\Gamma(t^n)}dz + \int_0^L D_3\frac{\partial(u_z^0|_{\Gamma(t^n)})}{\partial z}\frac{\partial(v_z|_{\Gamma(t^n)})}{\partial z}dz \\ &\quad +\frac{\varrho_s h}{\triangle t}\int_0^L u_r^0|_{\Gamma(t^n)}v_r|_{\Gamma(t^n)}dz + \int_0^L\left(D_0u_r^0|_{\Gamma(t^n)} + D_2\frac{\partial(u_z^0|_{\Gamma(t^n)})}{\partial z}\right)v_r|_{\Gamma(t^n)}dz \\ &+\int_0^L D_1\frac{\partial(u_r^0|_{\Gamma(t^n)})}{\partial z}\frac{\partial(v_r|_{\Gamma(t^n)})}{\partial z}dz = \int_{\Omega(t^n)} p^0\nabla\cdot\boldsymbol{v}d\boldsymbol{x} + L(\boldsymbol{v}), \quad \forall\boldsymbol{v}\in V_h(t^n), \end{aligned} \tag{5.45}$$

and set $r^0 = \nabla\cdot\boldsymbol{u}^0$.

Then, solve

$$\begin{cases} -\triangle\varphi^0 = r^0 & \text{in } \Omega(t^n), \\ \varphi^0 = 0 & \text{on}\Gamma_{in} \cup \Gamma_{out}, \\ \frac{\partial\varphi^0}{\partial n} = 0 & \text{on } \Gamma_b, \\ \varphi^0 + \frac{\beta}{\alpha}\frac{\partial\varphi^0}{\partial n} = 0 & \text{on } \Gamma(t^n), \end{cases} \tag{5.46}$$

and set

$$g^0 = \mu r^0 + \alpha\varphi^0 \tag{5.47}$$

$$w^0 = g^0. \tag{5.48}$$

For $k \geq 0$, assuming that p^k, r^k, g^k and w^k are known, compute $p^{k+1}, r^{k+1}, g^{k+1}$ and w^{k+1} as follows:

Find $\bar{\boldsymbol{u}}^k \in V_h(t^n)$ such that

$$\begin{aligned}
&\frac{\varrho_f}{\triangle t}\int_{\Omega(t^n)} \bar{\boldsymbol{u}}^k \cdot \boldsymbol{v} d\boldsymbol{x} + 2\mu \int_{\Omega(t^n)} \boldsymbol{D}(\bar{\boldsymbol{u}}^k) : \boldsymbol{D}(\boldsymbol{v}) d\boldsymbol{x} + \frac{\varrho_s h}{\triangle t}\int_0^L \bar{u}_z^k|_{\Gamma(t^n)} v_z|_{\Gamma(t^n)} dz \\
&\quad - \int_0^L D_2 \frac{\partial(\bar{u}_r^k|_{\Gamma(t^n)})}{\partial z} v_z|_{\Gamma(t^n)} dz + \int_0^L D_3 \frac{\partial(\bar{u}_z^k|_{\Gamma(t^n)})}{\partial z}\frac{\partial(v_z|_{\Gamma(t^n)})}{\partial z} dz \\
&+ \frac{\varrho_s h}{\triangle t}\int_0^L \bar{u}_r^k|_{\Gamma(t^n)} v_r|_{\Gamma(t^n)} dz + \int_0^L \left(D_0 \bar{u}_r^k|_{\Gamma(t^n)} + D_2 \frac{\partial(\bar{u}_z^k|_{\Gamma(t^n)})}{\partial z}\right) v_r|_{\Gamma(t^n)} dz \\
&+ \int_0^L D_1 \frac{\partial(\bar{u}_r^k|_{\Gamma(t^n)})}{\partial z}\frac{\partial(v_r|_{\Gamma(t^n)})}{\partial z} dz = \int_{\Omega(t^n)} w^k \nabla \cdot \boldsymbol{v} d\boldsymbol{x}, \quad \forall \boldsymbol{v} \in V_h(t^n),
\end{aligned} \tag{5.49}$$

and set $\bar{r}^k = \nabla \cdot \bar{\boldsymbol{u}}^k$. Compute

$$\varrho_k = \int_{\Omega(t^n)} r^k g^k d\boldsymbol{x} / \int_{\Omega(t^n)} \bar{r}^k w^k d\boldsymbol{x}, \tag{5.50}$$

and set

$$p^{k+1} = p^k - \varrho_k w^k \tag{5.51}$$

$$r^{k+1} = r^k - \varrho_k \bar{r}^k. \tag{5.52}$$

Then, solve

$$\begin{cases}
-\triangle \bar{\varphi}^k = \bar{r}^k & \text{in } \Omega(t^n), \\
\bar{\varphi}^k = 0 & \text{on} \Gamma_{in} \cup \Gamma_{out}, \\
\frac{\partial \bar{\varphi}^k}{\partial n} = 0 & \text{on } \Gamma_b, \\
\bar{\varphi}^k + \frac{\beta}{\alpha}\frac{\partial \bar{\varphi}^k}{\partial n} = 0 & \text{on } \Gamma(t^n),
\end{cases} \tag{5.53}$$

and set $g^{k+1} = g^k - \varrho_k(\mu \bar{r}^k + \alpha \bar{\varphi}^k)$.

If

$$\int_{\Omega(t^n)} r^{k+1} g^{k+1} d\boldsymbol{x} / \int_{\Omega(t^n)} r^0 g^0 \leq \epsilon \tag{5.54}$$

take $p = p^{k+1}$; *else, compute*

$$\gamma_k = \int_{\Omega(t^n)} r^{k+1} g^{k+1} d\boldsymbol{x} / \int_{\Omega(t^n)} r^k g^k d\boldsymbol{x}, \tag{5.55}$$

and set

$$w^{k+1} = g^{k+1} + \gamma_k w^k. \tag{5.56}$$

Do $k = k + 1$ *and return to* (5.49).

This algorithm is a pressure-driven method, where the vectors g^k and w^k are pressure corrections which enforce the incompressibility condition. A great attention was given in the choice of a proper preconditioner in the pressure space. More precisely, the choice of a new scalar product associated with the boundary conditions reduces substantially the number of iterations when compared with a conjugate gradient algorithm equipped with the canonical scalar product in L^2.

Remark 5.2.3. The algorithm above requires the solution of the elliptic problem (5.53) at each iteration of the conjugate gradient calculation. This elliptic problem is defined on the domain $\Omega(t^n)$ which changes at each time step and therefore the stiffness matrix of the elliptic problem should be recalculated at each time step. In order to avoid this, even if the geometry of the domain has changed, we assemble the stiffness matrix on the initial domain and we "freeze" it, using the same matrix at every time step. By doing this, we need to assemble the stiffness matrix only once and this still gives excellent numerical results.

5.2.2 The fluid and ALE advection

Problem 5.2.2 consists of two non-dissipative transport problems, the transport of u_z and the transport of u_r. In this sub-problem the time derivative of $\boldsymbol{\eta}$ is zero, which again allows us to map the reference domain onto the current domain. In an attempt to preserve non-dissipative nature of the problem, it is natural to use solvers with low numerical dissipation. We have implemented two such solvers: a positivity-preserving ALE finite element method [15] (Solver 1), and a wave-like equation method [44] (Solver 2). We can use Solver 1 or Solver 2, depending on the particular application in mind. For example, a positivity preserving ALE finite element method is particularly suitable for problems for which it is important to preserve positivity of the unknown variable, such as, for example, a concentration of a given quantity. We start by a description of Solver 1 first, and present the wave-like method (Solver 2) next.

5.2.2.1 A positivity-preserving ALE finite element scheme

In this section we present the numerical algorithm proposed in [15], which is capable of successfully keeping positivity of concentration, preserving conservation of mass at the discrete level, correctly resolving the no-flux condition at the moving boundary, and resolving the sharp and thin concentration fronts in the advection-dominated case.

Denote by c the advected quantity and consider the following advection problem

$$\frac{\partial c}{\partial t} + \nabla \cdot (\boldsymbol{u} c) = 0 \quad \text{in } \Omega(t),\ t \in (0, T), \tag{5.57}$$

in the time-dependent domain (see Figure 3.1)

$$\Omega(t) = \{(z, r) \in \mathbb{R}^2 : 0 < z < L, 0 < r < g(z; t)\},$$

where

$$g(\cdot; t) : (0, L) \to \mathbb{R}, \quad g(\cdot; t) : z \mapsto g(z; t), \quad \forall t \in (0, T)$$

is a Lipschitz continuous function describing the motion of the upper wall. We assume the following:

- $\nabla \cdot \boldsymbol{u} = 0$ in $\Omega(t)$,
- $\boldsymbol{u} \cdot \boldsymbol{n}|_{\Gamma(t)} = \dfrac{\partial \boldsymbol{\eta}}{\partial t}$.

Using an ALE formulation, we can write (5.57) in conservative form as

$$\frac{1}{J_{\mathcal{A}}} \frac{\partial (J_{\mathcal{A}} c)}{\partial t}\bigg|_{\hat{x}} + \nabla \cdot ((\boldsymbol{u} - \boldsymbol{w})c) = 0 \quad \text{in } \Omega(t),\ t \in (0, T), \tag{5.58}$$

where $J_{\mathcal{A}}$ is the Jacobian of the ALE mapping $\mathcal{A}_t$ defined in (3.15), and $\boldsymbol{w}$ is the domain velocity. We assume

$$\boldsymbol{u} \cdot \boldsymbol{n} = \boldsymbol{w} \cdot \boldsymbol{n} \quad \text{on } \Gamma_b \cup \Gamma(t),\ t \in (0, T), \tag{5.59}$$

where Γ_b denotes the bottom boundary.

Denote by

$$\Gamma_- = \{\boldsymbol{x} \in \mathbb{R}^2 | \boldsymbol{x} \in \partial\Gamma_{in}, (\boldsymbol{u} - \boldsymbol{w}) \cdot \boldsymbol{n} < 0\}, \tag{5.60}$$

$$\Gamma_+ = \{\boldsymbol{x} \in \mathbb{R}^2 | \boldsymbol{x} \in \partial\Gamma_{out}, (\boldsymbol{u} - \boldsymbol{w}) \cdot \boldsymbol{n} > 0\} \tag{5.61}$$

the inflow and outflow portions of the boundary $\partial\Omega(t)$, respectively. At the inflow boundary we prescribe the total flux

$$(\boldsymbol{u}c)\cdot\boldsymbol{n} = (\boldsymbol{u}c_{in})\cdot\boldsymbol{n} \quad \text{on } \Gamma_-\times(0,T), \tag{5.62}$$

where c_{in} is the concentration at the inflow boundary. The initial condition is given by

$$c|_{t=0} = c_0 \quad \text{in } \hat{\Omega}. \tag{5.63}$$

We assume that the velocity field $\boldsymbol{u}$, the domain displacement $\boldsymbol{\eta}$, and the domain velocity $\boldsymbol{w}$, are given. Namely, they are determined in the previous steps by a numerical solution of a fluid-structure interaction problem.

Let ϕ be an admissible weight function. The weak formulation of (5.58) is given by [42]

$$\frac{d}{dt}\int_{\Omega(t)} c\phi d\boldsymbol{x} - \int_{\Omega(t)} \nabla\phi\cdot((\boldsymbol{u}-\boldsymbol{w})c)d\boldsymbol{x} + \int_{\Gamma_-(t)} \phi(\boldsymbol{u}c_{in})\cdot\boldsymbol{n}ds + \int_{\Gamma_+(t)} \phi(\boldsymbol{u}c)\cdot\boldsymbol{n}ds = 0, \quad \forall\phi. \tag{5.64}$$

Let $\mathcal{T}_h$ be a triangulation of Ω, and let $\{\phi_i\}$ be a set of $\mathbb{P}_1$ basis functions associated with the vertices $\{\boldsymbol{x}_j\}$ of $\mathcal{T}_h$. Using a finite element approach, the solution of (5.64) is approximated by

$$c_h(\boldsymbol{x},t) = \sum_j c_j(t)\varphi_j(\boldsymbol{x}),$$

and

$$(\boldsymbol{u}c)_h(\boldsymbol{x},t) = \sum_j \boldsymbol{u}_j c_j(t)\varphi_j(\boldsymbol{x}).$$

Substituting c by c_h and $\boldsymbol{u}c$ by $(\boldsymbol{u}c)_h$, and taking $\phi=\varphi_i,\ i=1,\dots,n$, we obtain

$$\sum_{j=1}^{n}\frac{d}{dt}\int_{\Omega(t)} c_j(t)\varphi_j\varphi_i d\boldsymbol{x} - \sum_{j=1}^{n}(\boldsymbol{u}_j-\boldsymbol{w}_j)c_j(t)\cdot\int_{\Omega(t)}\nabla\varphi_i\varphi_j d\boldsymbol{x} + \int_{\Gamma_-(t)}(\boldsymbol{u}c_{in}\cdot\boldsymbol{n})\varphi_i ds$$

$$+\sum_{j=1}^{n} \boldsymbol{u}_j c_j(t) \cdot \int_{\Gamma_+(t)} \varphi_j \varphi_i \boldsymbol{n} ds = 0, \quad \forall\, i = 1, \ldots, n.$$

Remark 5.2.4. The triangulation $\mathcal{T}_h$ used here is the one used to approximate velocity in the Stokes sub-problem.

Let $M_C(t) = \{m_{ij}(t)\}$, $K(t) = \{k_{ij}(t)\}$ and $q(t) = \{q_i(t)\}$ be defined as follows:

$$m_{ij}(t) = \int_{\Omega(t)} \varphi_j \varphi_i d\boldsymbol{x}, \quad q_i = -\int_{\Gamma_-(t)} (\boldsymbol{u} c_{in} \cdot \boldsymbol{n}) \varphi_i ds,$$

$$k_{ij}(t) = -\boldsymbol{u}_j \cdot \int_{\Gamma_+(t)} \varphi_j \varphi_i \boldsymbol{n} ds + (\boldsymbol{v}_j - \boldsymbol{w}_j) \int_{\Omega(t)} \nabla \varphi_i \cdot \varphi_j d\boldsymbol{x}.$$

Let $c(t) = \{c_j\}$ be the vector of nodal values. Then, we can write our problem as the following semi-discrete system

$$\frac{d}{dt}[M_C(t)c(t)] = K(t)c(t) + q(t), \quad t \in (t^n, t^{n+1}). \tag{5.65}$$

In certain flow regimes, the Galerkin discretization of the advection equation is known to become unstable and produce oscillations in the proximity to steep fronts. This may cause the concentration c to assume non-physical negative values. To rectify this, we use the algebraic flux correction [57, 58] to constrain the coefficients of the Galerkin scheme. We begin the modification by a conservative elimination of matrix entries that do not satisfy the positivity constraint. First, the mass matrix M_C is replaced by

$$M_L = diag\{m_i\}, \quad m_i = \sum_j m_{ij}. \tag{5.66}$$

Next, we add an artificial diffusion operator D to construct a non-oscillatory low-order counterpart of the discrete advection operator K:

$$L = K + D, \tag{5.67}$$

where D is defined as follows [57, 58]

$$d_{ij} = \max\{-k_{ij}, 0, -k_{ji}\} = d_{ji}, \quad j \neq i, \tag{5.68}$$

and

$$d_{ii} = -\sum_{j \neq i} d_{ij}, \ i = 1, \ldots, n. \tag{5.69}$$

Substituting M_C by M_L and K by L, one obtains the low-order approximation

$$\frac{d}{dt}[M_L(t)c(t)] = L(t)c(t) + q(t), \quad t \in (t^n, t^{n+1}). \tag{5.70}$$

Integrating (5.70) in time one obtains

$$M_L(t^{n+1})c(t^{n+1}) = M_L(t^n)c(t^n) + \int_{t^n}^{t^{n+1}} L(t)c(t)dt + \int_{t^n}^{t^{n+1}} q(t)dt. \tag{5.71}$$

The fully discrete problem now reads

$$Ac^L = Bc^n + \triangle t q^{n+1/2}, \tag{5.72}$$

where the integrals in (5.71) are approximated by the midpoint rule and

$$A = M_L^{n+1} - \frac{\triangle t}{2} L^{n+1/2}, \tag{5.73}$$

$$B = M_L^n + \frac{\triangle t}{2} L^{n+1/2}. \tag{5.74}$$

Matrix A is the so-called M-matrix whose inverse A^{-1} has no negative entries [58]. Entries of B are also non-negative if the time step Δt is sufficiently small. The source term q is non-negative since $\boldsymbol{u} \cdot \boldsymbol{n} < 0$ at Γ_-. This proves that the scheme is positivity-preserving.

To preform the anti-diffusive correction of c^L note that the difference between the residuals of systems (5.65) and (5.70) is the vector

$$f = (M_L - M_C)\frac{dc}{dt} - Dc. \tag{5.75}$$

As proposed by Kuzmin [57], the *raw antidiffusive fluxes* f_{ij} can be evaluated using the predictor c^L. Denote by $\dot{c}_i^L$ a numerical approximation of $\frac{dc_i^L}{dt}$ and let

$$f_{ij} = m_{ij}(\dot{c}_i^L - \dot{c}_j^L) + d_{ij}(c_i^L - c_j^L), \quad f_{ji} = -f_{ij}. \tag{5.76}$$

If the flux f_{ij} has the same sign as $(c_i^L - c_j^L)$, we set $f_{ij} := 0$ because then f_{ij} is diffusive in nature and tends to flatten the solution profile instead of steepening it. We apply the sum of limited antidiffusive fluxes multiplied by a solution-dependent correction factor α_{ij} to the low-order solution c^L:

$$M_L^{n+1}c^{n+1} = M_L^{n+1}c^L + \triangle t\bar{f}, \quad \bar{f}_i = \sum_{j\neq i}\alpha_{ij}f_{ij}. \tag{5.77}$$

The correction factors $\alpha_{ij} \in [0,1]$ are chosen so that the nodal values of the final solution c^{n+1} are bounded by the local maxima and minima of c^L. Namely, the correction factors α_{ij} are obtained using the Zalesak's limiter [91] as follows:

1. Compute the sums of positive/negative antidiffusive fluxes into node i

$$P_i^+ = \sum_{j\neq i}\max\{0, f_{ij}\}, \quad P_i^- = \sum_{j\neq i}\min\{0, f_{ij}\}. \tag{5.78}$$

2. Compute the distance to a local extremum of the auxiliary solution c^L

$$Q_i^+ = \max\{0, \max_{j\neq i}(c_j^L - c_i^L)\}, \quad Q_i^- = \min\{0, \min_{j\neq i}(c_j^L - c_i^L)\}. \tag{5.79}$$

3. Compute the nodal correction factors for the net increment to node i

$$R_i^+ = \min\{1, \frac{m_i Q_i^+}{\triangle t P_i^+}\}, \quad R_i^- = \min\{1, \frac{m_i Q_i^-}{\triangle t P_i^-}\}. \tag{5.80}$$

4. Define α_{ij} so as to satisfy the positivity constraint for nodes i and j

$$\alpha_{ij} = \begin{cases} \min\{R_i^+, R_j^-\}, & \text{if } f_{ij} > 0, \\ \min\{R_i^-, R_j^+\}, & \text{otherwise.} \end{cases} \tag{5.81}$$

This completes a description of the positivity preserving ALE scheme.

5.2.2.2 A wave-like equation method

Consider the following transport problem for c:

$$\frac{\partial c}{\partial t} + \boldsymbol{u}^{n+1/3} \cdot \nabla c = 0 \quad \text{in } \Omega(t^n) \times (t^n, t^{n+1}), \tag{5.82}$$

$$c(t^n) = c^{n+1/3}, \tag{5.83}$$

$$c = c_{in} \quad \text{on } \Gamma_-^{n+1/3} \times (t^n, t^{n+1}), \tag{5.84}$$

where $\boldsymbol{u}^{n+1/3}$ is given, and such that $\boldsymbol{u}^{n+1/3}$ is independent of time on (t^n, t^{n+1}). Assume also that

$$\nabla \cdot \boldsymbol{u}^{n+1/3} = 0 \ \text{ in } \Omega(t^n) \times (t^n, t^{n+1}), \tag{5.85}$$

$$\frac{\partial c_{in}}{\partial t} = 0 \ \text{ on } \Gamma_-^{n+1/3} \times (t^n, t^{n+1}), \tag{5.86}$$

where

$$\Gamma_-^{n+1/3} = \{\boldsymbol{x} \in \mathbb{R}^2 | \boldsymbol{x} \in \partial\Omega(t^n), \boldsymbol{u}^{n+1/3} \cdot \boldsymbol{n} < 0\}. \tag{5.87}$$

Initial condition $c^{n+1/3}$ is equal to $u_z^{n+1/3}$ for the transport of u_z, and $u_r^{n+1/3}$ for the transport of u_r. Analogous holds for c_{in}.

Taking the time derivative of equation (5.82) and using condition $\dfrac{\partial \boldsymbol{u}^{n+1/3}}{\partial t} = 0$, one obtains

$$\frac{\partial^2 c}{\partial t^2} + \boldsymbol{u}^{n+1/3} \cdot \nabla \frac{\partial c}{\partial t} = 0 \quad \text{in } \Omega(t^n) \times (t^n, t^{n+1}). \tag{5.88}$$

Combining the transport equation (5.82) with (5.88) we obtain the following *wave-like equation problem*

$$\frac{\partial^2 c}{\partial t^2} - \boldsymbol{u}^{n+1/3} \cdot \nabla(\boldsymbol{u}^{n+1/3} \cdot \nabla c) = 0 \quad \text{in } \Omega(t^n) \times (t^n, t^{n+1}), \tag{5.89}$$

$$c(t^n) = c^{n+1/3}, \quad \frac{\partial c}{\partial t}(t^n) = -\boldsymbol{u}^{n+1/3} \cdot \nabla c^{n+1/3}, \tag{5.90}$$

$$c = c_{in} \quad \text{on } \Gamma_-^{n+1/3} \times (t^n, t^{n+1}), \tag{5.91}$$

$$\boldsymbol{u}^{n+1/3} \cdot \boldsymbol{n}(\frac{\partial c}{\partial t} + \boldsymbol{u}^{n+1/3} \cdot \nabla c) = 0 \quad \text{on } (\partial\Omega(t^n) \backslash \Gamma_-^{n+1/3}) \times (t^n, t^{n+1}). \tag{5.92}$$

To write the weak formulation of the problem (5.89)-(5.92) let $\Gamma_+^{n+1/3} = \{\boldsymbol{x} \in \mathbb{R}^2 | \boldsymbol{x} \in \partial\Omega(t^n), \boldsymbol{u}^{n+1/3} \cdot \boldsymbol{n} > 0\}$ and define the space of test function by

$$\Phi_0 = \{\phi \,|\, \phi \in H^1(\Omega(t^n)), \phi = 0 \text{ on } \Gamma_-^{n+1/3}\}. \tag{5.93}$$

After multiplying (5.89) by a test function $\phi \in \Phi_0$, and after using the divergence theorem and assuming c is smooth enough, any solution c of (5.89)-(5.92) satisfies

$$\begin{aligned}
&\int_{\Omega(t^n)} \frac{\partial^2 c}{\partial t^2} \phi d\boldsymbol{x} + \int_{\Omega(t^n)} (\boldsymbol{u}^{n+1/3} \cdot \nabla c)(\boldsymbol{u}^{n+1/3} \cdot \nabla \phi) d\boldsymbol{x} \\
&\qquad + \int_{\Gamma_+^{n+1/3}} \boldsymbol{u}^{n+1/3} \cdot \boldsymbol{n} \frac{\partial c}{\partial t} \phi ds = 0, \quad \forall \phi \in \Phi_0, \text{ a.e. on } (t^n, t^{n+1}), \\
&c(t^n) = c^{n+1/3}, \quad \frac{\partial c}{\partial t}(t^n) = -\boldsymbol{u}^{n+1/3} \cdot \nabla c^{n+1/3}, \\
&c = c_{in} \quad \text{on } \Gamma_-^{n+1/3} \times (t^n, t^{n+1}).
\end{aligned}$$

It was shown in [44], Chapter 6, Section 31.5.2., that any smooth solution of the transport problem (5.82)-(5.84) is also a solution of the wave-like equation problem (5.89)-(5.92).

To solve this problem numerically, define $\mathcal{T}_h$ to be a finite element triangulation

of $\Omega(t^n)$ defined as in (5.28), and let

$$\Phi_h = \{\phi_h \mid \phi_h \in C^0(\bar{\Omega}(t^n)), \phi_h|_T \in \mathbb{P}_1, \forall T \in \mathcal{T}_h\}, \tag{5.94}$$

$$\Phi_{0h} = \{\phi_h \mid \phi_h \in \Phi_h, \phi_h = 0 \text{ on } \Gamma_-^{n+1/3}\}. \tag{5.95}$$

Remark 5.2.5. As in the positivity-preserving ALE finite element scheme, the triangulation $\mathcal{T}_h$ used here is the one used to approximate velocity in the Stokes subproblem.

We assume that the set of vertices of $\mathcal{T}_h$ contains the points at the interface of $\Gamma_-^{n+1/3}$ and $\partial\Omega(t^n)\backslash\Gamma_-^{n+1/3}$ and of $\Gamma_+^{n+1/3}$ and $\partial\Omega(t^n)\backslash\Gamma_+^{n+1/3}$, and that

$$\lim_{h\to 0} \Phi_h = H^1(\Omega(t^n)), \quad \lim_{h\to 0} \Phi_{0h} = \Phi_0. \tag{5.96}$$

With this notation, the finite element approximation of problem (5.89)-(5.92) reads as follows:

$$c_h(t^n) = c_h^{n+1/3} \in \Phi_h, \quad c_h^{n+1/3} \simeq c^{n+1/3}, \tag{5.97}$$

$$\frac{\partial c_h}{\partial t}(t^n) = c_{1h} \in V_{0h}, \tag{5.98}$$

$$\int_{\Omega(t^n)} c_{1h}\phi_h d\boldsymbol{x} = -\int_{\Omega(t^n)} \boldsymbol{u}^{n+1/3} \cdot \nabla c_h^{n+1/3} \phi_h d\boldsymbol{x}, \quad \forall \phi_h \in \Phi_{0h}, \tag{5.99}$$

$$c_h(t) \in \Phi_h,\ c_h(t) = c_{in,h} \quad \text{on } \Gamma_-^{n+1/3}, \forall t \in [t^n, t^{n+1}], \tag{5.100}$$

$$\int_{\Omega(t^n)} \frac{\partial^2 c_h}{\partial t^2}\phi_h d\boldsymbol{x} + \int_{\Omega(t^n)} (\boldsymbol{u}^{n+1/3} \cdot \nabla c_h)(\boldsymbol{u}^{n+1/3} \cdot \nabla \phi_h) d\boldsymbol{x} \tag{5.101}$$

$$+ \int_{\Gamma_+^{n+1/3}} \boldsymbol{u}^{n+1/3} \cdot \boldsymbol{n} \frac{\partial c_h}{\partial t}\phi_h dS = 0, \quad \forall \phi_h \in V_{0h}, \text{ a.e. on } (t^n, t^{n+1}). \tag{5.102}$$

Denote by Σ_h the set of vertices of $\mathcal{T}_h$

$$\Sigma_h = \{P \mid P \in \bar{\Omega}, P \text{ is a vertex of } \mathcal{T}_h\}, \tag{5.103}$$

and by $\Sigma_{0h} \subset \Sigma_h$ the set of vertices of $\mathcal{T}_h$ that are not on $\bar{\Gamma}_-^{n+1/3}$

$$\Sigma_{0h} = \{P \mid P \in \Sigma_h, P \notin \bar{\Gamma}_-^{n+1/3}\}. \tag{5.104}$$

We order the elements in Σ_h in the following way

$$\Sigma_h = \Sigma_{0h} \cup \{P_j\}_{j=N_{0h}+1}^{N_h}, \tag{5.105}$$

where $N_h := \dim(\Phi_h) = Card(\Sigma_h)$ and $N_{0h} := \dim(\Phi_{0h}) = Card(\Sigma_{0h})$. Let $\{\phi_j\}_{j=1}^{N_h}$ be a set of $\mathbb{P}_1$ basis functions associated with vertices $P_j \in \Sigma_h$ of $\mathcal{T}_h$ such that $\varphi_j \in \Phi_h, \forall j = 1, \ldots, N_h$, and

$$\varphi_j(P_i) = \delta_{ij}, \quad \forall i, j = 1, \ldots, N_h. \tag{5.106}$$

Then we can approximate c_h by

$$c_h(t) = \sum_{j=1}^{N_{0h}} c_j(t)\varphi_j + \sum_{j=N_{0h}+1}^{N_h} c_{in,h}(P_j)\varphi_j. \tag{5.107}$$

Substituting (5.107) into (5.97)-(5.102), and by replacing ϕ_h by $\varphi_i,\ i = 1, \ldots, N_{0h}$ we obtain

$$\begin{aligned}
&\sum_{j=1}^{N_{0h}} c_j''(t) \int_{\Omega(t^n)} \varphi_j\varphi_i d\boldsymbol{x} + \sum_{j=1}^{N_{0h}} c_j(t) \int_{\Omega(t^n)} (\boldsymbol{u}\cdot\nabla\varphi_i)(\boldsymbol{u}\cdot\nabla\varphi_j) d\boldsymbol{x} \\
&+ \sum_{j=1}^{N_{0h}} c_j'(t) \int_{\Gamma_+^{n+1/3}(t)} (\boldsymbol{u}\cdot\boldsymbol{n})\varphi_i\varphi_j dS \\
&= -\sum_{j=N_{0h}+1}^{N_h} c_{in,h}(P_j) \int_{\Omega(t^n)} (\boldsymbol{u}\cdot\nabla\varphi_i)(\boldsymbol{u}\cdot\nabla\varphi_j) d\boldsymbol{x},\ \forall\ i = 1, \ldots, N_{0h}.
\end{aligned} \tag{5.108}$$

Define the $N_{0h} \times N_{0h}$ matrices M, A and C by

$$\begin{aligned}
M &= (m_{ij})_{1\le i,j\le N_{0h}}, \quad & m_{ij} &= \textstyle\int_{\Omega(t^n)} \varphi_i\varphi_j d\boldsymbol{x}, \\
A &= (a_{ij})_{1\le i,j\le N_{0h}}, \quad & a_{ij} &= \textstyle\int_{\Omega(t^n)} (\boldsymbol{u}\cdot\nabla\varphi_i)(\boldsymbol{u}\cdot\nabla\varphi_j) d\boldsymbol{x}, \\
C &= (c_{ij})_{1\le i,j\le N_{0h}}, \quad & c_{ij} &= \textstyle\int_{\Gamma_+(t^n)} (\boldsymbol{u}\cdot\boldsymbol{n})\varphi_i\varphi_j dS,
\end{aligned} \tag{5.109}$$

and the forcing term vector $F = \{f_i\}_{i=1}^{N_{0h}}$ by

$$f_i = -\Sigma_{j=N_{0h}+1}^{N_h} c_{in}(P_j) \int_{\Sigma_{t^n}} (\boldsymbol{u} \cdot \nabla \varphi_i)(\boldsymbol{u} \cdot \nabla \varphi_j) d\boldsymbol{x}. \tag{5.110}$$

Then equation (5.108) can be written as

$$\begin{cases} M\ddot{X} + AX + C\dot{X} = F \quad \text{on } (t^n, t^{n+1}), \\ X(0) = X_0, \quad \dot{X}(0) = X_1, \end{cases} \tag{5.111}$$

where $X(t) = \{c_i(t)\}_{i=1}^{N_{0h}}$, $X_0 = \{c_h^{n+1/3}(P_i)\}_{i=1}^{N_{0h}}$ and $\dot{X}(t) = \{c_{1h}(P_i)\}_{i=1}^{N_{0h}}$.

Matrices A and C are symmetric and positive semi-definite, while M is symmetric positive definite. We discretise equation (5.111) in time following the approach in [44]:

$$M\frac{X^{n+1} - 2X^n + X^{n-1}}{\tau_a^2} + A(\alpha X^{n+1} + (1-2\alpha)X^n + \alpha X^{n-1}) \tag{5.112}$$

$$+C\frac{X^{n+1} - X^{n-1}}{2\tau_a} = F^n \quad \text{for } n = 0, 1, \ldots N-1, \tag{5.113}$$

$$X^0 = X_0, \quad X^1 - X^{-1} = 2\tau_a X_1, \tag{5.114}$$

where $0 \leq \alpha \leq 1/2$ and $\tau_a = \triangle t/N$ is a time substep in (t^n, t^{n+1}). It was shown in [44] that this scheme is unconditionally stable for of $\alpha = 1/4$.

5.2.3 Elastodynamics of the deformable boundary

Problem 5.2.3 describes the elastodynamics of the thin, linearly elastic Koiter shell with the load that comes from a part of the fluid pressure. As mentioned in Remark 5.2.1, we can rewrite Problem 5.2.3 in the following way

$$\begin{cases} \rho_s h \frac{\partial^2 \eta_z}{\partial t^2} - (C_2 - \beta \hat{p}^{n+1}) \frac{\partial \eta_r}{\partial z} - C_3 \frac{\partial^2 \eta_z}{\partial z^2} = 0 \quad \text{on } (0, L) \times (t^n, t^{n+1}), \\ \rho_s h \frac{\partial^2 \eta_r}{\partial t^2} + C_0 \eta_r - C_1 \frac{\partial^2 \eta_r}{\partial z^2} + (C_2 - \beta \hat{p}^{n+1}) \frac{\partial \eta_z}{\partial z} + \frac{h^2}{12} C_3 \frac{\partial^4 \eta_r}{\partial z^4} \\ \qquad = \beta \hat{p}^{n+1} \quad \text{on } (0, L) \times (t^n, t^{n+1}), \end{cases} \tag{5.115}$$

with boundary conditions

$$\boldsymbol{\eta}|_{z=0} = 0, \ \boldsymbol{\eta}|_{z=L} = 0, \tag{5.116}$$

and initial conditions

$$\boldsymbol{\eta}(t^n) = \boldsymbol{\eta}^{n+2/3}, \tag{5.117}$$

$$\frac{\partial \boldsymbol{\eta}}{\partial t}(t^n) = \boldsymbol{u}^{n+2/3}|_{\Gamma}, \tag{5.118}$$

where $\boldsymbol{u}^{n+2/3}$, p^{n+1} and $\boldsymbol{\eta}^{n+2/3}$ are computed in the previous steps.

5.2.3.1 Space discretization

We discretise the problem in space using a second-order finite difference scheme. Let

$$\{z_i\}_{i=1,\dots,M}, \quad z_i = (i-1)\frac{L}{M-1} \tag{5.119}$$

be the set of points for the space discretization and denote by

$$X = [\eta_{z_1}, \dots, \eta_{z_M}, \eta_{r_1}, \dots, \eta_{r_M}]^\tau$$

the vector of space-discretized values of $\boldsymbol{\eta}$, by

$$X_0 = [\eta_{z_1}^{n+2/3}, \ldots, \eta_{z_M}^{n+2/3}, \eta_{r_1}^{n+2/3}, \ldots, \eta_{r_M}^{n+2/3}]^\tau$$

the vector of space-discretised values of $\boldsymbol{\eta}^{n+2/3}$, and by

$$X_1 = [(u_z^{n+2/3}|_\Gamma)_1, \ldots, (u_z^{n+2/3}|_\Gamma)_M, (u_r^{n+2/3}|_\Gamma)_1, \ldots, (u_r^{n+2/3}|_\Gamma)_M]^\tau$$

the vector of space-discretised values of $\boldsymbol{u}^{n+2/3}$.

Now we can write our problem as

$$\rho_s h\ddot{X} + AX = F, \tag{5.120}$$

$$X(0) = X_0,\ \dot{X}(0) = X_1, \tag{5.121}$$

where $\dot{X}$ denotes the time-derivative of X, $F = [f_z, f_r]^\tau$ and

$$A = \left[\begin{array}{c|c} A_1 & A_2 \\ \hline A_2^\tau & A_3 \end{array}\right], \tag{5.122}$$

where

$$A_1 = \begin{bmatrix} \frac{2C_3}{\triangle x^2} & \frac{-C_3}{\triangle x^2} & \ldots & 0 \\ \frac{-C_3}{\triangle x^2} & \ddots & \ddots & \vdots \\ \vdots & \ddots & \ddots & \frac{-C_3}{\triangle x^2} \\ 0 & \ldots & \frac{-C_3}{\triangle x^2} & \frac{2C_3}{\triangle x^2} \end{bmatrix},$$

$$A_2 = \begin{bmatrix} 0 & \frac{-(C_2-\beta\hat{p}^{n+1})}{2\triangle x} & \ldots & 0 \\ \frac{C_2-\beta\hat{p}^{n+1}}{2\triangle x} & \ddots & \ddots & \vdots \\ \vdots & \ddots & \ddots & \frac{-(C_2-\beta\hat{p}^{n+1})}{2\triangle x} \\ 0 & \ldots & \frac{C_2-\beta\hat{p}^{n+1}}{2\triangle x} & 0 \end{bmatrix},$$

and

$$A_3 = \begin{bmatrix} \frac{2C_1}{\triangle x^2} + C_0 + \frac{h^2 C_3}{2\triangle x^4} & \frac{-C_1}{\triangle x^2} - \frac{h^2 C_3}{3\triangle x^4} & \frac{h^2 C_3}{12\triangle x^4} & 0 & \dots & 0 \\ \frac{-C_1}{\triangle x^2} - \frac{h^2 C_3}{3\triangle x^4} & \ddots & \ddots & \ddots & & \vdots \\ \frac{h^2 C_3}{12\triangle x^4} & \ddots & \ddots & \ddots & \ddots & 0 \\ 0 & \ddots & \ddots & \ddots & \ddots & \frac{h^2 C_3}{12\triangle x^4} \\ \vdots & & \ddots & \ddots & \ddots & \frac{-C_1}{\triangle x^2} - \frac{h^2 C_3}{3\triangle x^4} \\ 0 & \dots & \dots & \frac{h^2 C_3}{12\triangle x^4} & \frac{-C_1}{\triangle x^2} - \frac{h^2 C_3}{3\triangle x^4} & \frac{2C_1}{\triangle x^2} + C_0 + \frac{h^2 C_3}{2\triangle x^4} \end{bmatrix}.$$

Note that A is a symmetric positive definite matrix.

5.2.3.2 Time discretization

Let us denote the vector X at a time t^k by X^k. We discretise equation (5.120) in time as suggested in [44]:

$$\frac{\rho_s h}{\tau^2}(X^{n+1} - 2X^n + X^{n-1}) + A(\alpha X^{n+1} + (1-2\alpha)X^n + \alpha X^{n-1}) = F^n, \quad (5.123)$$

$$X^0 = X_0, \quad X^1 - X^{-1} = 2\tau X_1, \quad (5.124)$$

for $n = 0, 1, \dots N-1$, where $0 \leq \alpha \leq 1/2$ and $\tau = \triangle t/N$ is a time substep in (t^n, t^{n+1}). We choose $\alpha = 1/4$ as it was shown in [44] that the scheme is unconditionally stable for this value of α.

Using this approach we compute X^1 as

$$2\left(\frac{\rho_s h}{\tau^2}I + \frac{1}{4}A\right)X^1 = F^0 + \left(\frac{2\rho_s h}{\tau^2}I - \frac{1}{2}A\right)X^0 + 2\tau\left(\frac{\rho_s h}{\tau^2}I + \frac{1}{4}A\right)X^1, \quad (5.125)$$

and X^{n+1}, for $n = 1, \dots, N-1$, as

$$\left(\frac{\rho_s h}{\tau^2}I + \frac{1}{4}A\right)X^{n+1} = F^n + \left(\frac{2\rho_s h}{\tau^2}I - \frac{1}{2}A\right)X^n - \left(\frac{\rho_s h}{\tau^2}I + \frac{1}{4}A\right)X^{n-1}. \quad (5.126)$$

5.3 Stability of the kinematically coupled β-scheme

In this section we discuss stability of the kinematically coupled scheme β-scheme in the case when the structure dynamics is governed by the Koiter shell. We perform the stability analysis on a simplified problem, similar to the one considered in [22]. This simplified problem retains the main difficulties associated with the "added mass effect" which is responsible for the loss of stability in "classical" loosely coupled schemes applied to blood flow.

5.3.1 The simplified problem

The simplified problem consists of solving the time-dependent Stokes equations for an incompressible inviscid fluid in a 2D channel with deformable walls, and with the elastodynamics equations given by the linearly elastic Koiter shell model capturing only radial displacement. Moreover, we assume the displacement of the deformable wall is small enough so that it can be neglected in the fluid flow problem. In this case the geometry of the fluid domain is fixed while the small deformation of the boundary is calculated using the elastodynamics equations coupled with the fluid flow through the kinematic and dynamic coupling conditions.

Thus, the problem is defined on the fluid domain

$$\Omega = (0, L) \times (0, R),$$

with the lateral boundary

$$\Gamma = \{(z, r) \in \mathbb{R}^2 \mid 0 < z < L,\ r = R\},$$

the bottom boundary Γ_b for which $r = 0$, and the inlet and outlet boundaries $\Gamma_{in/out}$ corresponding to $z = 0, L$, respectively.

We will be assuming that the inlet and outlet pressure data, which are functions of time, are uniformly bounded. This is a reasonable assumption for the blood flow application, since the pressure is typically a periodic function of time, with a bounded amplitude.

The **fluid problem** reads: Find the fluid velocity $\boldsymbol{u} = \boldsymbol{u}(z, r, t)$ and pressure $p = p(z, r, t)$ such that

$$\begin{cases} \rho_f \dfrac{\partial \boldsymbol{u}}{\partial t} + \nabla p = 0 & \text{in } \Omega \times (0,T), \\ \nabla \cdot \boldsymbol{u} = 0 & \text{in } \Omega \times (0,T), \\ \boldsymbol{u} \cdot \boldsymbol{n} = 0 & \text{on } \Gamma_b \times (0,T), \\ p = p_{in/out}(t) & \text{on } \Gamma_{in/out} \times (0,T), \\ \boldsymbol{u} \cdot \boldsymbol{n} = w & \text{on } \Gamma \times (0,T), \end{cases} \tag{5.127}$$

with the initial velocity and pressure equal to zero.

The **structure problem** is defined by solving for $\eta_r = \eta_r(z, t)$ the (simplified) Koiter shell equation

$$\rho_s h \frac{\partial^2 \eta_r}{\partial t^2} + C_0 \eta_r - C_1 \frac{\partial^2 \eta_r}{\partial z^2} = f, \tag{5.128}$$

with boundary conditions $\eta_r(0) = \eta_r(L) = 0$, and initial conditions given by the zero initial displacement and zero initial structure velocity.

The **coupling** between the fluid and structure is defined by the kinematic and

dynamic lateral boundary conditions:

$$\begin{aligned} f &= p|_\Gamma, \\ (\frac{\partial \eta_r}{\partial t}, 0) &= \boldsymbol{u}|_\Gamma. \end{aligned} \tag{5.129}$$

The coupled fluid-structure interaction problem can be written as follows:

Problem 5.3.1.

$$\begin{cases} \rho_f \dfrac{\partial \boldsymbol{u}}{\partial t} + \nabla p = 0 & in\ \Omega \times (0,T), \\ \nabla \cdot \boldsymbol{u} = 0 & in\ \Omega \times (0,T), \\ \boldsymbol{u} \cdot \boldsymbol{n} = 0 & on\ \Gamma_b \times (0,T), \\ p = p_{in/out}(t) & on\ \Gamma_{in/out} \times (0,T), \\ \boldsymbol{u} \cdot \boldsymbol{n} = \frac{\partial \eta_r}{\partial t} & on\ \Gamma \times (0,T), \\ p = \rho_s h \frac{\partial^2 \eta_r}{\partial t^2} + C_0 \eta_r - C_1 \frac{\partial^2 \eta_r}{\partial z^2} & on\ \Gamma \times (0,T). \end{cases} \tag{5.130}$$

To perform the Lie splitting, this system can be written as a first-order system by using the kinematic coupling condition in the structure equation to express the structure inertia in terms of the trace of fluid velocity on Γ to obtain:

$$\begin{cases} \rho_f \dfrac{\partial \boldsymbol{u}}{\partial t} + \nabla p = 0 & \text{in } \Omega \times (0,T), \\ \nabla \cdot \boldsymbol{u} = 0 & \text{in } \Omega \times (0,T), \\ \boldsymbol{u} \cdot \boldsymbol{n} = 0 & \text{on } \Gamma_b \times (0,T), \\ p = p_{in/out}(t) & \text{on } \Gamma_{in/out} \times (0,T), \\ \boldsymbol{u} \cdot \boldsymbol{n} = \frac{\partial \eta_r}{\partial t} & \text{on } \Gamma \times (0,T), \\ p = \rho_s h \frac{\partial (u_r|_\Gamma)}{\partial t} + C_0 \eta_r - C_1 \frac{\partial^2 \eta_r}{\partial z^2} & \text{on } \Gamma \times (0,T). \end{cases} \tag{5.131}$$

As before, this point is crucial in order to perform the splitting which gives rise to a stable scheme. Namely, in the fluid sub-problem, which we write next, the structure

inertia will be taken into account implicitly in the boundary condition on Γ, which is a crucial ingredient for the stability of the β-scheme.

Before we write the main splitting steps we also notice that the fluid stress, which in this simplified example is only the pressure, will be split into two parts: Part I which is given by $p-\beta p$, and Part 2 which is given by βp so that $p=(p-\beta p)+\beta p=$ Part 1 + Part 2.

Thus, the main steps of the Lie splitting for the simplified FSI problem (5.131) are:

Step 1. The Stokes problem is solved on a fixed fluid domain, where the fluid inertia is coupled to Part I of the fluid stress. Here, a portion of the stress (βp) is taken explicitly, while the rest is taken implicitly. The displacement of the structure stays intact. The problem reads:

Given p^n from the previous time step, find $\boldsymbol{u}, \eta_r$ and p such that for $t \in (t^n, t^{n+1})$:

$$\begin{cases} \rho_f \dfrac{\partial \boldsymbol{u}}{\partial t} + \nabla p &= 0 & \text{in } \Omega, \\ \nabla \cdot \boldsymbol{u} &= 0 & \text{in } \Omega, \\ \boldsymbol{u} \cdot \boldsymbol{n} &= 0 & \text{on } \Gamma_b, \\ p &= p_{in/out}(t) & \text{on } \Gamma_{in/out}, \\ p - \beta p^n &= \rho_s h \frac{\partial (u_r|_\Gamma)}{\partial t} & \text{on } \Gamma. \end{cases} \tag{5.132}$$

The structure displacement stays intact, namely

$$\frac{\partial \eta_r}{\partial t} = 0 \quad \text{on} \quad \Gamma. \tag{5.133}$$

The initial conditions are taken from the previous time step. Then set

$$\boldsymbol{u}^{n+1/2} = \boldsymbol{u}(t^{n+1}), \boldsymbol{u}|_\Gamma^{n+1/2} = \boldsymbol{u}|_\Gamma(t^{n+1}), p^{n+1} = p(t^{n+1}). \tag{5.134}$$

Step 2. The structure problem is solved and the kinematic coupling condition is enforced. The problem reads:

Find $\mathbf{u}$ *and* η_r *such that for* $t \in (t^n, t^{n+1})$ *the following holds:*

$$\begin{cases} \rho_s h \dfrac{\partial (u_r)|_\Gamma}{\partial t} + C_0 \eta_r - C_1 \dfrac{\partial^2 \eta_r}{\partial z^2} = \beta p^{n+1}|_\Gamma \quad on\ (0, L), \\ \dfrac{\partial \eta_r}{\partial t}(z,t) = u_r|_\Gamma \quad on\ (0, L) \end{cases}$$

The fluid velocity in Ω *remains intact, namely:*

$$\frac{\partial \boldsymbol{u}}{\partial t} = 0 \quad in\ \Omega.$$

Take the initial data to be the solution of the problem in Step 1 evaluated at t^{n+1}. *Then set*

$$\boldsymbol{u}^{n+1} = \boldsymbol{u}(t^{n+1}), \boldsymbol{u}|_\Gamma^{n+1} = \boldsymbol{u}|_\Gamma(t^{n+1}), \eta_r^{n+1} = \eta_r(t^{n+1}). \tag{5.135}$$

In this simplified model, the problem in Step 1 can entirely be formulated in terms of the pressure and the trace of fluid velocity on Γ. Namely, by taking the divergence free condition in the first (momentum) equation, the problem can be written in terms of the Laplace operator for the pressure. Similarly, we can re-write the boundary conditions on Γ in terms of the pressure and trace of the velocity on Γ. Namely, by differentiating the kinematic coupling condition with respect to t one obtains

$$\frac{\partial \boldsymbol{u}}{\partial t} \cdot \boldsymbol{n} = \frac{\partial^2 \eta_r}{\partial t^2}.$$

Using the partial differential equation relating $\boldsymbol{u}$ and p, one obtains

$$-\frac{1}{\rho_f} \frac{\partial p}{\partial \boldsymbol{n}} = \frac{\partial^2 \eta_r}{\partial t^2}.$$

Combining these two equations, the kinematic coupling condition can be replaced by

$$\frac{\partial p}{\partial \boldsymbol{n}} = -\rho_f \frac{\partial (u_r|_\Gamma)}{\partial t} \quad \text{on} \quad \Gamma. \tag{5.136}$$

Similarly, the dynamic coupling condition can be re-written as

$$\frac{\partial p}{\partial \boldsymbol{n}} = -\frac{\rho_f}{\rho_s h}(p - \beta p). \tag{5.137}$$

With this, the problem in Step 1 can be stated as:

Step 1'. *Find p and $u_r|_\Gamma$ such that for $t \in (t^n, t^{n+1})$:*

$$\begin{cases} -\triangle p &= 0, & \text{in } \Omega, \\ p &= p_{in/out}(t) & \text{on } \Gamma_{in/out}, \\ \dfrac{\partial p}{\partial \boldsymbol{n}} &= 0 & \text{on } \Gamma_b, \\ p + \dfrac{\rho_s h}{\rho_f}\dfrac{\partial p}{\partial \boldsymbol{n}} &= \beta p^n & \text{on } \Gamma, \\ - - - - - - & - - & - - - - - - & - - - \\ \dfrac{\partial (u_r|_\Gamma)}{\partial t} &= -\dfrac{1}{\rho_f}\dfrac{\partial (p|_\Gamma)}{\partial \boldsymbol{n}} & \text{on } \Gamma, \end{cases}$$

The first four equations in Step 1', supplemented by the initial data for the pressure, determine a time-dependent Robin problem for the pressure. The time-dependence enters through the inlet and outlet pressure data, which are functions of time. Notice that this problem already incorporates a portion of the coupling of the underlying moving boundary problem. This problem has a unique solution in the space $C(0, \infty; H^1(\Omega))$ provided that the data $p_{in/out} \in C(0, \infty; H^{1/2}(\Gamma_{in/out}))$, and $p^n \in C(0, \infty; H^{1/2}(\Gamma))$.

One can also show (see e.g., [22]) that the problem for the structure, defined in Step 2, has a unique solution $\eta \in C([0,\infty); H_0^1(0,L))$ provided that the initial data are such that $\eta|_{t=0} \in H_0^1(0,L)$, and $\partial\eta/\partial t|_{t=0} \in H_0^1(0,L)$, with $p^{n+1}|_\Gamma \in C(0,\infty; H^{1/2}(\Gamma))$.

To simplify notation, as in [22], we introduce a linear, symmetric, positive definite operator $\mathcal{L}$ defined by the elasticity tensor associated with the structure problem. Namely, for $\eta, \xi \in H_0^1(0,L)$, we define

$$< \mathcal{L}\eta, \xi >:= a_S(\eta, \xi), \tag{5.138}$$

where $a_S(\eta,\xi)$ is the inner product on $H^1(0,L)$ defined by

$$a_S(\eta,\xi) := \int_0^L C_0 \eta\xi dx + \int_0^L C_1 \frac{\partial\eta}{\partial x}\frac{\partial\xi}{\partial x} dx, \quad \forall \eta, \xi \in H^1(0,L).$$

With this notation, the structure equation in Step 2 can be written as

$$\rho_s h \frac{\partial^2 \eta_r}{\partial t^2} + \mathcal{L}\eta_r = \beta p^{n+1}|_\Gamma.$$

Operator $\mathcal{L}$ can be extended to the full structure operator defining the Koiter shell model, described in Section 2.

We now summarize the main steps of the splitting sheme. With a slight abuse of notation, we emphasize the discretized form of the Lie splitting, defining our kinematically coupled β-scheme:

Step 1. *Given* $u_r^n|_\Gamma$, p^n, η^n, *find* $p^{n+1/2}$, $u_r^{n+1/2}|_\Gamma$, $\eta^{n+1/2}$, *such that for* $t \in (t^n, t^{n+1})$:

$$\left\{\begin{array}{rcll} -\triangle p^{n+1/2} & = & 0, & \text{in } \Omega, \\ p^{n+1/2} & = & p_{in/out}(t) & \text{on } \Gamma_{in/out}, \\ \dfrac{\partial p^{n+1/2}}{\partial \boldsymbol{n}} & = & 0 & \text{on } \Gamma_b, \\ p^{n+1/2} + \dfrac{\rho_s h}{\rho_f}\dfrac{\partial p^{n+1/2}}{\partial \boldsymbol{n}} & = & \beta p^n & \text{on } \Gamma, \\ - - - - - & - - & - - - - - & - - - \\ \dfrac{\partial (u_r^{n+1/2}|_\Gamma)}{\partial t} & = & -\dfrac{1}{\rho_f}\dfrac{\partial (p^{n+1/2}|_\Gamma)}{\partial \boldsymbol{n}} & \text{on } \Gamma, \\ \eta^{n+1/2} & = & \eta^n & \text{on } \Gamma. \end{array}\right.$$

with the initial data given by $u_r^n|_\Gamma$, p^n, η^n.

Step 2. *Given* $p^{n+1/2}$, $u_r^{n+1/2}|_\Gamma$, $\eta^{n+1/2}$ *find* p^{n+1}, $u_r^{n+1}|_\Gamma$, η^{n+1}, *such that for* $t \in (t^n, t^{n+1})$:

$$\left\{\begin{array}{rcll} \rho_s h\dfrac{\partial^2 \eta^{n+1}}{\partial t^2} + \mathcal{L}\eta^{n+1} & = & \beta p^{n+1/2}|_\Gamma & \text{on } \Gamma \\ u_r^{n+1}|_\Gamma & = & \frac{\partial \eta^{n+1}}{\partial t} & \text{on } \Gamma \\ p^{n+1} & = & p^{n+1/2} & \text{on } \Omega. \end{array}\right.$$

with the initial data given by $p^{n+1/2}$, $u_r^{n+1/2}|_\Gamma$, $\eta^{n+1/2}$ *at* t^{n+1}.

We study stability of the kinematically coupled β-scheme next.

5.3.2 Stability

To study stability we introduce an operator $\mathcal{P} : H^{-1/2}(\Gamma) \to Q$, where

$$Q = \{q \in H^1(\Omega) \mid q|_{\Gamma_{in/out}} = 0\}, \tag{5.139}$$

such that

$$\begin{cases} -\triangle \mathcal{P}w &= 0, \quad \text{in } \Omega, \\ \mathcal{P}w &= 0 \quad \text{on } \Gamma_{in/out}, \\ \dfrac{\partial \mathcal{P}w}{\partial \boldsymbol{n}} &= 0 \quad \text{on } \Gamma_b, \\ \mathcal{P}w + \dfrac{\rho_s h}{\rho_f}\dfrac{\partial \mathcal{P}w}{\partial \boldsymbol{n}} &= w \quad \text{on } \Gamma. \end{cases} \tag{5.140}$$

Thus, operator $\mathcal{P}$ associates to every $w \in H^{-1/2}(\Gamma)$ the solution of the pressure problem in Step 1', with the homogeneous inlet and outlet data $p_{in/out} = 0$.

We are interested in the trace on Γ of this pressure solution. For this purpose, introduce the operator $\mathcal{S} : H^{-1/2}(\Gamma) \to H^{1/2}(\Gamma)$ by

$$\mathcal{S}w = \mathcal{P}w|_{\Gamma}. \tag{5.141}$$

One can prove (see [22]), the following standard results:

Proposition 5.3.1. *The operator $\mathcal{S}$ satisfies the following properties:*

1. *The operator $\mathcal{S} : H^{-1/2}(\Gamma) \to H^{1/2}(\Gamma)$ is continuous.*

2. *The operator $\mathcal{S}$ is compact, self-adjoint, and positive on $L^2(\Gamma)$.*

To study the solution of the corresponding non-homogeneous problem with $p = p_{in/out}(t)$ on $\Gamma_{in/out}$, let us introduce an arbitrary continuous extension operator $E_F : H^{1/2}(\partial\Omega\backslash\Gamma) \to H^1(\Omega)$ so that $E_F q|_{\partial\Omega\backslash\Gamma} = q$ and $||E_F q||_{H^1(\Omega)} \leq C||q||_{H^{1/2}(\partial\Omega\backslash\Gamma)}$. Let

$p^* \in C(0,\infty;H^1(\Omega))$ be the solution to

$$\begin{cases} -\triangle p^* &= \triangle E_F\bar{p}, & \text{in } \Omega, \\ p^* &= 0 & \text{on } \Gamma_{in/out}, \\ \dfrac{\partial p^*}{\partial \boldsymbol{n}} &= -\dfrac{\partial E_F\bar{p}}{\partial \boldsymbol{n}} & \text{on } \Gamma_b, \\ p^* + \dfrac{\rho_s h}{\rho_f}\dfrac{\partial p^*}{\partial \boldsymbol{n}} &= -\dfrac{\partial E_F\bar{p}}{\partial \boldsymbol{n}} & \text{on } \Gamma, \end{cases}$$

where $\bar{p} = p_{in/out}$ on $\Gamma_{in/out}$. Now, the solution to the pressure problem in Step 1' is given by

$$p = p^* + E_F\bar{p} - \mathcal{P}(\beta p^n). \tag{5.142}$$

Let us denote

$$p_{ext} = p^*|_\Gamma + E_F\bar{p}|_\Gamma. \tag{5.143}$$

Now we can write the trace of the pressure solution in Step 1' on Γ as

$$p|_\Gamma = p_{ext} - \mathcal{S}(\beta p^n). \tag{5.144}$$

This trace of the pressure is used to load the equation for the structure in Step 2. Thus, the structure problem in Step 2 can now be written as:

Find $\eta_r \in V_s$ such that

$$\rho_s h\frac{\partial^2\eta_r}{\partial t^2} + \mathcal{L}\eta_r = \beta(p_{ext}^{n+1} - \mathcal{S}(\beta p^n)). \tag{5.145}$$

One way to discretize this equation in time is to use an implicit marching scheme

$$\rho_s h\frac{\eta_r^{n+1} - 2\eta_r^n + \eta_r^{n-1}}{\triangle t^2} + \mathcal{L}\eta_r^{n+1} = \beta(p_{ext}^{n+1} - \mathcal{S}(\beta p^n)). \tag{5.146}$$

This scheme is unconditionally stable (provided that the right hand-side is "reasonable").

We chose to discretize equation (5.145) in time using the θ-scheme, as suggested in [44]:

$$\rho_s h \frac{\eta_r^{n+1} - 2\eta_r^n + \eta_r^{n-1}}{\triangle t^2} + \mathcal{L}(\theta\eta_r^{n+1} + (1-2\theta)\eta_r^n + \theta\eta_r^{n-1}) = \beta(p_{ext}^{n+1} - \mathcal{S}(\beta p^n)). \quad (5.147)$$

It was shown in [44] that, for a given fixed right-hand side (source term), this scheme is stable for all $0 \leq \theta \leq 1/2$. Thus, we have unconditional stability with respect to the arbitrary ratios of fluid and structure densities, provided that the right-hand side of this equation is "reasonable".

A crucial point to observe here is that the right-hand side of this equation, which comes from the pressure loading, is given by an iterative procedure, and can be written entirely in terms of the initial pressure, the external pressure ($p_{in/out}$), and the the operator $\mathcal{S}$ whose maximum eigenvalue, as we shall show below, is always less than 1, for all the choices of ρ_f and ρ_s. Moreover, we will show below that the right-hand side converges, as the number of iterations $n \to \infty$, if $0 \leq \beta \leq 1$, for all the choices of ρ_f and ρ_s.

To analyze the righ-hand side of equation (5.145), we first study the eigenvalues of operator $\mathcal{S}$. As we shall see below, it is convenient to express the eigenvalues of $\mathcal{S}$ via the eigenvalues of the "Neumann to Dirichlet" operator $\mathcal{M}_A : H^{-1/2}(\Gamma) \to H^{1/2}(\Gamma)$ which is defined to be the trace on Γ of the operator $\mathcal{R} : H^{-1/2}(\Gamma) \to Q$:

$$\mathcal{M}_A w = \mathcal{R}w|_\Gamma, \quad (5.148)$$

where $\mathcal{R}$ associates to every $w \in H^{-1/2}(\Gamma)$ the solution $\mathcal{R}w \in Q$ of the following

(pressure) problem:

$$\begin{cases} -\triangle \mathcal{R}w &= 0, \quad \text{in } \Omega, \\ \mathcal{R}w &= 0 \quad \text{on } \Gamma_{in/out}, \\ \dfrac{\partial \mathcal{R}w}{\partial \boldsymbol{n}} &= 0 \quad \text{on } \Gamma_b, \\ \dfrac{\partial \mathcal{R}w}{\partial \boldsymbol{n}} &= w \quad \text{on } \Gamma. \end{cases}$$

It can be shown (see [22]) that operator $\mathcal{M}_A : H^{-1/2}(\Gamma) \to H^{1/2}(\Gamma)$ is continuous, and that $\mathcal{M}_A$ is compact, self-adjoint, and positive on $L^2(\Gamma)$. Moreover, the eigenvalues μ_i of $\mathcal{M}_A$ are decreasing to zero ($\mu_i = L/(i\pi \text{th}(i\pi R/L))$, i = 1,2,...), with the maximum eigenvalue μ_{max} given by

$$\mu_{max} = \mu_1 = \frac{L}{\pi \text{th}(\dfrac{\pi R}{L})}.$$

We will use this knowledge to calculate the eigenvalues of operator $\mathcal{S}$. Let μ be an eigenvalue of operator $\mathcal{M}_A$. Then there exists a vector $v \neq 0$ such that

$$\mathcal{M}_A v = \mu v.$$

Recall that, by definition of $\mathcal{M}_A$, $\mathcal{M}_A v = \mathcal{R}v|_\Gamma$. Using this, we calculate

$$\mathcal{R}v|_\Gamma + \frac{\rho_s h}{\rho_f} \frac{\partial \mathcal{R}v}{\partial n}|_\Gamma = (\mu + \frac{\rho_s h}{\rho_f}) v|_\Gamma.$$

This implies that $\mathcal{R}$ also satisfies the following Robin problem:

$$\begin{cases} -\triangle \mathcal{R}g &= 0, & \text{in } \Omega, \\ \mathcal{R}g &= 0 & \text{on } \Gamma_{in/out}, \\ \dfrac{\partial \mathcal{R}g}{\partial \boldsymbol{n}} &= 0 & \text{on } \Gamma_b, \\ \mathcal{R}g + \dfrac{\rho_s h}{\rho_f} \dfrac{\partial \mathcal{R}g}{\partial \boldsymbol{n}} &= \big(\mu + \dfrac{\rho_s h}{\rho_f}\big) v & \text{on } \Gamma. \end{cases}$$

But this is precisely the problem defined by the operator $\mathcal{P}$ in (5.140), with the data on Γ given by $(\mu + \frac{\rho_s h}{\rho_f})v$. Thus:

$$\mathcal{R}v = \mathcal{P}\big(\mu + \frac{\rho_s h}{\rho_f}\big)v,$$

and therefore, the traces on Γ satisfy:

$$\mathcal{M}_{\mathcal{A}}v = \mathcal{S}\big(\mu + \frac{\rho_s h}{\rho_f}\big)v = \big(\mu + \frac{\rho_s h}{\rho_f}\big)\mathcal{S}v.$$

Since $\mathcal{M}_A v = \mu v$ we finally get

$$\mu v = \big(\mu + \frac{\rho_s h}{\rho_f}\big)\mathcal{S}v.$$

Therefore, v is also an eigenvector for $\mathcal{S}$, and the corresponding eigenvalue λ satisfies:

$$\lambda = \frac{\mu}{\mu + \dfrac{\rho_s h}{\rho_f}}. \tag{5.149}$$

Thus, we have shown that the eigenvalues λ_i of $\mathcal{S}$ can be expressed using the eigenvalues μ_i of $\mathcal{M}_{\mathcal{A}}$ as

$$\lambda_i = \frac{\mu_i}{\mu_i + \dfrac{\rho_s h}{\rho_f}}, \quad i = 1, 2, ... \tag{5.150}$$

We now use this information to study the right hand-side of equation (5.147). Since $\mathcal{S}$ is compact, we know that there exists an orthonormal basis of $L^2(\Gamma)$ composed of the eigenvectors $\{z_j\}$ of $\mathcal{S}$. We thus expand the solution η_r, and the external pressure data p_{ext} and p^0 in this basis:

$$\eta_r^n = \sum_j (\eta_r^n)_j z_j, \quad p_{ext}^n = \sum_j (p_{ext}^n)_j z_j, \quad p_0 = \sum_j (p_0)_j z_j.$$

Then, from (5.147), for each j, the Fourier coefficients satisfy the following equation:

$$\begin{aligned}\rho_s h\frac{(\eta_r^{n+1})_j - 2(\eta_r^n)_j + (\eta_r^{n-1})_j}{\triangle t^2} + \mathcal{L}(\theta(\eta_r^{n+1})_j + (1-2\theta)(\eta_r^n)_j + \theta(\eta_r^{n-1})_j) \\ = \beta((p_{ext}^{n+1})_j - \mathcal{S}(\beta(p^n))_j).\end{aligned} \tag{5.151}$$

The right-hand side of this equation is equal to

$$\beta((p_{ext}^{n+1})_j - \mathcal{S}(\beta(p^n))_j) =$$

$$\beta(p_{ext}^{n+1})_j + \textstyle\sum_{i=1}^{n}(-1)^i\beta^{i+1}\lambda_j^i(p_{ext}^{n+1-i})_j + (-1)^{n+1}\beta^{n+2}\lambda_j^{n+1}(p_0)_j.$$

As $n \to \infty$, the series that defines the right hand-side converges if

$$|\beta\lambda_j| < 1.$$

From (5.150) we see that all λ_j are strictly less than one, which implies that the right-hand side converges if

$$0 \leq \beta \leq 1. \tag{5.152}$$

We have shown the following result:

Proposition 5.3.2. *Provided that $0 \leq \beta \leq 1$, the kinematically coupled β-scheme is unconditionally stable for any choice of the time step Δt, irrespectively of the value of the ratio $\rho_s h/\rho_f > 0$.*

We conclude this section by emphasizing that there is no "added mass effect" exhibited in the kinematically coupled β scheme. This is obvious from the implicit nature of the equation (5.145), which we can write, with a slight abuse of notation, as:

$$\rho_s h\frac{\partial^2\eta_r^{n+1}}{\partial t^2} + \mathcal{L}\eta_r^{n+1} = \beta(p_{ext}^{n+1} - \mathcal{S}(\beta p^n)). \tag{5.153}$$

Indeed, we recall that classical loosely coupled partitioned schemes solve the FSI problem (5.127)-(5.129) by solving the fluid sub-problem (5.127) with Dirichlet boundary data for the fluid velocity on Γ, given in terms of the structure velocity $\partial\eta_r/\partial t$ calculated from the previous time step. Then, the fluid stress calculated in problem (5.127), is used to load the structure in sub-problem (5.128). Using similar ideas as already presented in this manuscript, it was shown in [22] that this kind of partitioned approach leads to solving the problem for η_r of the form

$$\rho_s h\frac{\partial^2\eta_r}{\partial t^2} + \mathcal{L}\eta_r = p|_\Gamma, \tag{5.154}$$

where

$$p|_\Gamma = p_{ext} - \rho_f \mathcal{M}_A \frac{\partial^2\eta}{\partial t^2}. \tag{5.155}$$

Here p_{ext} comes from the "external" pressure data ($p_{in/out}$), and $\mathcal{M}_A$ is the "added mass operator". The **added mass operator** is defined to be the trace of the pressure solution on Γ of the corresponding fluid sub-problem (5.127) written in terms of pressure (with the homogeneous inlet/outlet data). Namely, $\mathcal{M}_A : H^{-1/2}(\Gamma) \to H^{1/2}(\Gamma)$ is the trace of the operator $\mathcal{R}$:

$$\mathcal{M}_A w = \mathcal{R}w|_\Gamma, \tag{5.156}$$

where $\mathcal{R} : H^{-1/2}(\Gamma) \to Q$ associates to each $w \in H^{-1/2}(\Gamma)$ the (pressure) solution of the following problem:

$$\left\{\begin{array}{rcll} -\triangle\mathcal{R}w &=& 0 & \text{in } \Omega, \\ \mathcal{R}w &=& 0 & \text{on } \Gamma_{in/out}, \\ \dfrac{\partial\mathcal{R}w}{\partial\boldsymbol{n}} &=& 0 & \text{on } \Gamma_b, \\ \dfrac{\partial\mathcal{R}w}{\partial\boldsymbol{n}} &=& w & \text{on } \Gamma. \end{array}\right.$$

Here Q is the space defined in (5.139). While w here corresponds to the structure inertia $\partial^2\eta/\partial t^2$, in our kinematically coupled β-scheme w corresponds to the fraction of the fluid stress determined by βp. When $\beta = 0$, which corresponds to the original kinematically coupled scheme, this term is zero. We emphasize again that the structure inertia in the kinematically coupled schemes is taken *implicitly* in the Robin boundary condition, and not explicitely, as in the classical loosely coupled schemes.

With the added mass operator, the problem for the structure (5.154) can now be written as

$$(\rho_s h + \rho_f \mathcal{M}_A)\frac{\partial^2 \eta_r}{\partial t^2} + \mathcal{L}\eta_r = p_{ext}. \tag{5.157}$$

Since in classical loosely coupled partitioned schemes, the pressure is calculated in the fluid sub-problem using the structure velocity from the previous time step, this implies that, with a slight abuse of notation, (5.157) can be written as

$$\rho_s h\frac{\partial^2 \eta_r^{n+1}}{\partial t^2} + \rho_f \mathcal{M}_A\frac{\partial^2 \eta_r^{n}}{\partial t^2} + \mathcal{L}\eta_r^n = p_{ext}. \tag{5.158}$$

More precisely, equation (5.159) means

$$\rho_s h\frac{\eta_r^{n+1} - 2\eta_r^n + \eta_r^{n-1}}{(\Delta t)^2} + \rho_f \mathcal{M}_A\frac{\eta_r^{n} - 2\eta_r^{n-1} + \eta_r^{n-2}}{(\Delta t)^2} + \mathcal{L}\eta_r^n = p_{ext}. \tag{5.159}$$

It was shown in [22] that the scheme is unconditionally unstable if

$$\frac{\rho_s h}{\rho_f \mu_{max}} < 1, \tag{5.160}$$

where μ_{max} is the maximum eigenvalue of the added mass operator $\mathcal{M}_A$. It was also shown in [22] that the maximum eigenvalue μ_{max} is associated with the aspect ratio of the fluid domain R/L. The smaller that aspect ratio (the more slender the domain), the maximum eigenvalue μ_{max} is larger.

Going back to equation (5.153), one can now see that there is no added mass operator associated with the kinematically coupled β-scheme. The right-hand side of equation (5.153) is an iterative procedure which can be written in terms of the initial pressure and of the external (in/out) pressure data. Thus, of $0 \leq \beta \leq 1$, our scheme is unconditionally stable for all the choices of $\rho_s h$, ρ_f, and domain size.

In the last two Chapters of this thesis we present numerical results of the proposed computational scheme. In Chapter 6 we first study the performance of our scheme on a set of benchmark problems in FSI. In Chapter 7 we simulate a set of FSI problems with physiologically reasonable data and compare our results with measurements. Excellent agreement with the measurements was obtained.

Chapter 6

Numerical results for the FSI solver tested on a benchmark problem

We present four tests that show the behavior of our scheme for FSI problems discussed in Section 5.2 for different parameter values. The first test, presented in Example 1 below, corresponds to the benchmark problem suggested by Formaggia et al. in [41] to study the behavior of FSI scheme for blood flow. The structure model in this case is a linearly viscoelastic string model capturing only radial displacement, with the coefficient that describes bending rigidity given in terms of the shear modulus and Timoshenko correction factor, which is different from the corresponding Koiter shell model coefficient. The viscoelasticity and the Young's modulus in this model are both very small. See, e.g., [21] for the physiological values of these parameters.

In Example 1b we supplemented this model by an equation describing dynamics

of the longitudinal displacement, obtained from the Koiter shell model. The corresponding equation for longitudinal displacement is degenerate, and there are no coupling terms between the radial and longitudinal displacement.

In Example 2 we consider the full Koiter shell model capturing both radial and longitudinal displacement, and the coupling between the two. The coefficients in the model are given by those associated with the derivation of the Koiter shell, see (2.23). The values of Youngs modulus, Poisson ratio, and shell thickness are the same as in Examples 1 and 1b, with the viscoelasticity coefficients small, and related to the one in Example 1.

In Example 3 we consider the full Koiter shell model as in Example 2, but with the viscoelasticity coefficients which are physiologically reasonable, and higher than in the previous examples.

Each of the examples provides new information about the behavior of the solutions and of our numerical scheme. The following values of fluid and structure parameters are used in all the examples listed below:

Parameters	**Values**	**Parameters**	**Values**
Radius R (cm)	0.5	**Length** L (cm)	6
Fluid density ρ_f (g/cm^3)	1	**Dyn. viscosity** μ (poise)	0.035
Wall density ρ_s(g/cm^3)	1.1	**Wall thickness** h_s (cm)	0.1
Young's mod. E(dynes/cm^2)	0.75×10^6	**Poisson's ratio** σ	0.5

Table 6.1: Geometry, fluid and structure parameters that are used in all the numerical tests presented in this section.

Parameter β that appears in Step 1 and Step 3 of our numerical scheme can vary

between 0 and 1, where the value of $\beta = 0$ corresponds to the kinematically coupled scheme presented in [46]. We noticed that the accuracy improves as we increase the value of β. Thus, the numerical results in the following examples are given for $\beta = 1$.

6.1 Example 1: The benchmark problem with only radial displacement

We consider the classical test problem proposed by Formaggia et al. in [41]. This problem has been used in several works as a benchmark problem for testing the results of fluid-structure interaction algorithms for blood flow [8, 10, 46, 70, 76]. The structure model for this benchmark problem is of the form

$$\rho_s h \frac{\partial^2 \eta_r}{\partial t^2} - kGh \frac{\partial^2 \eta_r}{\partial z^2} + \frac{Eh}{1-\sigma^2}\frac{\eta_r}{R^2} - \gamma \frac{\partial^3 \eta_r}{\partial z^2 \partial t} = f, \tag{6.1}$$

with absorbing boundary conditions at the inlet and outlet boundaries:

$$\frac{\partial \eta_r}{\partial t} - \sqrt{\frac{kG}{\rho_s}}\frac{\partial \eta_r}{\partial z} = 0 \quad \text{at } z = 0 \tag{6.2}$$

$$\frac{\partial \eta_r}{\partial t} + \sqrt{\frac{kG}{\rho_s}}\frac{\partial \eta_r}{\partial z} = 0 \quad \text{at } z = L. \tag{6.3}$$

Here $G = \frac{E}{2(1+\sigma)}$ is the *shear modulus* and k is the *Timoshenko shear correction factor*. The flow is driven by the time-dependent pressure data (see Figure 6.1):

$$p_{in}(t) = \begin{cases} \frac{p_{max}}{2}\left[1 - \cos\left(\frac{2\pi t}{t_{max}}\right)\right] & \text{if } t \le t_{max} \\ 0 & \text{if } t > t_{max} \end{cases}, \quad p_{out}(t) = 0 \ \forall t \in (0, T), \tag{6.4}$$

where $p_{max} = 2 \times 10^4$ (dynes/cm^2) and $t_{max} = 0.005$ (s). The values of all the parameters in this model are given in Tables 6.1 and 6.2.

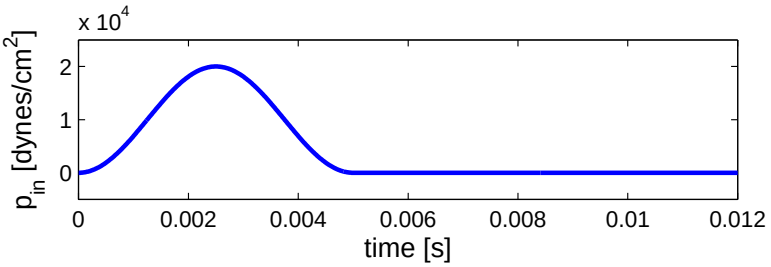

Figure 6.1: Example 1: Inlet pressure used in the benchmark problem

Parameters	**Values**
Shear mod. G(dynes/cm^2)	0.25×10^6
Timoshenko factor k	1
Viscoelasticity γ (poise cm)	0.01

Table 6.2: Example 1: The structure parameters for Example 1 in addition to those listed in Table 6.1. These parameters are not necessarily in the optimal physiological range.

The viscoelasticity and Young's modulus are both very small. For the typical physiological values of these parameters see, e.g., [21]. This means that the arterial wall in this example is rather elastic. The relatively large value of the coefficient in front of the second-order derivative with respect to z (describing bending rigidity), minimizes the oscillations that would normally appear in such structures. See Example 2 for more details.

We implemented this problem in our solver. Since this model captures only radial displacement the solver was modified accordingly. The model equation (6.1) can be recovered from the Koiter shell model (2.22) by setting the following values for the coefficients:

$$\begin{aligned} C_0 &= \tfrac{Eh}{R^2(1-\sigma^2)}, & C_1 &= kGh, & C_2 &= 0, & C_3 &= 0, & C_4 &= 0, \\ D_0 &= 0, & D_1 &= \gamma, & D_2 &= 0, & D_3 &= 0, & D_4 &= 0, \end{aligned}$$

which implies numerical values of the constants given in Table 6.3. Homogeneous

$C_0 = 4 \times 10^5$	$C_1 = 2.5 \times 10^4$	$C_2 = 0$	$C_3 = 0$
$D_0 = 0$	$D_1 = 10^{-2}$	$D_2 = 0$	$D_3 = 0$

Table 6.3: Koiter shell model coefficients for Example 1.

Dirichlet boundary conditions for the structure in Step 3 were replaced with absorbing boundary conditions (6.2)-(6.3). The problem was solved over the time interval $[0, 0.012]$ s. Propagation of the corresponding pressure pulse in 2D is shown in Figure 6.5.

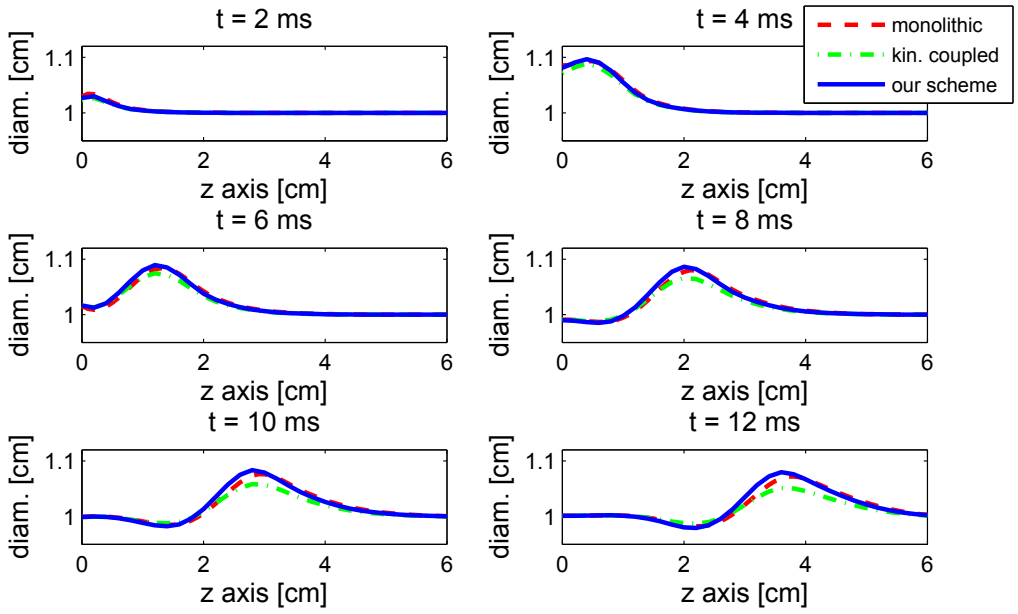

Figure 6.2: Example 1: Diameter of the tube computed with the kinematically coupled scheme with time step $\triangle t = 5 \times 10^{-5}$ (dash-dot line), implicit scheme used by Quaini in [76] with the time step $\triangle t = 10^{-4}$ (dashed line) and our scheme with the time step $\triangle t = 10^{-4}$ (solid line).

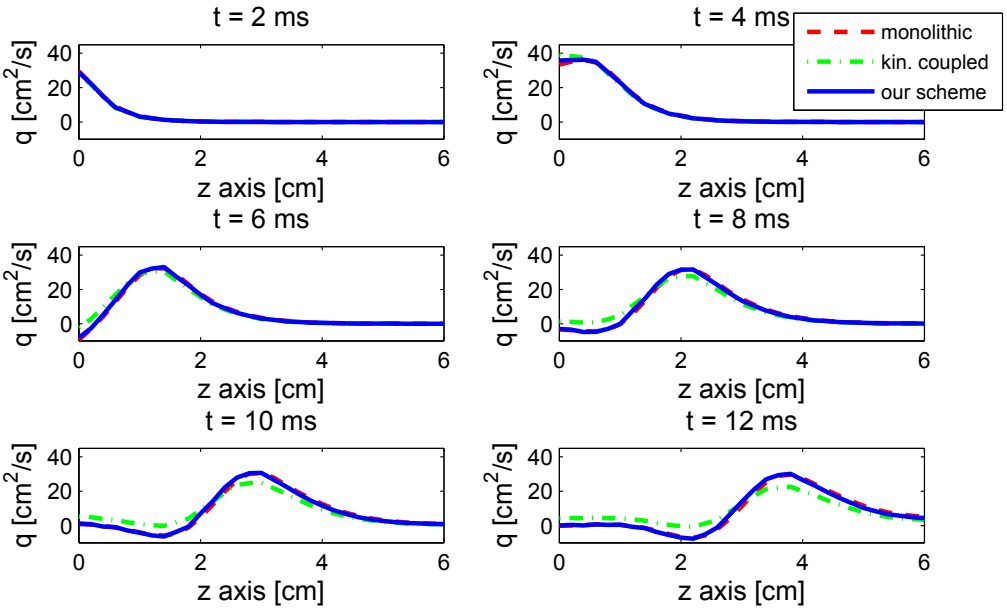

Figure 6.3: Example 1: Flowrate computed with the kinematically coupled scheme with time step $\triangle t = 5 \times 10^{-5}$ (dash-dot line), implicit scheme used by Quaini in [76] with the time step $\triangle t = 10^{-4}$ (dashed line) and our scheme with the time step $\triangle t = 10^{-4}$ (solid line).

The numerical results obtained using our modification of the kinematically (loosely) coupled scheme proposed in this manuscript, were compared with the numerical results obtained using the classical kinematically coupled scheme proposed in [46], and the monolithic scheme proposed in [76]. Figures 6.2, 6.3, and 6.4 show the comparison between tube diameter, flowrate, and mean pressure, respectively, at six different times.

These results were obtained on the same mesh as the one used for the monolithic scheme in [76], containing 31×11 $\mathbb{P}_1$ fluid nodes. More precisely, we used an isoparametric version of the Bercovier-Pironneau element spaces, also known as $\mathbb{P}_1$-iso-$\mathbb{P}_2$

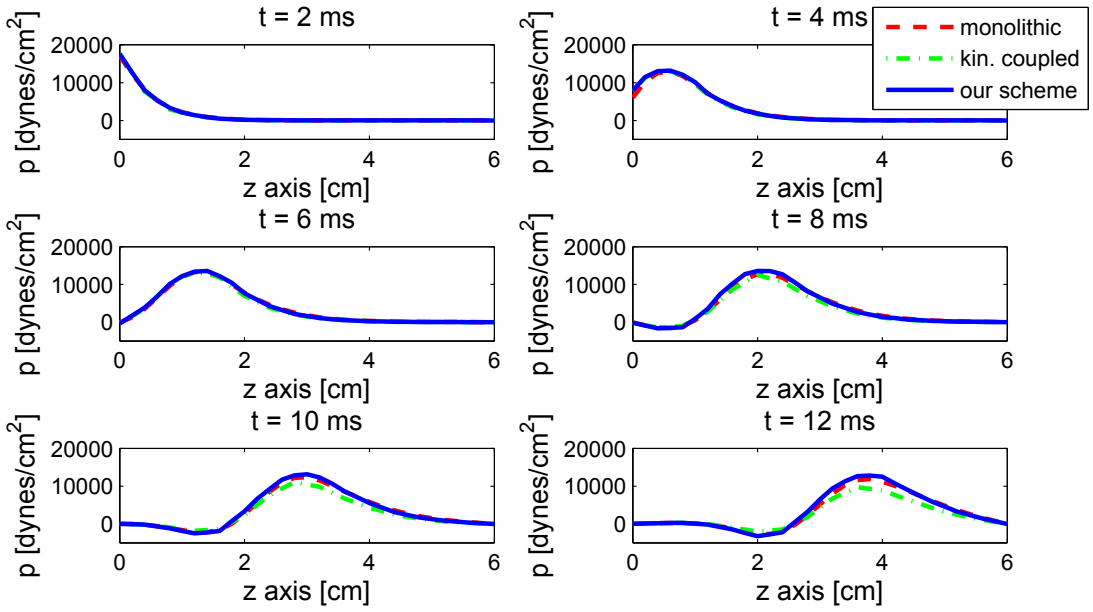

Figure 6.4: Example 1: Mean pressure computed with the kinematically coupled scheme with time step $\triangle t = 5 \times 10^{-5}$ (dash-dot line), implicit scheme used by Quaini in [76] with the time step $\triangle t = 10^{-4}$ (dashed line) and our scheme with the time step $\triangle t = 10^{-4}$ (solid line).

approximation in which a coarse mesh is used for the pressure (mesh size h_p) and a fine mesh for velocity (mesh step $h_v = h_p/2$).

The time step used was $\triangle t = 10^{-4}$ which is the same as the time step used for the monolithic scheme, while the time step used for the kinematically coupled scheme in [46] was $\triangle t = 5 \times 10^{-5}$. It is well-known that splitting schemes require smaller time step due to the splitting error. However, the new splitting proposed in this manuscript allows us to use the same time step as in the monolithic method, obtaining comparable accuracy, as it will be shown next. This is exciting since we obtain the same accuracy while retaining the main benefits of the partitioned

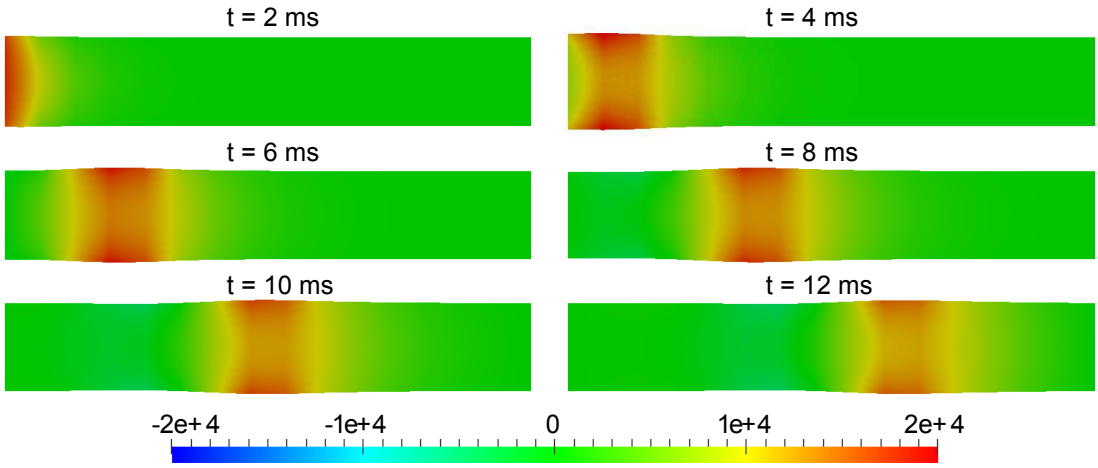

Figure 6.5: Example 1: Propagation of the pressure wave.

schemes, such as modularity, simple implementation, and low computational costs.

$\triangle t$	$\|\|p - p_{ref}\|\|_{L^2}$	L^2 order	$\|\|\boldsymbol{u} - \boldsymbol{u}_{ref}\|\|_{L^2}$	L^2 order	$\|\|\boldsymbol{\eta} - \boldsymbol{\eta}_{ref}\|\|_{L^2}$	L^2 order
10^{-4}	4.01e + 03	-	5.97	-	0.003	-
	(5.65e + 04)	-	(136.32)	-	(0.0446)	-
5×10^{-5}	1.57e + 03	1.35	4.05	0.56	0.0014	1.1
	(3.36e + 04)	(0.75)	(77.91)	(0.80)	(0.0264)	(0.75)
10^{-5}	296.36	1.04	1.0	0.87	3.17e − 04	0.92
	(7.27e + 03)	(0.95)	(16.27)	(0.97)	(0.00576)	(0.95)
5×10^{-6}	134.33	1.14	0.46	1.12	1.45e − 04	1.13
	(3.3e + 03)	(1.14)	(7.36)	(1.14)	(0.0026)	(1.14)

Table 6.4: Example 1: Convergence in time calculated at $t = 10$ ms. The numbers in the parenthesis show the convergence rate for the kinematically coupled scheme presented in [46].

The kinematically coupled scheme was shown numerically to be first-order accurate in time and second order accurate in space [46]. Due to the novel splitting our scheme has an improved consistency over the classical kinematically coupled scheme. Indeed, here we show that this is the case by studying time-convergence

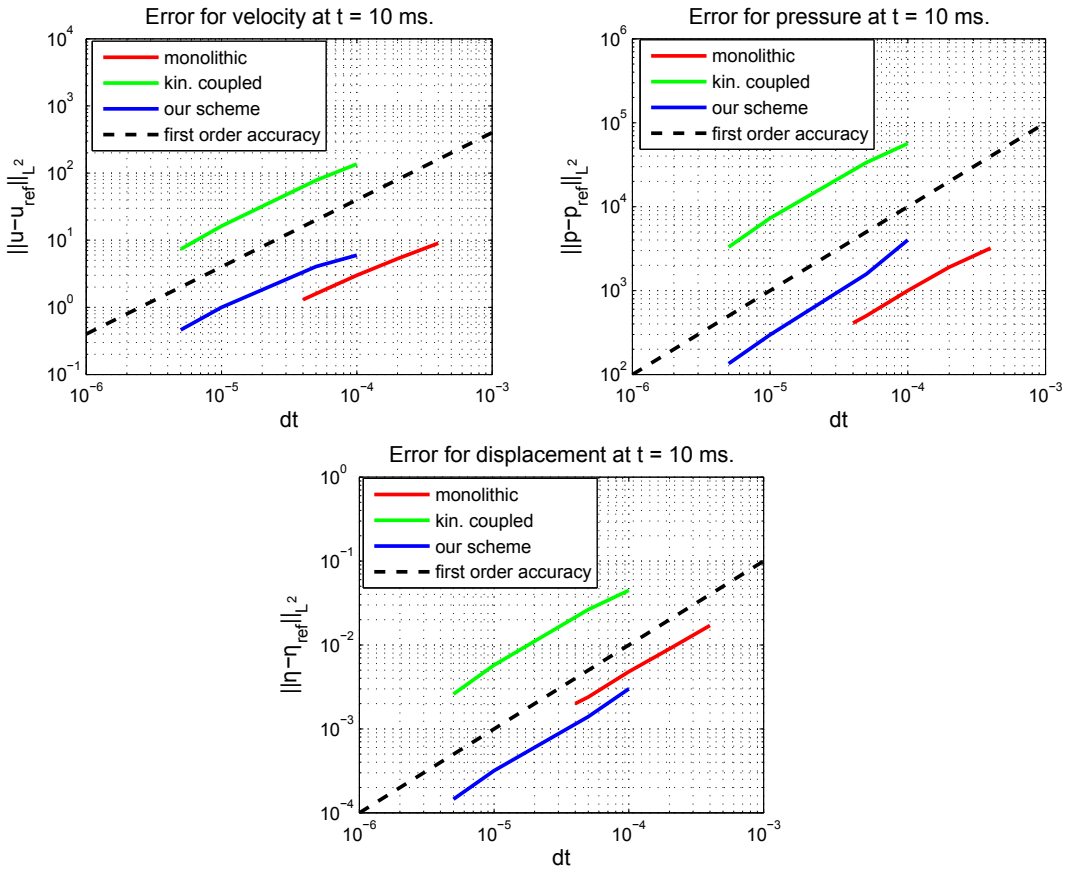

Figure 6.6: Example 1: Figures show relative errors compared with the kinematically coupled scheme which is first-order accurate in time. Top left: Relative error for fluid velocity at t=10 ms. Top right: Relative error for fluid pressure at t=10 ms. Bottom: Relative error for displacement at t=10 ms.

of our scheme. Figure 6.6 shows a comparison between the time convergence of our scheme, the kinematically coupled scheme, and the monolithic scheme used in [76]. The reference solution was defined to be the one obtained with $\triangle t = 10^{-6}$. We calculated the absolute L^2 error for the velocity, pressure and displacement between the reference solution and the solutions obtained using $\triangle t = 5 \times 10^{-6}, 10^{-5},\ 5 \times 10^{-5}$ and 10^{-4}. Figure 6.6 shows first-order in time convergence for the velocity, pressure,

and displacement obtained by the kinematically coupled scheme, monolithic scheme, and our scheme. Due to the improved consistency, the error of our method is noticeably smaller than the error obtained using the kinematically coupled scheme, and is comparable to the error obtained by the monolithic scheme.

6.1.1 Homogeneous Dirichlet vs. absorbing boundary conditions

We give a short remark related to the impact of the homogeneous Dirichlet vs. absorbing boundary conditions. Although absorbing boundary conditions for the structure are more realistic in the blood flow application, they will only impact the solution near the boundary, except when reflected waves form in which case the influence of the boundary conditions is felt everywhere in the domain. It was rigorously proved in [88] that in the case of homogeneous Dirichlet inlet/outlet structure data $\boldsymbol{\eta} = 0$, a boundary layer forms near the inlet or outlet boundaries of the structure to accommodate the transition from zero displacement to the displacement dictated by the inlet/outlet normal stress flow data. It was proved in [88] that this boundary layer decays exponentially fast away from the inlet/outlet boundaries. Figure 6.7 depicts a comparison between the displacement obtained using absorbing boundary conditions, and the displacement obtained using homogeneous Dirichlet boundary conditions, showing a boundary layer near the inlet boundary where the two solutions differ the most.

It is worth pointing out, however, that absorbing boundary conditions help in

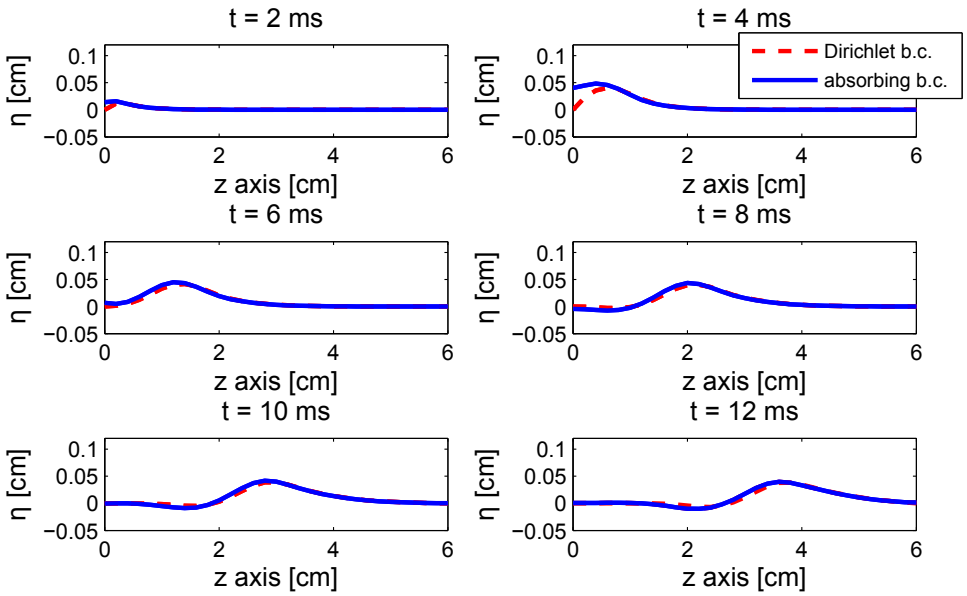

Figure 6.7: Example 1: Displacement of the structure in the case of absorbing boundary conditions (solid line) and homogeneous Dirichlet boundary conditions (dashed line).

reducing reflected waves that will appear when the propagating wave reaches the outlet boundary and reflects back. The "optimum" absorbing boundary conditions would have to be designed on the basis of Riemann Invariants (or characteristic variables) for the hyperbolic problem modeling wave propagation in the structure. Those conditions, however, are not always easy to calculate, and so approximate Riemann Invariant-based absorbing conditions such as (6.2)-(6.3) are used. Figure 6.8 shows the displacement in the case of absorbing boundary conditions (6.2), (6.3), and homogeneous Dirichlet boundary conditions $\boldsymbol{\eta} = 0$ at $t = 100$ ms and $t = 200$ ms. Notice how the two solutions differ everywhere in the domain, and how the solution with absorbing boundary conditions reduces the amplitude and formation

of reflected waves.

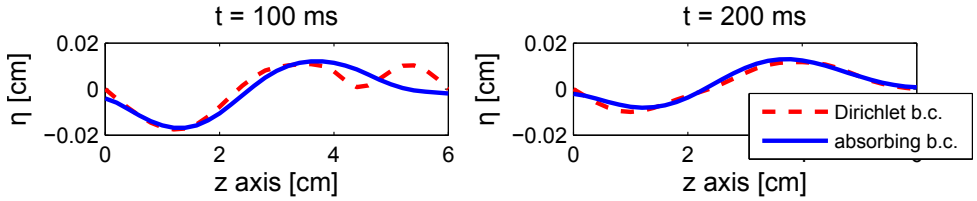

Figure 6.8: Example 1: Displacement of the structure in the case of absorbing boundary conditions (solid line) and homogeneous Dirichlet boundary conditions (dashed line).

We will see in Example 3, below, that for a Koiter shell model with the physiologically relevant coefficients describing the behavior of viscoelastic walls, reflected waves have a much smaller influence on the simulation of the physiologically relevant wave propagation.

6.1.2 Example 1b

This example is an extension of the benchmark problem by Formaggia et al. [41] studied in Example 1. The extension concerns inclusion of the longitudinal displacement in the model described in Example 1.

Namely, here we explore how the Koiter shell model (2.21)-(2.22) looks for the coefficients given by those in Example 1. Namely, the radial displacement satisfies the same model equation as in Formaggia et al. [41], while the longitudinal displacement satisfies equation (2.21) in the Koiter shell model, with the corresponding coefficients in accordance with equation (6.1). More precisely, by comparing equations (2.22) and (6.1) we observe that only the coefficients C_0, C_1 and D_1 are different from zero.

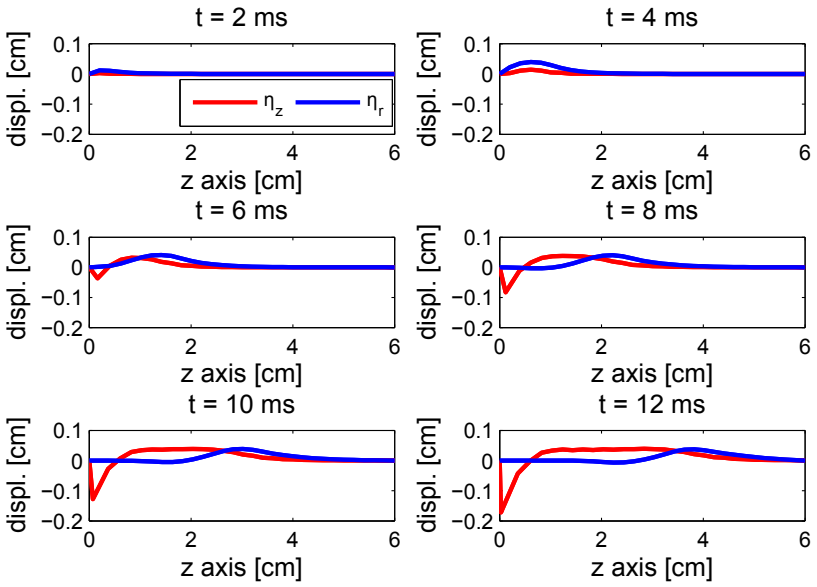

Figure 6.9: Example 1b: Longitudinal displacement (red) and radial displacement (blue) for the Koiter shell model in Example 2 calculated with $\Delta t = 10^{-4}$.

This implies the following Koiter shell model:

$$\rho_s h \frac{\partial^2 \eta_z}{\partial t^2} = f_z, \tag{6.5}$$

$$\rho_s h \frac{\partial^2 \eta_r}{\partial t^2} - kGh \frac{\partial^2 \eta_r}{\partial z^2} + \frac{Eh}{1-\sigma^2} \frac{\eta_r}{R^2} - \gamma \frac{\partial^3 \eta_r}{\partial z^2 \partial t} = f_r. \tag{6.6}$$

Notice that this problem is degenerate in that the operator associated with the static equilibrium problem is no longer strictly elliptic. Nevertheless, we solve the related FSI problem with zero Dirichlet boundary data $\boldsymbol{\eta} = 0$, and flow driven by the time-dependent pressure data (6.4) given in Example 1. The values of the coefficients in the Koiter shell model (6.6)-(6.5) are equal to those in Example 1. Figures 6.9, 6.10, and 6.11 show the displacement, flow rate, and pressure, respectively. It is interesting to notice, as is shown in Figure 6.9, that the magnitude of longitudinal displacement

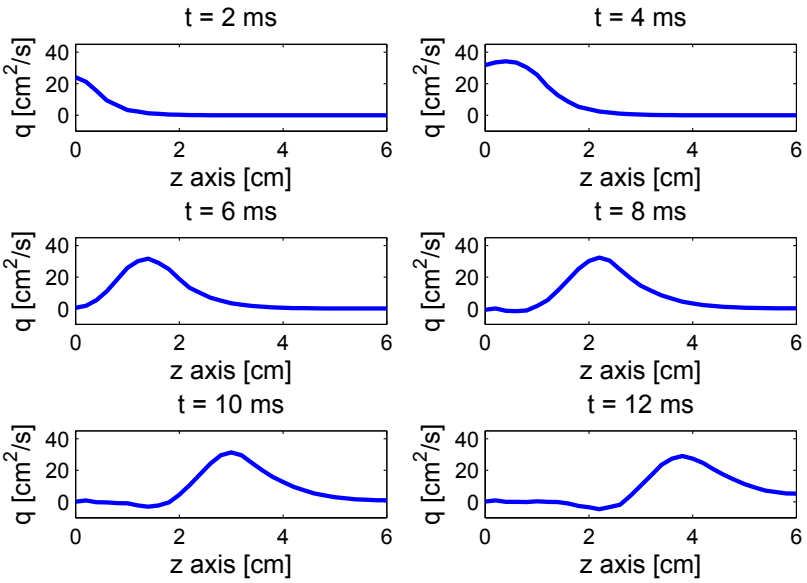

Figure 6.10: Example 1b: Flow rate for the Koiter shell model in Example 1b calculated with $\Delta t = 10^{-4}$.

is the same as the magnitude of radial displacement.

6.2 Example 2

In this test case we consider the Koiter shell model (2.21)-(2.22) with the corresponding coefficients (2.23). The flow and structure parameters are given in Tables 6.1 and 6.5. The model and the coefficients are as follows:

$$\rho_s h \frac{\partial^2 \eta_z}{\partial t^2} - C_2 \frac{\partial \eta_r}{\partial z} - C_3 \frac{\partial^2 \eta_z}{\partial z^2} - D_2 \frac{\partial^2 \eta_r}{\partial t \partial z} - D_3 \frac{\partial^3 \eta_z}{\partial t \partial z^2} = f_z$$
$$\rho_s h \frac{\partial^2 \eta_r}{\partial t^2} + C_0 \eta_r - C_1 \frac{\partial^2 \eta_r}{\partial z^2} + C_2 \frac{\partial \eta_z}{\partial z} + D_0 \frac{\partial \eta_r}{\partial t} - D_1 \frac{\partial^3 \eta_r}{\partial t \partial z^2} + D_2 \frac{\partial^2 \eta_z}{\partial t \partial z} = f_r,$$

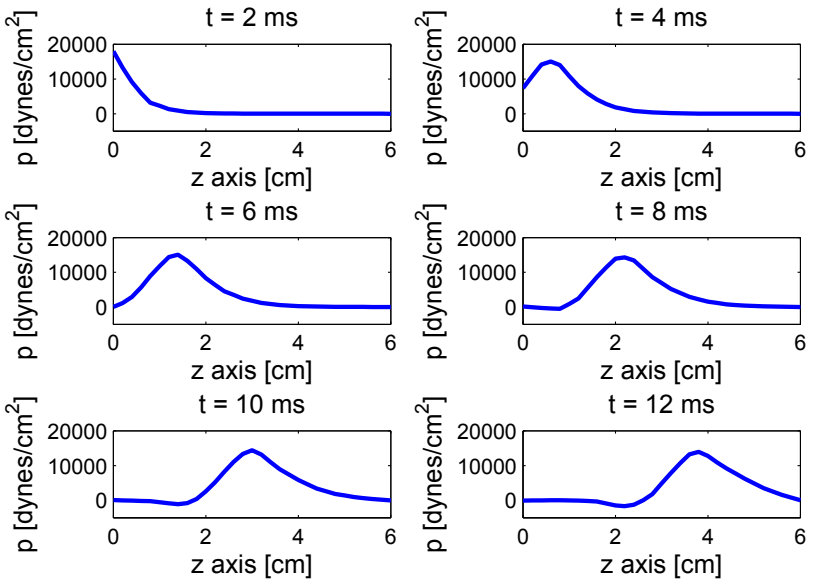

Figure 6.11: Example 1b: Mean pressure for the Koiter shell model in Example 1b calculated with $\Delta t = 10^{-4}$.

with

$$C_0 = \frac{hE}{R^2(1-\sigma^2)}(1+\frac{h^2}{12R^2}), \quad C_1 = \frac{h^3}{6}\frac{E\sigma}{R^2(1-\sigma^2)}, \quad C_2 = \frac{h}{R}\frac{E\sigma}{1-\sigma^2},$$
$$D_0 = \frac{h}{R^2}C_v(1+\frac{h^2}{12R^2}), \quad D_1 = \frac{h^3}{6}\frac{D_v}{R^2}, \quad D_2 = \frac{hD_v}{R},$$

where here we take the value of D_1 to be equal to γ from Examples 1 and 1b, which from the definition of coefficient D_1 above implies $D_v = 6R^2\gamma/h^3$. From here we determine $C_v = D_v/\sigma_v = 2D_v$. The corresponding values of the coefficients are given

Parameters	**Values**
Viscoelast. C_v(poise cm)	30
Viscoelast. D_v(poise cm)	15

Table 6.5: Viscoelasticity parameters for Example 2.

in Table 6.6.

$C_0 = 4.0133 \times 10^5$	$C_1 = 333.3$	$C_2 = 10^5$	$C_3 = 10^5$
$D_0 = 12$	$D_1 = 10^{-2}$	$D_2 = 3$	$D_3 = 3$

Table 6.6: Koiter shell model coefficients for Example 2.

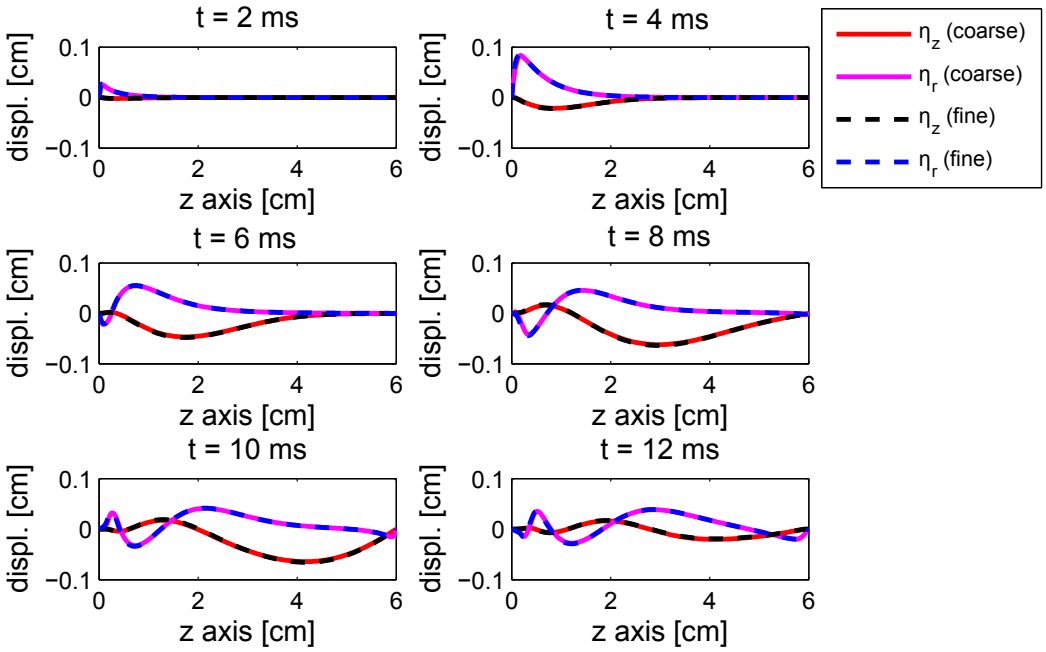

Figure 6.12: Example 2: Longitudinal displacement η_z, and radial displacement η_r calculated on a coarse mesh (solid line) and on a fine mesh (dashed line), obtained with $\triangle t = 10^{-4}$.

This model includes the coupling terms between the longitudinal and radial components of the displacement through $C_2 \neq 0$ and $D_2 \neq 0$, and the leading-order viscoelastic effects in the radial displacement described by $D_0 \neq 0$. Notice a much smaller value for the coefficient C_1 than in Example 1. Also notice the large coefficient C_2 that describes the coupling between the radial and longitudinal components of the displacement. Although the viscoelasticity parameters, or the inlet pressure,

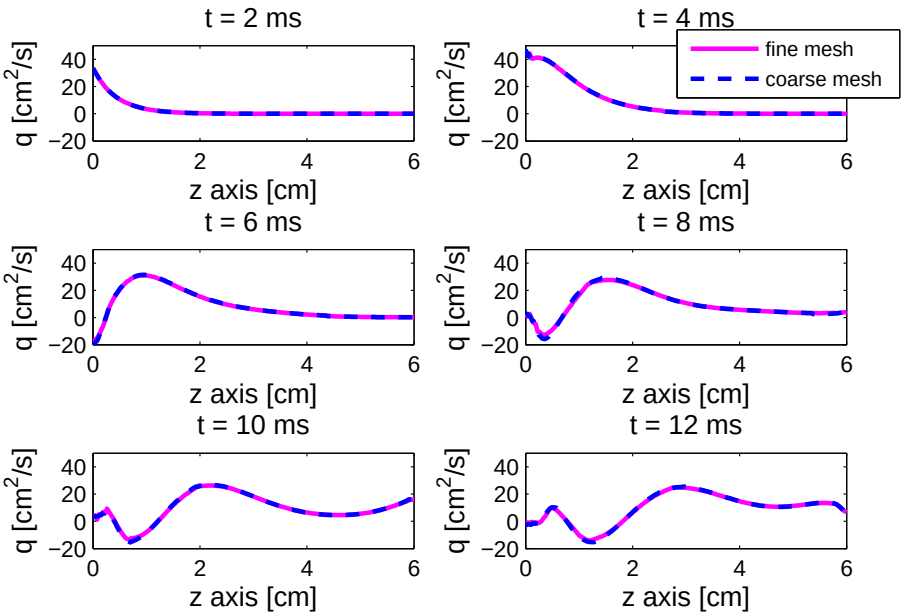

Figure 6.13: Example 2: Flowrate computed on a coarse mesh (solid line), and on a fine mesh (dashed line), obtained with $\triangle t = 10^{-4}$.

are not physiologically reasonable, this example can serve as a good benchmark problem to study the behavior of FSI schemes for blood flow in which both radial and longitudinal displacement of a thin structure are included.

Figure 6.12 shows longitudinal and radial displacement of the structure computed on two different meshes, evaluated at times $t = 2, 4, 6, 8, 10$, and 12 ms. The coarser mesh is twice as fine as the mesh used in Example 1, so that the triangulation of the coarser mesh is $h_p^{coarse} = h_p/2$, $h_v^{coarse} = h_v/2$. The fine mesh in this example is twice as fine as the coarse mesh, namely $h_p^{fine} = h_p^{coarse}/2 = h_p/4$, $h_v^{fine} = h_v^{coarse}/2 = h_v/4$. Note that the longitudinal displacement is of the same order of magnitude as the radial displacement. Figures 6.13 and 6.14 show the corresponding flowrate and mean

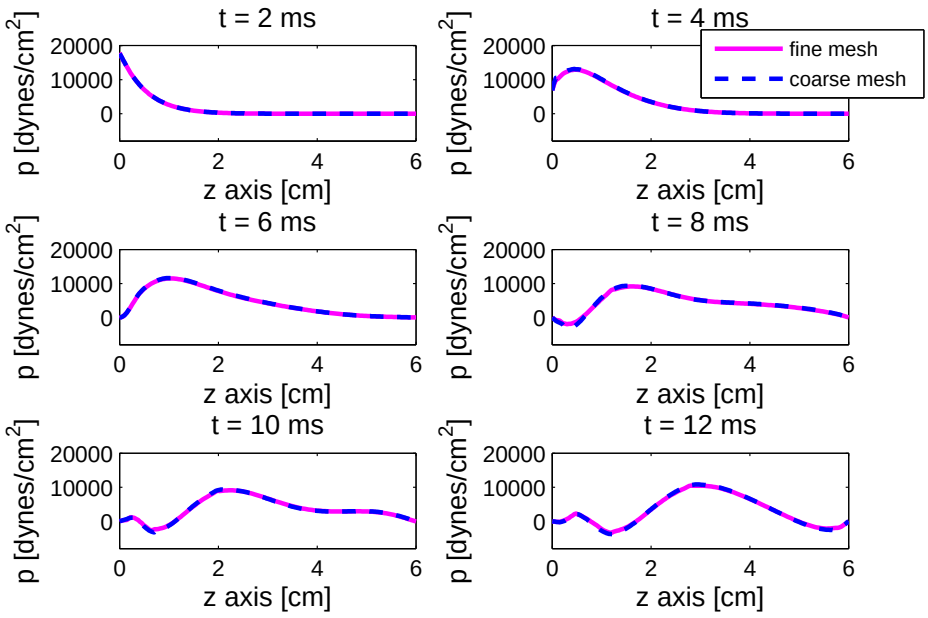

Figure 6.14: Example 2: Mean pressure computed on a coarse mesh (solid line), and on a fine mesh (dashed line), obtained with $\triangle t = 10^{-4}$.

pressure. The appearance of oscillations near the inlet is physical, and is associated with a very small value of the coefficient C_1 when compared to Example 1. An increase in the value of visoelasticity parameters, examined in the next example (physiologically reasonable), dampens the oscillations observed in this example.

To study convergence in time we define the reference solution to be the one obtained with $\triangle t = 10^{-6}$, and we compute the L^2-norms of the difference in the pressure, velocity and displacement between the reference solution and the solutions obtained with $\triangle t = 10^{-4}, 5 \times 10^{-5}, 10^{-5}$ and 5×10^{-6}. The time convergence is presented in Table 6.7.

$\triangle t$	$\|\|p - p_{ref}\|\|_{L^2}$	L^2 order	$\|\|\boldsymbol{u} - \boldsymbol{u}_{ref}\|\|_{L^2}$	L^2 order	$\|\|\boldsymbol{\eta} - \boldsymbol{\eta}_{ref}\|\|_{L^2}$	L^2 order
10^{-4}	1.75e + 03	-	5.83	-	0.0092	-
5×10^{-5}	739.9	1.24	3.85	0.6	0.0065	0.5
10^{-5}	158.46	0.96	0.88	0.92	0.0022	0.66
5×10^{-6}	72.67	1.12	0.4	1.13	0.0012	0.92

Table 6.7: Example 2: Convergence in time calculated at $t = 8$ ms.

6.3 Example 3

The model problem in this example is the same as in Example 2, except that the viscoelasticity coefficients are obtained from the measurements [3], and are therefore, more physiologically reasonable than those in the previous examples. We again consider the Koiter shell model (2.21)-(2.22) with the corresponding coefficients (2.23), and with the coefficients in front of the 4th and 5th order derivatives $C_4 = D_4 = 0$. The fluid and structure parameter values are those listed in Table 6.1, while the viscoelasticity coefficient C_v was taken from the measurements of the viscoelasticity of dog's aorta [3], and is given by $C_v = 13416.4$. This implies $D_v := \sigma_v C_v = 0.5 C_v$. The viscoelasticity parameters are summarized in Table 6.8. These parameters give

Parameters	**Values**
Viscoelast. C_v(poise cm)	13416.4
Viscoelast. D_v(poise cm)	6708.2

Table 6.8: Viscoelasticity parameters for Example 3.

rise to the values of the coefficients given in Table 6.9.

We impose homogeneous Dirichlet boundary data for the structure, and the same

$C_0 = 4.013 \times 10^5$	$C_1 = 333.3$	$C_2 = 10^5$	$C_3 = 10^5$	$C_4 = 0$
$D_0 = 5384.45$	$D_1 = 4.472$	$D_2 = 1341.6$	$D_3 = 1341.6$	$D_4 = 0$

Table 6.9: Koiter shell model coefficients for Example 3.

inlet/outlet pressure data as in Examples 1 and 2.

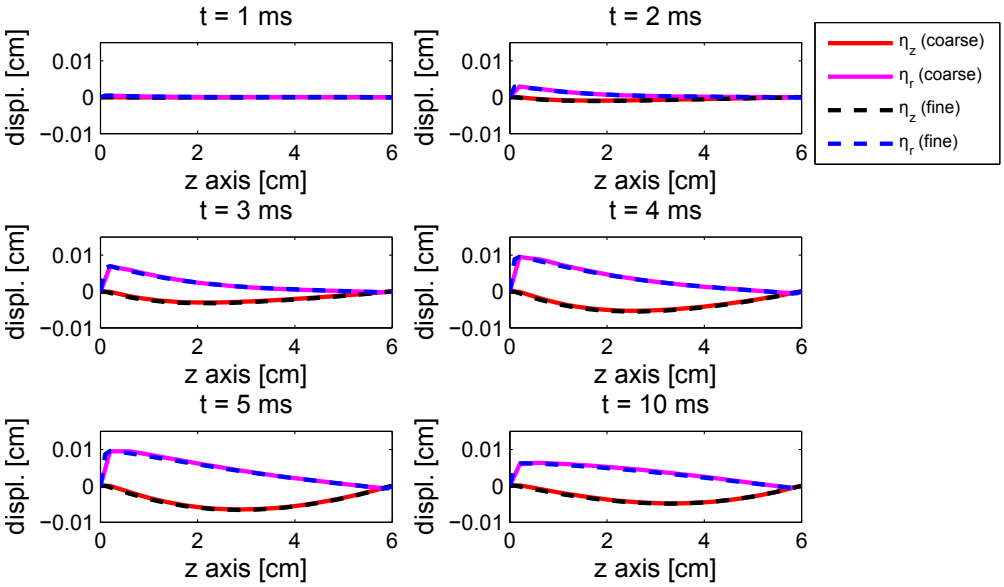

Figure 6.15: Example 3: Longitudinal displacement η_z, and radial displacement η_r, computed on a coarse mesh (solid lone) and on a fine mesh (dashed line).

Figure 6.15 shows displacement of the structure, superimposed over the displacement obtained on a finer mesh. Domain triangulation for the finer mesh is given by $h_p^{fine} = h_p/2$ and $h_v^{fine} = h_v/2$, where the coarser mesh is the same as the mesh in Examples 1 and 2. Results were obtained using the time step $\triangle t = 10^{-5}$. Longitudinal displacement is shown as a solid red line (dashed black line on the finer mesh), while radial displacement as a magenta line (dashed blue line on the finer mesh).

Four remarks are in order. First, notice that the results on the two different

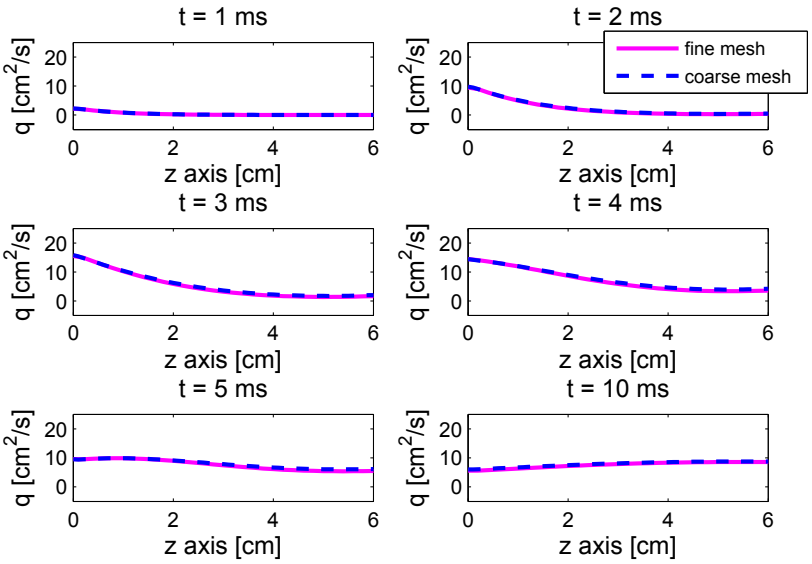

Figure 6.16: Example 3: Flowrate computed on a coarse mesh (solid line) and on a fine mesh (dashed line).

meshes are almost indistinguishable. Secondly, the radial displacement is considerably different from the one in Example 1. This is primarily due to the leading-order viscoelastic effects described by the term multiplying coefficient $D_0 \neq 0$. Thirdly, the viscous effects also diminish the presence of reflected waves. Finally, the longitudinal displacement is of the same order of magnitude due to the strong pressure pulse driving the flow. Negative displacement indicates that the tube has stretched toward the inlet to accommodate the large radial displacement dictated by the pressure pulse.

Figures 6.16 and 6.17 show the flowrate and mean pressure computed on the two different meshes mentioned above. Notice how the pressure wave propagates from left to right, with a strongly decaying amplitude due to the viscous dissipation. Also notice that the results obtained using two different meshes are in an excellent

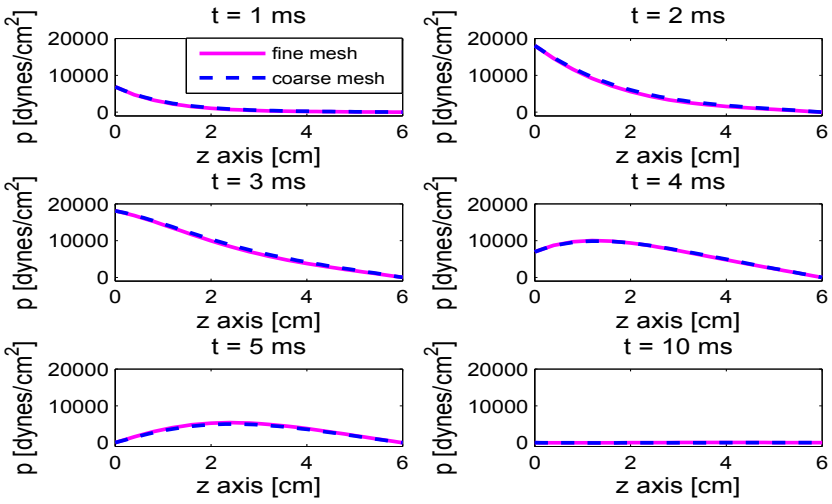

Figure 6.17: Example 3: Mean pressure computed on a coarse mesh (solid line), and on a fine mesh (dashed line).

agreement.

We conclude this section by showing the time-convergence of the scheme. Define the reference solution to be the one obtained with $\triangle t = 10^{-6}$. To investigate the time convergence, we calculate the relative L^2 error for the velocity, pressure and displacement between the reference solution and solutions obtained using $\triangle t = 10^{-4},\ 5 \times 10^{-5},\ 10^{-5}$ and 5×10^{-6}. Figure 6.18 shows the convergence in time. Table 6.10 shows the L^2-error and the convergence rate for the corresponding times steps depicted in Figure 6.18. These results show 1st-order convergence in time of our scheme applied to the problem in Example 3.

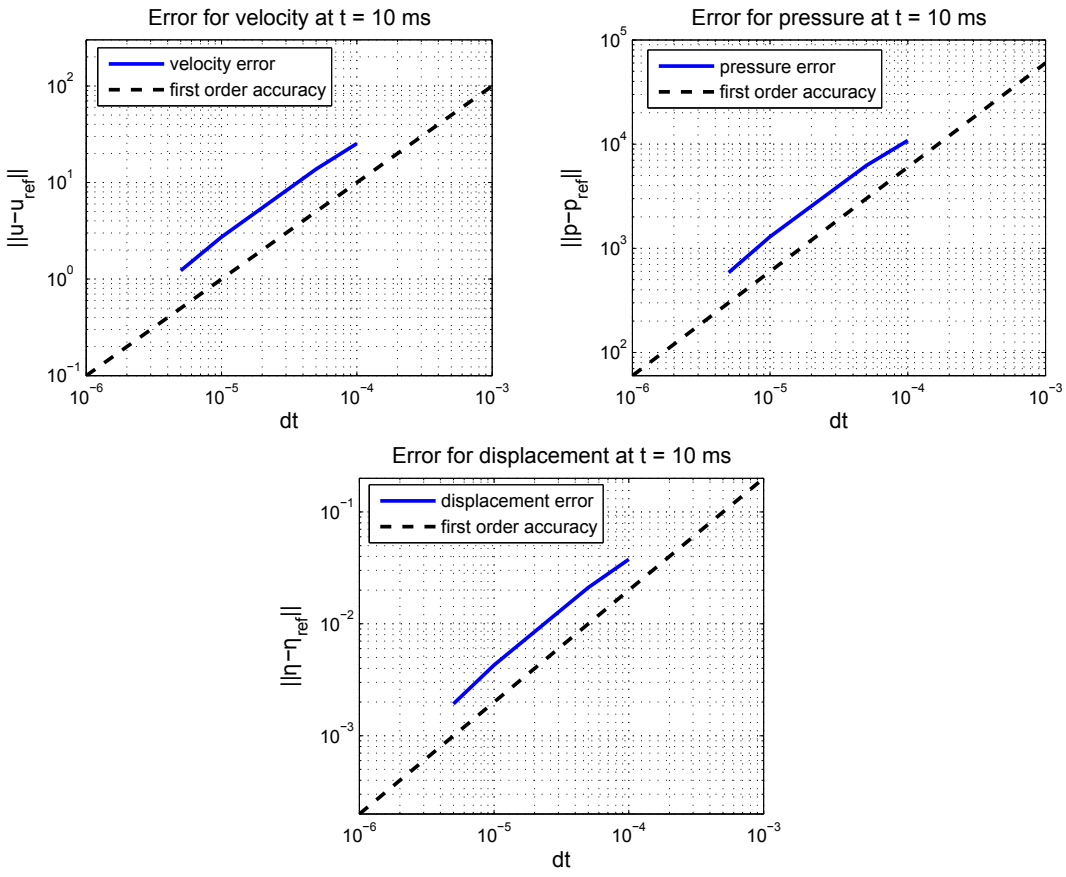

Figure 6.18: Example 3: Figures show first-order accuracy in time. Top left: Relative error for fluid velocity at t=10 ms. Top right: Relative error for fluid pressure at t=10 ms. Bottom: Relative error for displacement at t=10 ms.

$\triangle t$	$\|\|p - p_{ref}\|\|_{L^2}$	L^2 order	$\|\|\boldsymbol{u} - \boldsymbol{u}_{ref}\|\|_{L^2}$	L^2 order	$\|\|\boldsymbol{\eta} - \boldsymbol{\eta}_{ref}\|\|_{L^2}$	L^2 order
10^{-4}	$1.0828e+04$	-	25.35	-	0.0377	-
5×10^{-5}	$6.234e+03$	0.796	13.75	0.88	0.0211	0.839
10^{-5}	$1.29e+03$	0.978	2.73	1.0	0.0043	0.99
5×10^{-6}	584.29	1.1445	1.22	1.16	0.0019	1.15

Table 6.10: Example 3: Convergence in time calculated at $t = 10$ ms.

Chapter 7

Numerical results for blood flow under physiological conditions

In this chapter we show that our computational model gives rise to physiologically reasonable solutions by studying two examples of problems for which there exist data obtained from the measurements of both radial and longitudinal displacement. The first example concerns a healthy common carotid artery (CCA), while the second example concerns an atherosclerotic coronary artery. New results related to the influence of the geometry of stenotic lesion on the magnitude of longitudinal displacement will be shown.

7.1 The common carotid artery (CCA)

The common carotid artery is an artery that supplies the head and neck with oxygenated blood (see Figure 7.1). The artery branches in the neck to form the external

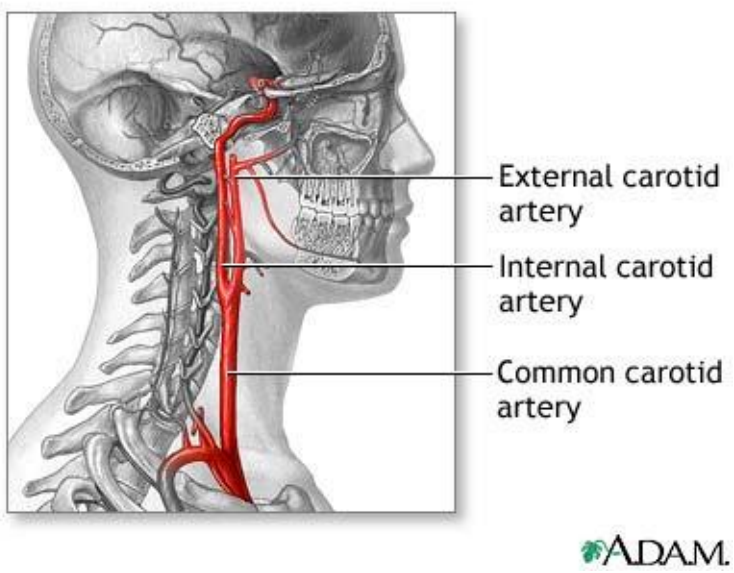

Figure 7.1: Carotid artery [82]

and internal carotid arteries. We simulated blood flow in the left common carotid artery. The choice of parameters in the model will be discussed first, and the pressure data will be presented next. Results of a simulation producing velocity, pressure, radial and longitudinal displacement will be presented. Comparison between calculated and measured velocity, radial and longitudinal displacement, and hysteresis due to viscoelastic arterial wall properties, will be shown.

Parameter Values. Left and right common carotid arteries in human subjects differ significantly in length and in their mode of origin. The study in Ribeiro et

al. [79] measured average length of the left and right CCA in 46 male cadavers. The measured length of the right CCA was 9.6 ± 0.1 cm while the left CCA measured 12.1 ± 0.2 cm. The diameter of CCA slightly differs in males and females, and ranges between 6.5 ± 0.99 cm in males and 5.97 ± 0.9 cm in females [52, 55]. Measurements in Bussy et al. [19] reported wall thickness of 0.0582 ± 0.0139 cm.

Young's modulus of carotid artery increases with age. The study in Urbina et al. [86] considered 516 subjects, aged $25 - 38$ years. Measured Young's modulus was $(2.11 \pm 0.65) \times 10^6$ dynes/cm^2 in males and $(1.83 \pm 0.63) \times 10^6$ dynes/cm^2 in females. On the other hand, Young's modulus of an older group (55 ± 12 years) studied in Mokhtari et al. [66] measured $(3.84 \pm 0.39) \times 10^6$ dynes/cm^2. Blood vessels are essentially incompressible and therefore have the Poisson's ratio of approximately 0.5 [69].

Our choice of parameters lies in the bounds given above, and is summarized in Table 7.1. The viscoelastic constants C_v and D_v that appear in our structure

Parameters	**CCA**
Radius H (cm)	0.3
Length L (cm)	10
Fluid density ρ_f (g/cm^3)	1.055
Fluid viscosity μ (g/(cm s))	0.04
Wall density ρ_s(g/cm^3)	1.055
Wall thickness h (cm)	0.07
Young's mod. E(dynes/cm^2)	2×10^6
Poisson's ratio σ	0.5

Table 7.1: Geometry, fluid and structure parameters for common carotid artery.

equations are equal to

$$C_v := 3 \times 10^4 \text{ dynes/cm}^2 \cdot \text{s}, \quad \text{where } C_v = E_v/(1-\sigma_v^2), \text{ and } \sigma_v = 0.5. \tag{7.1}$$

This choice of viscoelastic parameters is within the range of measured viscous moduli of blood vessels reported in Armentano et al. [2].

Pressure Data. We study blood flow driven by the inlet and outlet pressure data shown in Figure 7.2. These pressure data are obtained from [89]. The shape of

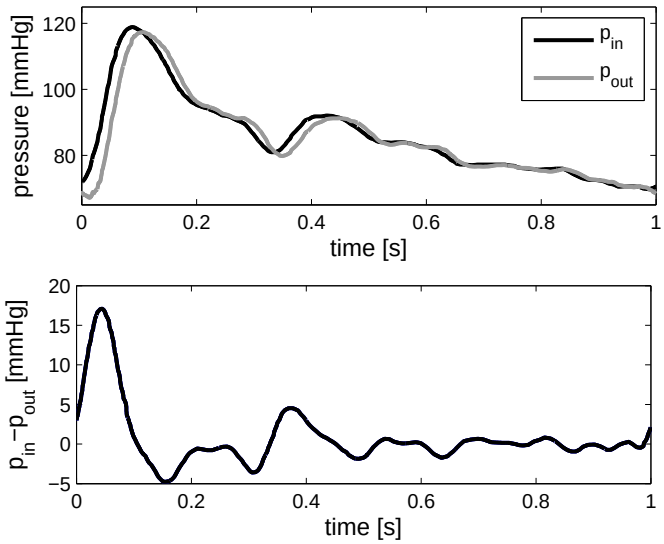

Figure 7.2: Top: inlet and outlet pressure. Bottom: pressure drop.

the pressure wave is the same as in [89] while the pressure drop is scaled by the factor 0.9 to recover physiologically reasonable blood velocity and Reynolds numbers. Namely, several experimental studies have shown that longitudinal velocity in healthy common carotid artery is usually less than 100 cm/s [16, 30, 60, 80] giving rise to the local Reynolds number which is less than 1500. This is smaller than the results in [89] which recover blood flow conditions corresponding to the local Reynold's number over

2400. In our simulations, the maximum axial velocity is around 95 cm/s, which can be seen in Figure 7.4, where longitudinal and radial velocity profiles are shown at the middle of the straight vessel segment. Furthermore, as we shall see below, our computed velocity is in very good agreement with the Doppler velocity data reported by Weinberg et al. [90].

Taking the smaller pressure drop than in [89] is partly responsible for the smaller radial and longitudinal displacements recovered in our simulations when compared to the results in [89], although, as we shall see bellow, they are of the same order of magnitude, and of almost identical morphology. In addition, we will show a very good agreement between our numerical results for the radial and longitudinal displacement and experimental measurements.

Fluid Velocity. Figure 7.4 shows longitudinal (left) and radial (right) velocity profiles at the middle of the vessel, computed using the data listed above, at five different times. The choice of the snapshot times is shown in the Figure 7.3. The velocity pro-

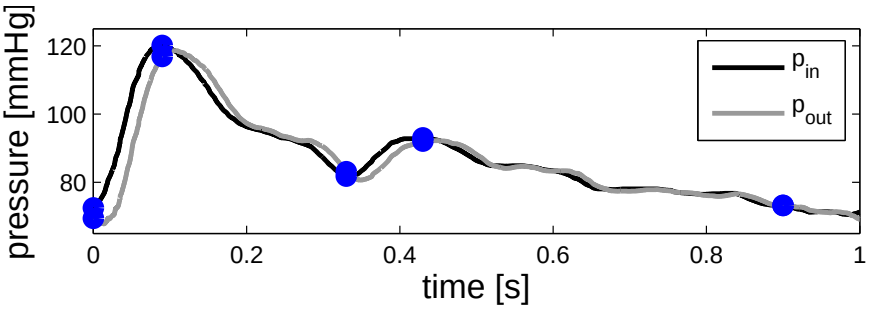

Figure 7.3: Choice of snapshot times and corresponding values of inlet and outlet pressures.

files resemble those experimentally and computationally observed in humans [17, 21].

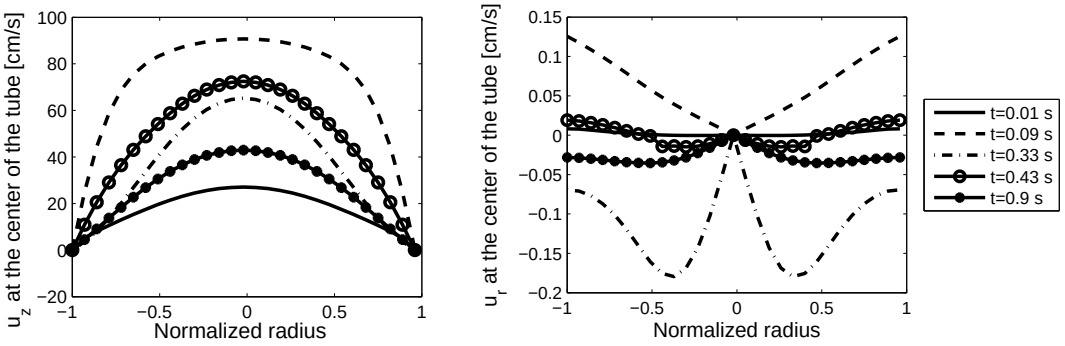

Figure 7.4: Longitudinal (left) and radial (right) velocity profiles over normalized radius at the center of the tube, at five time points.

We compared the computed velocity with Doppler velocity measurements of the left common carotid artery (CCA) reported by Weinberg et al. [90]. Figure 7.5, bottom right, shows the magnitude of velocity at the center of the tube over a cardiac cycle calculated using our computational model. This should be compared with the Doppler velocity graph, shown in Figure 7.5, top right. One can see that the graphs agree both quantitatively and qualitatively. Please notice that we did not have the exact pressure data for this particular measurement. We see that the maximum velocity obtained using our computational model is around 95 cm/s, and the minimum around 30 cm/s. This is in agreement with several results showing experimentally measured CCA velocities [16, 30, 60, 80]. In particular, the measurement shown in Figure 7.5 shows the maximum velocity of 101.1 cm/s, and the minimum velocity of 28.4 cm/s. This shows the difference of only 6% for the maximum, and 3% for the minimum velocity.

Radial and Longitudinal Displacement. Radial wall displacement has been

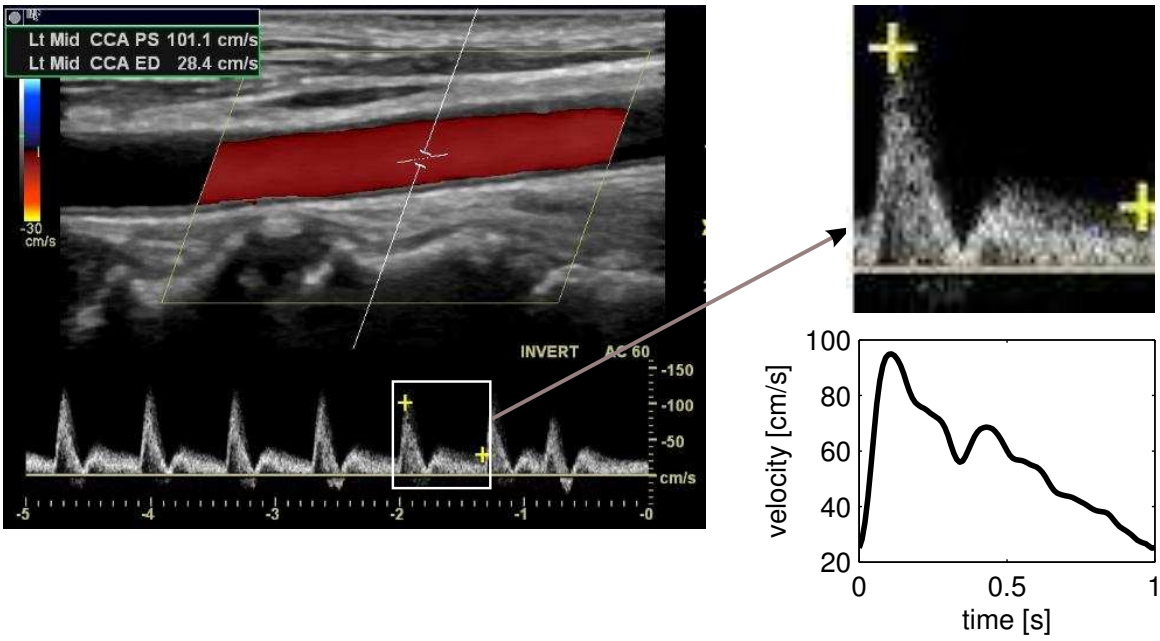

Figure 7.5: Left: Mid CCA velocity Doppler reported in [90]. Right: Comparison with our numerical results.

well examined by many experimental studies [19, 30, 64, 81]. Maximum radial displacement decreases with age, and usually varies between 0.1 mm and 0.38 mm, i.e. between 3% and 13% of the vessel's radius. Indeed, our simulations, shown in Figure 7.6, indicate maximum radial displacement around 6%, which is well within the normal range.

Figure 7.6 also shows longitudinal displacement computed using our thin shell model. Longitudinal displacement varies between -0.1 mm and 0.05 mm, which is in good agreement with experimental studies obtained using B-mode ultrasound speckle tracking method and/or B-mode ultrasound velocity vector imaging, reported in [25, 73, 84, 85]. A comparison with the results in [89] is shown in Figure 7.6. In Figure 7.6 we also show the relationship betweens radial and longitudinal displacement, showing

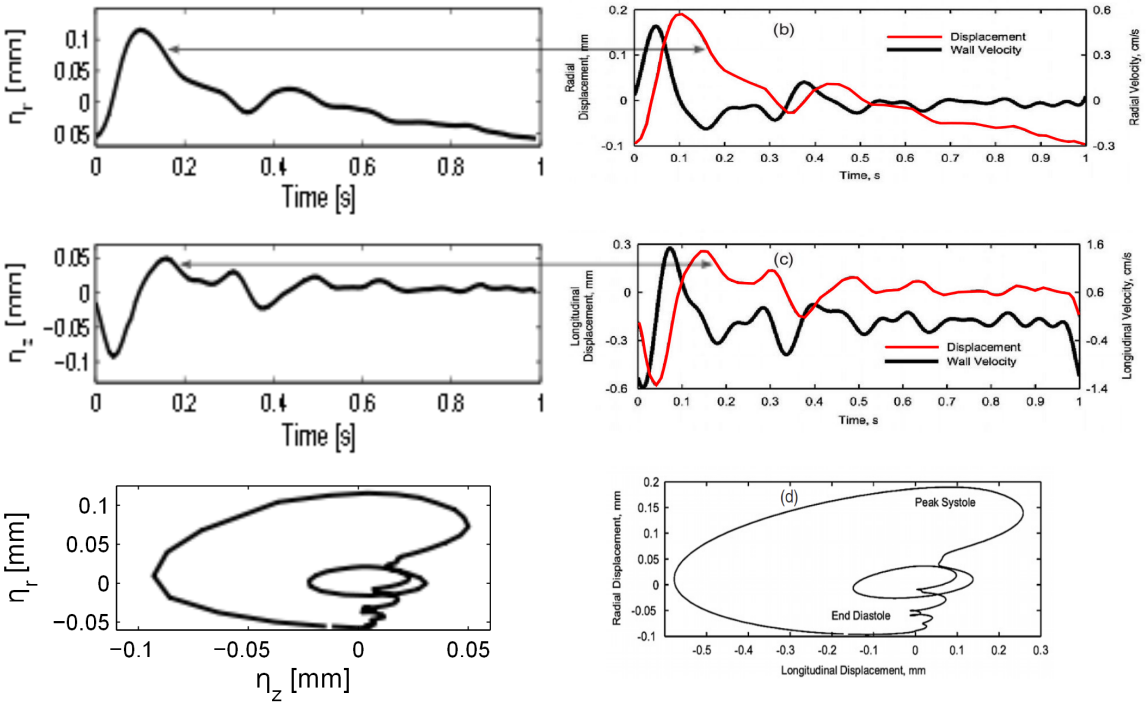

Figure 7.6: Comparison between our simulation (left) and results reported in [89] (right). The figures show longitudinal displacement vs. time (top), radial displacement vs. time (middle), and radial vs. longitudinal displacement (bottom) in one cardiac cycle.

very good agreement.

We also report the most recent results that appeared a few months ago in Atheroslerosis [84], in which longitudinal displacement was measured using B-mode ultrasound velocity vector methods. It was shown that for normal subjects the total longitudinal displacement of the common carotid artery is around 0.100 mm (0.052 mm - 0.302 mm), and the total radial displacement is around 0.3 mm. This is in excellent correlation with our results (see Table 7.2).

CCA variables	**Our num. results**	**Experim. measurem. [84]**
Diameter in systole (mm)	6.12	6.1 (5.4 – 6.7)
Diameter in diastole (mm)	5.94	5.8 (5.0 – 6.0)
Total longit. displ. (mm)	0.15	0.1 (0.052 – 0.302)

Table 7.2: Comparison of numerically obtained diameter change and total longitudinal displacement with experimental measurements reported by Svedlund et al. [84].

We emphasize that the morphology of both radial and longitudinal displacement curves over one cardiac cycle, shown in Figure 7.6, agrees well with the results in [89], and with those in [28]. Figure 7.7 shows the comparison of the numerically computed radial and longitudinal displacement curves at the midpoint of the vessel wall and the measurements reported in Ref [28]. Notice the similarity in the morphology of the curves. The amplitudes of the displacement are different, but of comparable orders of magnitude. We emphasize here that we did not have the pressure or velocity data that correspond to the measurements in [28], therefore, we use these pictures only for qualitative comparison.

Recall that our simulations were obtained for the physiologically relevant data obtained from literature, and with the inlet and outlet pressure data motivated by the studies in [89] enforcing the Reynold's number that is physiologically reasonable for the common carotid artery. Thus, based on the morphology of the displacement curves, and based on the experimental data of total longitudinal displacement and of typical radial displacement in the common carotid artery, we conclude that our simulations provide radial and longitudinal displacements that are in very good agreement with experiments.

Viscoelasticity. Finally, we compare the captured viscoelastic properties. In the

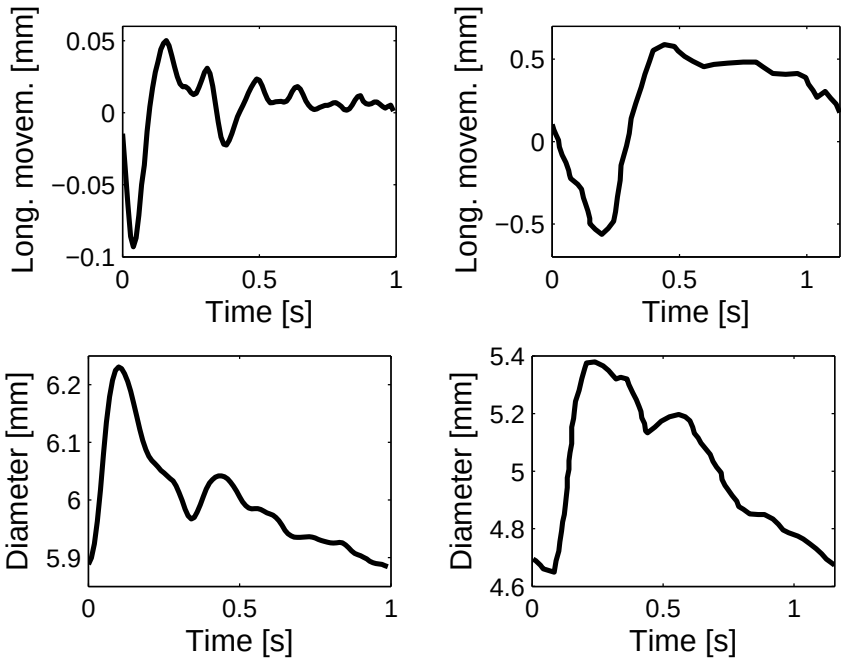

Figure 7.7: Left: numerically calculated radial and longitudinal displacements over one cardiac cycle. Right: experimental measurements in [28]

Kelvin-Voigt model, total stress is linearly proportional to strain and to the time-derivative of strain. As a result, there is a time delay between the pressure and displacement, as shown in Figure 7.8. Figure 7.8 top shows normalized pressure and radial displacement over one cardiac cycle obtained using our computer solutions, while Figure 7.8 bottom shows normalized pressure and radial displacement over one cardiac cycle reported in [89]. The time-delay between peak pressure and peak radial displacement is 0.01 second, or 1% of the cardiac cycle which is consistent with experimental observations.

The viscoelastic effect is also visible in the stress-strain relationship of the arterial wall, which exhibits hysteresis. In our simulations we used the viscosity parameters for the vessel wall, listed in (7.1), which are within the range of parameters reported

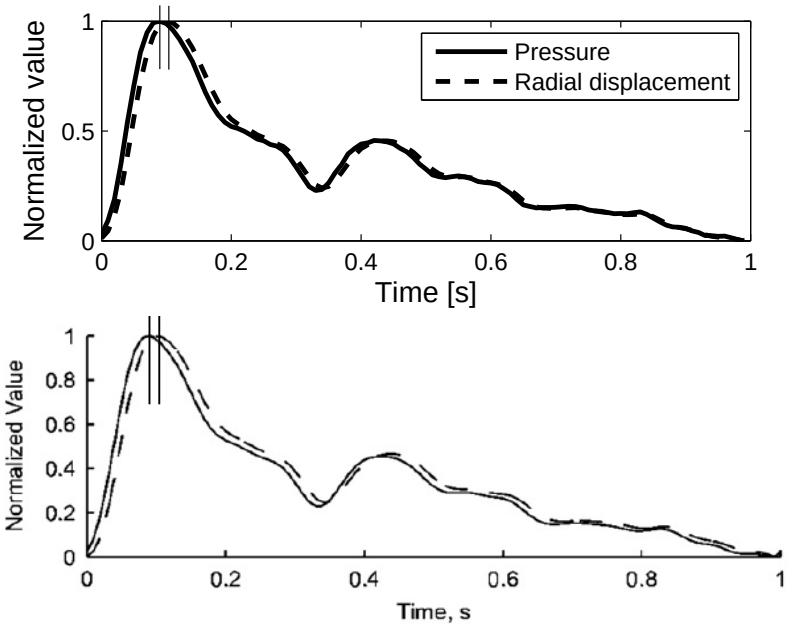

Figure 7.8: Normalized pressure and radial displacement vs. time, taken at the midpoint of a straight vessel segment. Top: our simulation, bottom: results in [89]. The figure shows time delay in the peak displacement due to viscoelasticity of arterial walls.

in Armentano et al. [2]. Figure 7.9 shows hysteresis between the vessel diameter and pressure at the center of the vessel over one cardiac cycle compared with the hysteresis obtained in [89], showing excellent agreement.

To quantify the hysteresis behavior one can calculate the Energy Dissipation Ratio (EDR), which is a measure of the area inside the diameter-pressure loop relative to the measure of areas inside and under the loop (see Figure 7.10). More precisely, if A_1 is the area inside the hysteresis loop, and A_2 is the area below the hysteresis loop, then EDR is defined to be $EDR = A_1/(A_1 + A_2) \times 100\%$. Walls with higher viscoelasticity have larger area inside the loop, resulting in higher EDR. In our simulations EDR is 8.5%. This is comparable to the results in Warriner et al. [89]

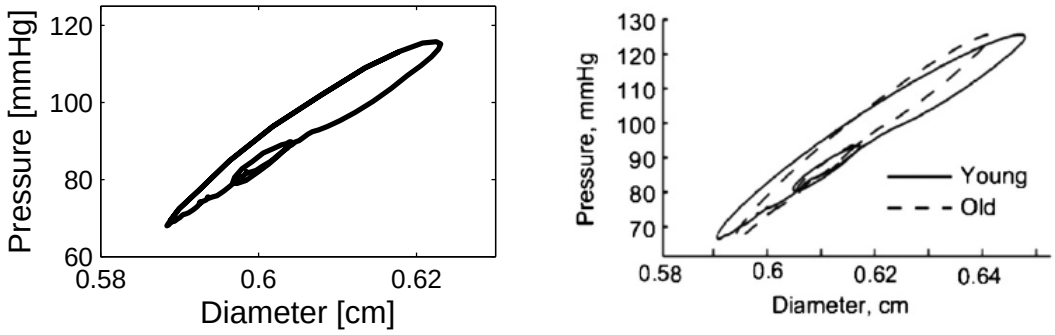

Figure 7.9: Hysteresis between vessel wall diameter and pressure at the center of the vessel, over a cardiac cycle. Left: our simulation, right: results in [89].

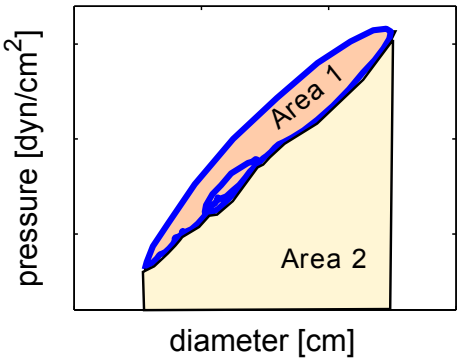

$$\text{EDR} = \frac{\text{Area1}}{\text{Area1}+\text{Area2}} \times 100\%$$

Figure 7.10: Energy dissipation ratio concept.

which show EDR of around 7.8% for a younger subject, and EDR of around 6.4% for an older subject.

7.2 Blood flow through stenosed coronary artery

The vessels that deliver oxygen-rich blood to the heart muscle are known as coronary arteries. Coronary artery disease (CAD), also known as coronary stenosis, is the most common type of heart disease. It is the leading cause of death in the United States

in both men and women. CAD happens when the arteries that supply blood to heart muscle become hardened and narrowed. This is due to the build-up of cholesterol and other material, called plaque, on their inner walls (see Figure 7.11). This build-

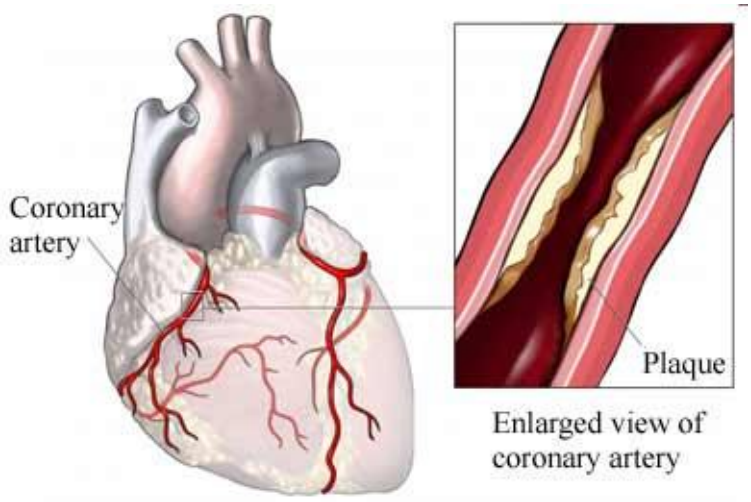

Figure 7.11: Left: Coronary artery. Right: Atherosclerosis. [72]

up is called atherosclerosis. As it grows, less blood can flow through the arteries. As a result, the heart muscle can't get the blood or oxygen it needs. This can lead to chest pain (angina) or a heart attack. Most heart attacks happen when a blood clot suddenly cuts off the hearts' blood supply, causing permanent heart damage.

In this section we simulate blood flow through a stenosed coronary artery with a mild stenosis (60%). We consider three different geometries of stenotic lesions, see Figure 7.12: a symmetric one (type 1), a geometry with a small inflow angle and a sharp outflow angle (type 2), and a geometry with a sharp inflow angle and a smooth outflow angle (type 3). We show that, while radial displacement in all three cases is similar, the longitudinal displacement differs significantly between cases. The role of this mechanism in lesion progression is un-explored. Furthermore, for the symmetric

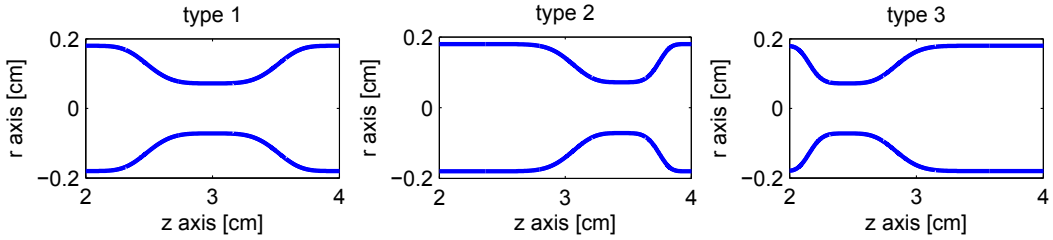

Figure 7.12: Three different plaque geometries used in our simulations.

stenotic lesion we compared the longitudinal displacement at the center of the lesion with that of a healthy coronary artery. We showed that the longitudinal displacement of an atherosclerotic artery is smaller than that of a healthy artery. This was recently experimentally confirmed by Svedlund et al. [85].

Parameter Values. Experimental study in Mokhtari et al. [66] reported Young's modulus of a healthy coronary artery of $3.84 \pm 0.389 \times 10^6 dynes/cm^2$, while in mild stenosis it increased up to $5.02 \pm 0.07 \times 10^6 dynes/cm^2$. In our numerical example, the Young's modulus is a function of position that changes between those two values depending on the geometry. The reference radius for a healthy coronary artery is 0.18 cm, as measured in Dodge et al. [31]. The reference radius in stenotic lesions was calculated based on the following formulas:

$$R(z) = 0.18 - 0.108 * \exp(-10 * (z - L/2)^4) \text{ (type 1)},$$

$$R(z) = 0.18 - 0.108 * \exp(-50 * (z - 2.5 - 0.95 * \exp(-0.5z - 3.4)^2))^4) \text{ (type 2)},$$

$$R(z) = 0.18 - 0.108 * \exp(-50 * (z - 3.4 + 0.95 * \exp(-0.5z - 2.5)^2))^4) \text{ (type 3)}.$$

Similarly, the Young's modulus is given by

$$E(z) = 3.84 \times 10^6 + 1.18 \times 10^6 * \exp(-10 * (z - L/2)^4) \text{ (type 1)},$$

$$E(z) = 3.84 \times 10^6 + 1.18 \times 10^6 * \exp(-50 * (z - 2.5 - 0.95 * \exp(-0.5z - 3.4)^2))^4)$$

(type 2),

$$E(z) = 3.84 \times 10^6 + 1.18 \times 10^6 * \exp(-50 * (z - 3.4 + 0.95 * \exp(-0.5z - 2.5)^2))^4)$$

(type 3).

Since the reference radius and Young's modulus now depend on the position, we used the linearly viscoelastic Koiter membrane model for a tube with variable reference radius given by (2.13)-(2.14) to model the vessel wall. The values of the parameters used in the simulations are given in Table 7.3.

Parameters	**Coronary artery**
Reference radius [31] R (cm)	0.18
Length L (cm)	6
Fluid density ρ_f (g/cm^3)	1.055
Fluid viscosity μ (g/(cm s))	0.04
Wall density ρ_s(g/cm^3)	1.055
Wall thickness [19] h (cm)	0.06
Poisson's ratio σ	0.5
Young's Modulus E $(dyne/cm^2)$	$(3.84 \times 10^6, 5.02 \times 10^6)$

Table 7.3: Geometry, fluid, and structure parameters for coronary artery.

Pressure data. The inlet and outlet pressure were taken from the measurements in Marques et al. [63] where a trans-stenotic pressure gradient in coronary arteries was recorded. The data is shown in Figure 7.13. We used those values of pressure as the inlet and outlet data in our simulations.

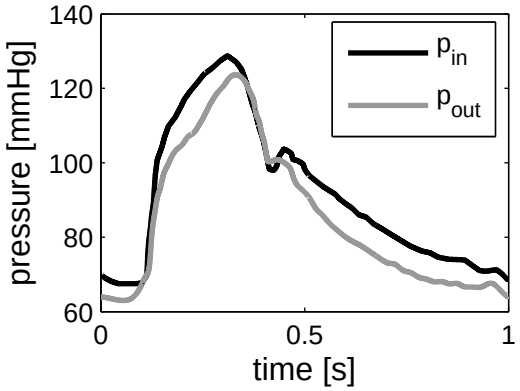

Figure 7.13: Inlet and outlet pressure [63] used in our numerical simulations.

Velocity. We calculated the fluid velocity wave form and streamlines for the 3 types of stenotic lesions. The numerically calculated velocity wave form over one cardiac cycle is shown in Figure 7.14, bottom. Numerically computed peak systolic velocity is around 25 cm/s in the area proximal to stenosis, and 60 cm/s in the stenotic region. This is in very good agreement with measurements reported in Hozumi et al. [49] and in Johnson et al. [51]. Furthermore, the results reported in Marques et al. [63], shown in Figure 7.14, top, report the measured peak systolic velocity in the area proximal to stenosis around 28 cm/s (10% difference with numerical simulation), and in the stenotic lesion around 70 cm/s. (14% difference with numerical simulation).

Figure 7.14 also shows a very good agreement between the morphology of the measured and numerically calculated velocity wave curves over one cardiac cycle. We emphasize here that, unfortunately, no inlet/outlet pressure data was reported in Marques et al. [63] so our simulations were run with the pressure data reported in Figure 7.13.

Notice that our results indicate that the velocity wave form over one cardiac cycle

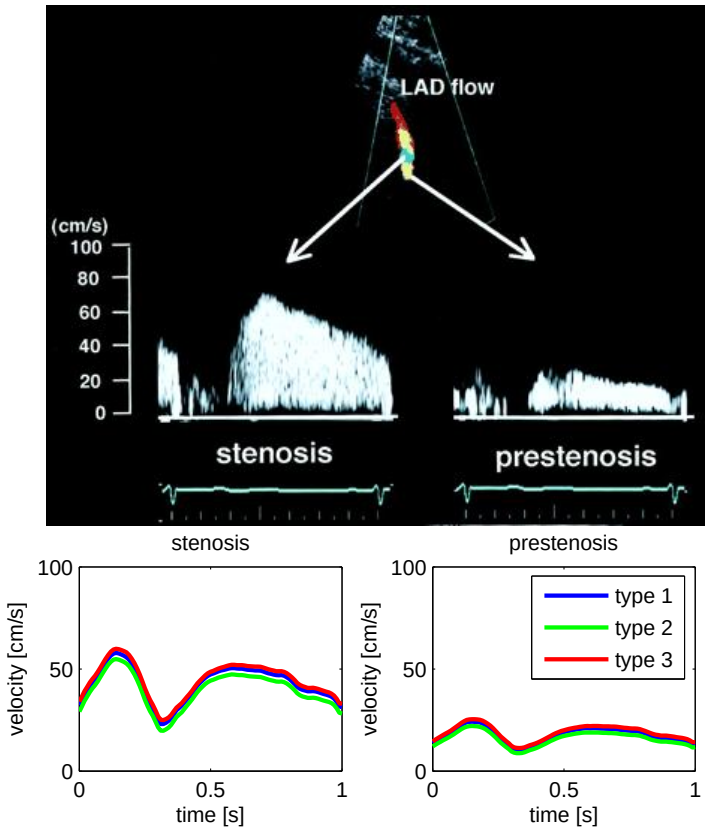

Figure 7.14: Comparison of the velocity wave form between measurements reported in Hozumi et al. [49] (top) and tour numerical simulations (bottom), for the three different geometries of stenotic lesions.

does not change significantly between the three types of stenotic lesions, however, it significantly increases in the stenotic region, as expected.

Figure 7.15 shows the numerically calculated streamlines for the 3 different stenotic geometries, recorded near the peak pressure gradient, at $t = 0.35$ s. One can see that for the type 2 stenotic geometry with a sharp distal (outflow) stenotic angle, the post-stenotic region exhibits a larger and more pronounced recirculation zone and stagnation points, which can be a pre-cursor for a propagation of stenotic lesion.

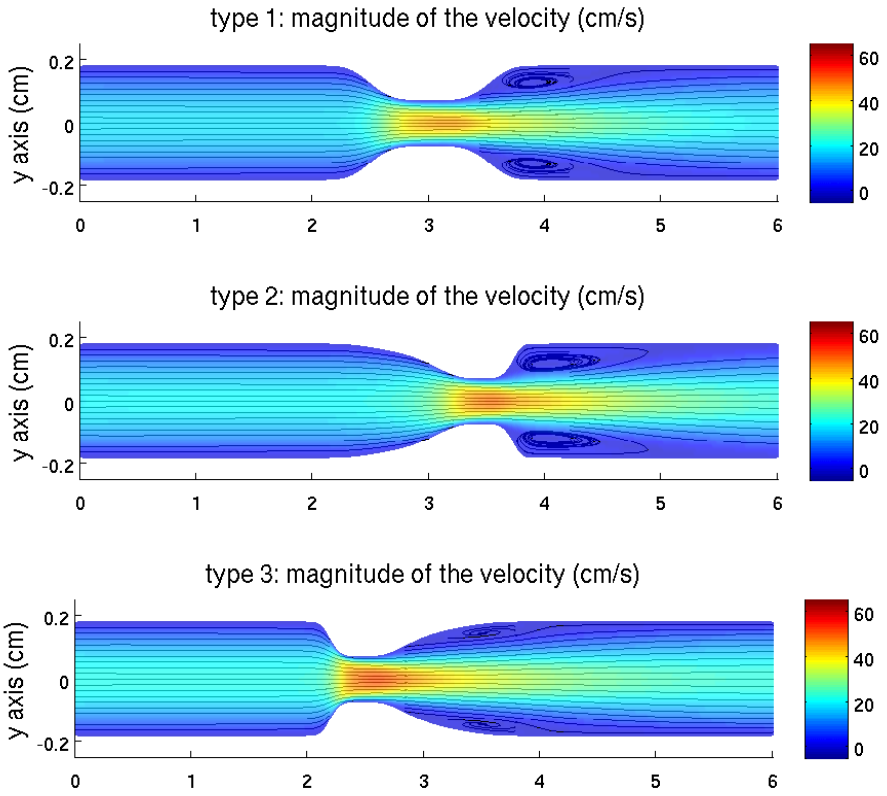

Figure 7.15: Comparison of the velocity in the case of three different stenotic geometries at $t = 0.35$ s.

Radial and Longitudinal Displacement. We simulated radial and longitudinal displacement of the arterial wall proximal to stenosis and in the stenosed area for the three different types of stenotic lesions, see Figure 7.16. We first observe that the radial displacement in the stenosed area is smaller than the radial displacement in the area proximal to the stenotic lesion, as expected. This is due to the local wall stiffening which is associated with atherosclerosis, and is captured in our model by the increase in the Young's modulus at the location of stenosis. Another observation, which is new and interesting, is that radial displacement does not show significant

differences between the three types of the stenotic geometries. The most interesting new observation, however, is that the longitudinal displacement is very different for the three different stenotic geometries. In particular, the plots on the right in Figure 7.16, show that the longitudinal displacement is largest in a coronary artery with the type 3 stenotic lesion. This may indicate that type 3 geometry may be associated with higher incidence of plaque rupture. Further research in this area is needed to make that correlation.

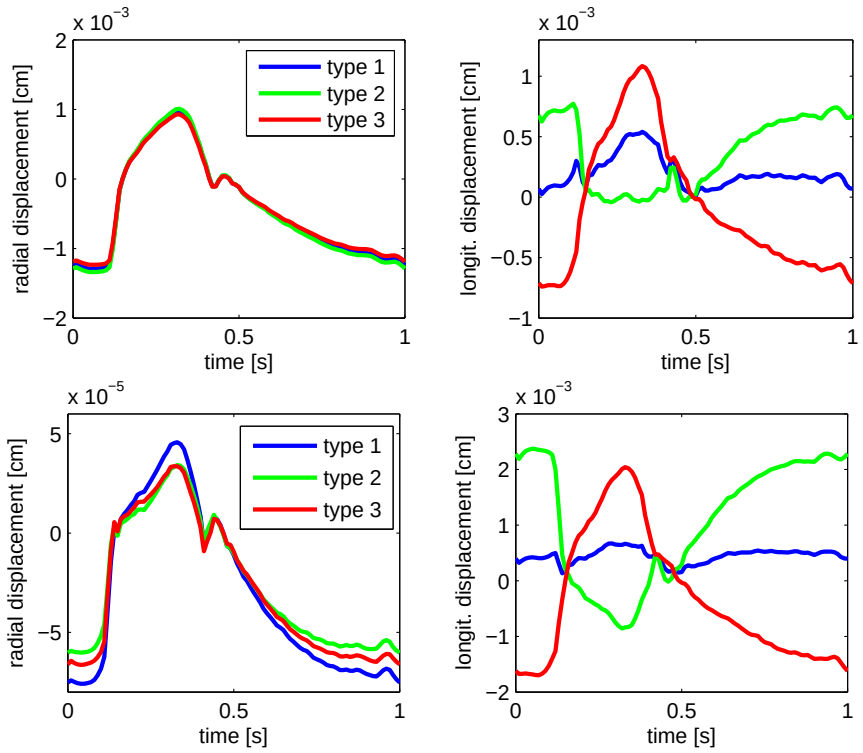

Figure 7.16: Radial and longitudinal displacement of the vessel wall proximal to stenosis (top) and in the stenosed area (bottom).

Finally, we compared the magnitude of longitudinal displacement in a healthy coronary artery with a coronary artery suffering from atherosclerosis (type 1 stenotic

lesion). See Figure 7.17. The main motivation for this comes from a recent work

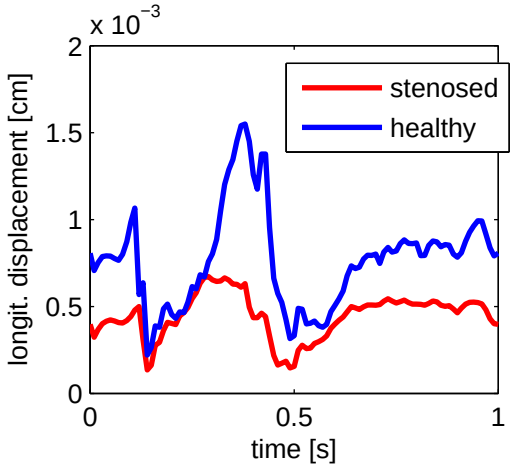

Figure 7.17: Longitudinal displacement in a healthy and stenosed coronary artery.

by Svedlund et al. [85] in which it was demonstrated, using velocity vector imaging (Vevostrain), that plaque burden in atherosclerotic arteries is associated with lower total longitudinal wall motion. It was hypothesized that the main reason for this observation is the reduced longitudinal tensile stress which is typical in local wall thickening due to the higher hemodynamics stress. This phenomenon is captured in our model by the increase in the Young's modulus that affects both the magnitude of radial as well as longitudinal wall motion, which can be seen by the form of the coefficients in the Koiter shell model (2.21), (2.22), in which both the radial and longitudinal stress coefficients depend on the Young's (stiffness) modulus of the structure.

Chapter 8

Discussion

In this thesis we proposed a new thin structure model capturing radial and longitudinal displacement of arterial walls, and have designed a modification of a loosely coupled partitioned scheme (the kinematically coupled scheme [46]) to numerically simulate the resulting fluid-structure interaction problem between blood flow and arterial walls. The proposed arterial wall model is given by the linearly viscoelastic, cylindrical Koiter shell model. The fluid and structure are fully coupled using the kinematic and dynamic coupling conditions. The new loosely coupled scheme, called the kinematically coupled β-scheme, which is first-order accurate in time, and second-order accurate in space, is based on a modified Lie splitting, which was shown to be unconditionally stable. Several test problems were presented showing that the newly proposed numerical scheme has accuracy which is comparable to that of the monolithic scheme by Badia, Quaini, and Quarteroni [10, 76] while retaining the main advantages of loosely coupled partitioned schemes such as modularity, easy

implementation, and low computational costs (no sub-iterations between the fluid and structure sub-solvers are necessary for convergence).

Application of the proposed model and scheme to a set of physiologically relevant problems was investigated. We used the proposed numerical scheme to recreate the radial and longitudional displacement in a healthy common carotid artery that was measured using *in vivo* ultrasound speckle tracking techniques [28, 89]. Our preliminary results show excellent agreement with experimental measurements not only in the radial and longitudinal displacement, but also in the hysteresis behavior due to viscoelasticity of vessel walls.

Furthermore, we modeled blood flow through a coronary artery suffering from atherosclerosis. New results related to the behavior of longitudinal displacement were obtained. More precisely, we showed that, unlike radial displacement, longitudinal displacement in stenotic lesions is highly dependent on the stenotic geometry. In particular, we showed that in type 3 stenotic geometry, the magnitude of longitudinal displacement is largest, which may be associated with higher incidence of plaque rupture. We also showed that longitudinal displacement in atherosclerotic arteries is smaller than in healthy arteries, which is in line with the recent *in vivo* measurements that associate plaque burden with reduced total longitudinal wall displacement [85].

The research presented in this thesis provides a first step in our effort to capture multi-layered structure of arterial walls and their interaction with blood flow. In modeling the intima-media/adventitia complex, the coupling between a thin shell (intima) allowing radial and longitudinal displacement, and a thick structure (media/adventitia) is important. Development of the model presented in this thesis is

crucial for this project. Our preliminary results show that the modified kinematically coupled scheme proposed in this thesis is perfect for the numerical solution of such a set of FSI problems. Research in this direction in under way.

Bibliography

[1] Å.R. Ahlgren, M. Cinthio, S. Steen, H.W. Persson, T. Sjöberg, and K. Lindström. Effects of adrenaline on longitudinal arterial wall movements and resulting intramural shear strain: a first report. *Clin. Physiol. Funct. Imaging*, 29(5):353–359, 2009.

[2] R. Armentano, J.L. Megnien, A. Simon, F. Bellenfant, J. Barra, and J. Levenson. Effects of hypertension on viscoelasticity of carotid and femoral arteries in humans. *Hypertension*, 26(1):48–54, 1995.

[3] R.L. Armentano, J.G. Barra, J. Levenson, A. Simon, and R.H. Pichel. Arterial wall mechanics in conscious dogs: assessment of viscous, inertial, and elastic moduli to characterize aortic wall behavior. *Circ. Res.*, 76(3):468–478, 1995.

[4] M. Astorino, F. Chouly, and M.A. Fernández. An added-mass free semi-implicit coupling scheme for fluid-structure interaction. *Comptes Rendus Mathematique*, 347(1-2):99–104, 2009.

[5] M. Astorino, F. Chouly, and M.A. Fernández Varela. Robin based semi-implicit coupling in fluid-structure interaction: Stability analysis and numerics. *SIAM J. Sci. Comput.*, 31:4041–4065, 2009.

[6] G. Avalos, I. Lasiecka, and R. Triggiani. Higher regularity of a coupled parabolic-hyperbolic fluid-structure interactive system. *Georgian Math. J.*, 15(3):403–437, 2008.

[7] F.P.T. Baaijens. A fictitious domain/mortar element method for fluid-structure interaction. *Int. J. Numer. Meth. Fl.*, 35(7):743–761, 2001.

[8] S. Badia, F. Nobile, and C. Vergara. Fluid-structure partitioned procedures based on Robin transmission conditions. *J. Comput. Phys.*, 227:7027–7051, 2008.

[9] S. Badia, F.. Nobile, and C. Vergara. Robin-robin preconditioned krylov methods for fluid-structure interaction problems. *Comput. Methods Appl. Mech. Eng.*, 198(33-36):2768–2784, 2009.

[10] S. Badia, A. Quaini, and A. Quarteroni. Splitting methods based on algebraic factorization for fluid-structure interaction. *SIAM J. Sci. Comput.*, 30(4):1778–1805, 2008.

[11] R.D. Bauer, R. Busse, A. Schabert, Y. Summa, and E. Wetterer. Separate determination of the pulsatile elastic and viscous forces developed in the arterial wall in vivo. *Pflugers Archiv European Journal of Physiology*, 380(3):221–226, 1979.

[12] Y. Bazilevs, VM Calo, T.J.R. Hughes, and Y. Zhang. Isogeometric fluid-structure interaction: theory, algorithms, and computations. *Computational Mechanics*, 43(1):3–37, 2008.

[13] M. Bercovier and O. Pironneau. Error estimates for finite element method solution of the stokes problem in the primitive variables. *Numerische Mathematik*, 33(2):211–224, 1979.

[14] A. Blouza and H. Le Dret. Existence and uniqueness for the linear koiter model for shells with little regularity. *Quarterly of Applied Mathematics*, 57(2):317–338, 1999.

[15] O. Boiarkine, D. Kuzmin, S. Canic, G. Guidoboni, and A. Mikelic. A positivity-preserving ale finite element scheme for convection-diffusion equations in moving domains. *Journal of Computational Physics*, 230(8):2896–2914, 2011.

[16] J. Bouthier, A. Benetos, A. Simon, J. Levenson, and M. Safar. Pulsed doppler evaluation of diameter, blood velocity and blood flow of common carotid artery in sustained essential hypertension. *Journal of Cardiovascular Pharmacology*, 7:S99, 1985.

[17] B.E. Bulwer and J.M. Rivero. *Echocardiography Pocket Guide: The Transthoracic Examination*. Jones & Bartlett Learning, 2010.

[18] E. Burman and M. A. Fernández. Stabilization of explicit coupling in fluid-structure interaction involving fluid incompressibility. *Comput. Methods Appl. Mech. Eng.*, 198:766–784, 2009.

[19] C. Bussy, P. Boutouyrie, P. Lacolley, P. Challande, and S. Laurent. Intrinsic stiffness of the carotid arterial wall material in essential hypertensives. *Hypertension*, 35(5):1049, 2000.

[20] S. Canic, D. Lamponi, A. Mikelic, and J. Tambaca. Self-consistent effective equations modeling blood flow in medium-to-large compliant arteries. *Multiscale Model. Simul.*, 3(3):559–596, 2005.

[21] S. Canic, J. Tambaca, G. Guidoboni, A. Mikelic, C.J. Hartley, and D. Rosenstrauch. Modeling viscoelastic behavior of arterial walls and their interaction with pulsatile blood flow. *SIAM Journal on Applied Mathematics*, 67(1):164, 2006.

[22] P. Causin, J.F. Gerbeau, and F. Nobile. Added-mass effect in the design of partitioned algorithms for fluid-structure problems. *Comput. Methods Appl. Mech. Eng.*, 194(42-44):4506–4527, 2005.

[23] M. Cervera, R. Codina, and M. Galindo. On the computational efficiency and implementation of block-iterative algorithms for nonlinear coupled problems. *Engineering computations*, 13(6):4–30, 1996.

[24] P.G. Ciarlet. *Mathematical Elasticity: Theory of Shells*, volume 3. North-Holland, Amsterdam, 2000.

[25] M. Cinthio, Å.R. Ahlgren, J. Bergkvist, T. Jansson, H.W. Persson, and K. Lindstrom. Longitudinal movements and resulting shear strain of the arterial wall. *Am. J. Physiol. Heart Circ. Physiol.*, 291(1):H394–H402, 2006.

[26] R.S.C. Cobbold. *Foundations of Biomedical Ultrasound*. Oxford University Press, USA, 2007.

[27] G.H. Cottet, E. Maitre, and T. Milcent. Eulerian formulation and level set models for incompressible fluid-structure interaction. *Esaim. Math. Model. Numer. Anal.*, 42:471–492, 2008.

[28] CREATIS, Biomedical Imaging Laboratory, University of Lyon-INSA. Lyon, France, 2011.

[29] S. Deparis, M.A. Fernández, and L. Formaggia. Acceleration of a fixed point algorithm for fluid-structure interaction using transpiration conditions. *ESAIM: Mathematical Modelling and Numerical Analysis*, 37(04):601–616, 2003.

[30] M.M. Dizaji, M. Maerefat, and S. Rahgozar. Estimation of carotid artery pulse wave velocity by doppler ultrasonography. *The Journal of Tehran University Heart Center*, 4(2), 2009.

[31] J.T. Dodge, B.G. Brown, E.L. Bolson, and H.T. Dodge. Lumen diameter of normal human coronary arteries. influence of age, sex, anatomic variation, and left ventricular hypertrophy or dilation. *Circulation*, 86, 1992.

[32] J. Donea. *Arbitrary Lagrangian-Eulerian Finite Element Methods, in: Computational Methods for Transient Analysis*. North-Holland, Amsterdam, 1983.

[33] F. Duarte, R. Gormaz, and S. Natesan. Arbitrary lagrangian-eulerian method for navier-stokes equations with moving boundaries. *Comput. Methods Appl. Mech. Eng.*, 193(45-47):4819–4836, 2004.

[34] H. Fang, Z. Wang, Z. Lin, and M. Liu. Lattice Boltzmann method for simulating the viscous flow in large distensible blood vessels. *Phys. Rev. E.*, 65(5):051925–1–051925–12, 2002.

[35] L.J. Fauci and R. Dillon. Biofluidmechanics of reproduction. *Annu. Rev. Fluid Mech.*, 38:371–394, 2006.

[36] Z.G. Feng and E.E. Michaelides. The immersed boundary-lattice Boltzmann method for solving fluid-particles interaction problems. *J. Comp. Phys.*, 195(2):602–628, 2004.

[37] M.A. Fernández, J.F. Gerbeau, and C. Grandmont. A projection algorithm for fluid-structure interaction problems with strong added-mass effect. *Comptes Rendus Mathematique*, 342(4):279–284, 2006.

[38] M.Á. Fernández and M. Moubachir. A Newton method using exact jacobians for solving fluid-structure coupling. *Computers & Structures*, 83(2-3):127–142, 2005.

[39] C.A. Figueroa, I.E. Vignon-Clementel, K.E. Jansen, T.J.R. Hughes, and C.A. Taylor. A coupled momentum method for modeling blood flow in three-dimensional deformable arteries. *Comput. Methods Appl. Mech. Eng.*, 195(41-43):5685–5706, 2006.

[40] A.L. Fogelson and R.D. Guy. Platelet-wall interactions in continuum models of platelet thrombosis: formulation and numerical solution. *Math. Med. Biol.*, 21(4):293, 2004.

[41] L. Formaggia, J.F. Gerbeau, F. Nobile, and A. Quarteroni. On the coupling of 3d and 1d navier-stokes equations for flow problems in compliant vessels. *Comput. Methods Appl. Mech. Eng.*, 191(6-7):561–582, 2001.

[42] L. Formaggia and F. Nobile. Stability analysis of second-order time accurate schemes for ale-fem. *Computer methods in applied mechanics and engineering*, 193(39-41):4097–4116, 2004.

[43] L. Formaggia, A. Quarteroni, and A. Veneziani. *Cardiovascular Mathematics, volume 1 of Modeling, Simulation and Applications*. Springer, 2009.

[44] R. Glowinski. *Finite Element Methods for Incompressible Viscous Flow, in: P.G.Ciarlet, J.-L.Lions (Eds), Handbook of Numerical Analysis*, volume 9. North-Holland, Amsterdam, 2003.

[45] R. Glowinski and G. Guidoboni. On the preconditioned conjugate gradient solution of a stokes problem with robin-type boundary conditions. *Comptes Rendus Mathematique*, 347(15-16):903–908, 2009.

[46] G. Guidoboni, R. Glowinski, N. Cavallini, and S. Čanić. Stable loosely-coupled-type algorithm for fluid-structure interaction in blood flow. *J. Comput. Phys.*, 228(18):6916–6937, 2009.

[47] P. Hansbo. Nitsches method for interface problems in computational mechanics. *GAMM-Mitt.*, 28(2):183–206, 2005.

[48] M. Heil. An efficient solver for the fully coupled solution of large-displacement fluid-structure interaction problems. *Comput. Methods Appl. Mech. Eng.*, 193(1-2):1–23, 2004.

[49] T. Hozumi, K. Yoshida, T. Akasaka, Y. Asami, Y. Kanzaki, Y. Ueda, A. Yamamuro, T. Takagi, and J. Yoshikawa. Value of acceleration flow and the prestenotic to stenotic coronary flow velocity ratio by transthoracic color doppler echocardiography in noninvasive diagnosis of restenosis after percutaneous transluminal coronary angioplasty. *J. Am. Coll. Cardiol.*, 35(1):164–168, 2000.

[50] T.J.R. Hughes, W.K. Liu, and T.K. Zimmermann. Lagrangian-eulerian finite element formulation for incompressible viscous flows. *Comput. Methods Appl. Mech. Eng.*, 29(3):329–349, 1981.

[51] E.L. Johnson, P.G. Yock, V.K. Hargrave, J.P. Srebro, S.M. Manubens, W. Seitz, and T.A. Ports. Assessment of severity of coronary stenoses using a doppler catheter. validation of a method based on the continuity equation. *Circulation*, 80(3):625–635, 1989.

[52] M. Juonala, M.J. Jarvisalo, N. Maki-Torkko, M. Kahonen, J.S.A. Viikari, and O.T. Raitakari. Risk factors identified in childhood and decreased carotid artery elasticity in adulthood: the cardiovascular risk in young finns study. *Circulation*, 112(10):1486, 2005.

[53] M. Krafczyk, M. Cerrolaza, M. Schulz, and E. Rank. Analysis of 3D transient blood flow passing through an artificial aortic valve by Lattice-Boltzmann methods. *J. Biomech.*, 31(5):453–462, 1998.

[54] M. Krafczyk, J. Tölke, E. Rank, and M. Schulz. Two-dimensional simulation of fluid-structure interaction using lattice-Boltzmann methods. *Comput. Struct.*, 79(22-25):2031–2037, 2001.

[55] J. Krejza, M. Arkuszewski, S.E. Kasner, J. Weigele, A. Ustymowicz, R.W. Hurst, B.L. Cucchiara, and S.R. Messe. Carotid artery diameter in men and women and the relation to body and neck size. *Stroke*, 37:1103–1105, 2006.

[56] I. Kukavica and A. Tuffaha. Solutions to a fluid-structure interaction free boundary problem. *Discrete Contion. Dyn. Syst.*, 32(4):1355–1389, 2012.

[57] D. Kuzmin. Explicit and implicit fem-fct algorithms with flux linearization. *Journal of Computational Physics*, 228(7):2517–2534, 2009.

[58] D. Kuzmin and M. Möller. Algebraic flux correction i. scalar conservation laws. *Flux-corrected transport*, pages 155–206, 2005.

[59] P. Le Tallec and J. Mouro. Fluid structure interaction with large structural displacements. *Comput. Methods Appl. Mech. Eng.*, 190(24-25):3039–3067, 2001.

[60] V.S. Lee, B.S. Hertzberg, M.A. Kliewer, and B.A. Carroll. Assessment of stenosis: Implications of variability of doppler measurements in normal-appearing carotid arteries1. *Radiology*, 212(2):493, 1999.

[61] A. Leuprecht, K. Perktold, M. Prosi, T. Berk, W. Trubel, and H. Schima. Numerical study of hemodynamics and wall mechanics in distal end-to-side anastomoses of bypass grafts. *J. Biomech.*, 35(2):225–236, 2002.

[62] S. Lim and C.S. Peskin. Simulations of the whirling instability by the immersed boundary method. *SIAM J. Sci. Comput.*, 25(6):2066–2083, 2004.

[63] K.M.J. Marques, H.J. Spruijt, C. Boer, N. Westerhof, C.A. Visser, and F.C. Visser. The diastolic flow-pressure gradient relation in coronary stenoses in humans. *J. Am. Coll. Cardiol.*, 39(10):1630–1635, 2002.

[64] J.M. Meinders, L. Kornet, and A.P.G. Hoeks. Assessment of spatial inhomogeneities in intima media thickness along an arterial segment using its dynamic behavior. *American Journal of Physiology-Heart and Circulatory Physiology*, 285(1):H384, 2003.

[65] L.A. Miller and C.S. Peskin. A computational fluid dynamics of 'clap and fling' in the smallest insects. *J. Exp. Biol.*, 208(2):195–212, 2005.

[66] M. Mokhtari-Dizaji, M. Montazeri, and H. Saberi. Differentiation of mild and severe stenosis with motion estimation in ultrasound images. *Ultrasound in medicine & biology*, 32(10):1493–1498, 2006.

[67] B. Muha, S. Čanić, and M. Bukač. Analysis of the fluid-structure interaction solution obtained using a loosely coupled partioned numerical scheme, In preparation (2012).

[68] C.M. Murea and S. Sy. A fast method for solving fluid-structure interaction problems numerically. *Int. J. Numer. Meth. Fl.*, 60(10):1149–1172, 2009.

[69] W.W. Nichols and F.O.R. Michael. *McDonald's blood flow in arteries: theoretical, experimental and clinical principles*. Hodder Arnold London, UK, 2005.

[70] F. Nobile. *Numerical approximation of uidstructure interaction problems with application to haemodynamics*. PhD thesis, EPFL, Switzerland, 2001.

[71] F. Nobile and C. Vergara. An effective fluid-structure interaction formulation for vascular dynamics by generalized Robin conditions. *SIAM J. Sci. Comput.*, 30:731–763, 2008.

[72] Inc Nucleus Medical Art. http://www.empowher.com/condition/coronary-artery-disease/definition, 2009.

[73] M. Persson, Å. Rydén Ahlgren, T. Jansson, A. Eriksson, H.W. Persson, and K. Lindstrom. A new non-invasive ultrasonic method for simultaneous measurements of longitudinal and radial arterial wall movements: first in vivo trial. *Clin. Physiol. Funct. Imaging*, 23(5):247–251, 2003.

[74] C.S. Peskin. Numerical analysis of blood flow in the heart. *J. Comp. Phys.*, 25(3):220–252, 1977.

[75] C.S. Peskin and D.M. McQueen. A three-dimensional computational method for blood flow in the heart I. Immersed elastic fibers in a viscous incompressible fluid. *J. Comp. Phys.*, 81(2):372–405, 1989.

[76] A. Quaini. *Algorithms for fluid-structure interaction problems arising in hemodynamics*. PhD thesis, EPFL, Switzerland, 2009.

[77] A. Quaini and A Quarteroni. A semi-implicit approach for fluid-structure interaction based on an algebraic fractional step method. *Math. Models Methods Appl. Sci.*, 17(6):957–985, 2007.

[78] A. Quarteroni, M. Tuveri, and A. Veneziani. Computational vascular fluid dynamics: problems, models and methods. *Comput. Vis. Sci.*, 2(4):163–197, 2000.

[79] R.A. Ribeiro, J.A.S. Ribeiro, O.A. Rodrigues Filho, A.G. Caetano, and V.P.S. Fazan. Common carotid artery bifurcation levels related to clinical relevant anatomical landmarks. *Int J Morphol*, 24:413–6, 2006.

[80] E.M. Rohren, M.A. Kliewer, B.A. Carroll, and B.S. Hertzberg. A spectrum of doppler waveforms in the carotid and vertebral arteries. *American Journal of Roentgenology*, 181(6):1695, 2003.

[81] S.K. Samijo, J.M. Willigers, R. Barkhuysen, P. Kitslaar, R.S. Reneman, P.J. Brands, and A.P.G. Hoeks. Wall shear stress in the human common carotid artery as function of age and gender. *Cardiovascular research*, 39(2):515, 1998.

[82] K. Sheth. http://www.nlm.nih.gov/medlineplus/ency/presentations/100124_1.htm, 2011.

[83] C. Surulescu. On a time-dependent fluid-solid coupling in 3d with nonstandard boundary conditions. *Acta Appl. Math.*, 110(3):1087–1104, 2010.

[84] S. Svedlund and L.-M. Gan. Longitudinal common carotid artery wall motion is associated with plaque burden in man and mouse. *Atherosclerosis*, 217:120–124, 2011.

[85] S. Svedlund and L.M. Gan. Longitudinal wall motion of the common carotid artery can be assessed by velocity vector imaging. *Clin. Physiol. Funct. Imaging*, 31(1):32–38, 2011.

[86] E.M. Urbina, S.R. Srinivasan, R.L. Kieltyka, R. Tang, M.G. Bond, W. Chen, and G.S. Berenson. Correlates of carotid artery stiffness in young adults: the bogalusa heart study. *Atherosclerosis*, 176(1):157–164, 2004.

[87] R. Van Loon, P.D. Anderson, J. De Hart, and F.P.T. Baaijens. A combined fictitious domain/adaptive meshing method for fluid-structure interaction in heart valves. *Int. J. Numer. Meth. Fl.*, 46(5):533–544, 2004.

[88] S. Čanić and A. Mikelić. Effective equations modeling the flow of a viscous incompressible fluid through a long elastic tube arising in the study of blood flow through small arteries. *SIAM J. Appl. Dyn. Syst.*, 2(3):431–463, 2003.

[89] R.K. Warriner, K.W. Johnston, and R.S.C. Cobbold. A viscoelastic model of arterial wall motion in pulsatile flow: implications for doppler ultrasound clutter assessment. *Physiol. Meas.*, 29:157, 2008.

[90] I Weinberg. Carotid duplex protocol, 2012.

[91] S.T. Zalesak. Fully multidimensional flux-corrected transport algorithms for fluids. *Journal of Computational Physics*, 31(3):335–362, 1979.